Study of Top Quark Spin with the CMS Experiment at LHC

by
Hamit Mermerkaya

Master of Science
Department of Physics
Ege University
Izmir, Turkey
2004

A dissertation
submitted to the Graduate School of
Florida Institute of Technology
in partial fulfillment of the requirements
for the degree of

Doctor of Philosophy
in
Physics

Melbourne, Florida
September 2009

© Copyright 2009 Hamit Mermerkaya
All Rights Reserved

The author grants permission to make single copies

We the undersigned committee hereby recommends that the attached document be accepted as fulfilling in part the requirements for the degree of Doctor of Philosophy in Physics.

"Study of Top Quark Spin with the CMS Experiment at LHC"
a dissertation by Hamit Mermerkaya

Marc Baarmand, Ph.D.
Professor, Department of Physics and Space Sciences
Major Advisor

Joseph Dwyer, Ph.D.
Professor , Department of Physics and Space Sciences
Committee Member

Jay Kovats, Ph.D.
Professor, Department of Mathematics
Committee Member

Terry Oswalt, Ph.D.
Professor, Department of Physics and Space Sciences
Committee Member

Hamid Rassoul, Ph.D.
Professor and Associate Dean, Department of Physics and Space Sciences
Committee Member

Igor Vodopiyanov, Ph.D.
Research Scientist, Department of Physics and Space Sciences
Guest Committee Member

ABSTRACT

Study of Top Quark Spin with the CMS Experiment at LHC

by

Hamit Mermerkaya

Dissertation Advisor: Marc Baarmand, Ph.D.

Since the top quark decays before either hadronization or depolarization, and its spin flip time is much larger than its lifetime, the spin properties of the top and anti-top quarks are reflected directly in the angular distribution of the jets and leptons into which they decay. These distributions are determined by t and $\bar{t}$ polarizations and the spin correlations induced by the production mechanisms and depend on the interactions responsible for heavy quark decay.

This thesis presents the measurements of spin correlation in top quark pair production and spin polarization in t-channel single top quark production in proton-proton collisions at $\sqrt{s} = 10$ TeV with the CMS detector at LHC.

Using simulations of muon plus jets decay of the top quark pair with the CMS detector response, and based on a total integrated luminosity of two inverse femtobarn, the spin asymmetry coefficient for top quark pair production can be measured with a total uncertainty of 25% including the systematic errors.

The top quark spin asymmetry coefficients in the spectator and beamline bases in simulated t-channel single top quark production are measured with a total uncertainty of 20.0% and 23.4%, respectively, using the angular distributions of only top quark decay products in a total integrated luminosity of two inverse femtobarn.

Acknowledgements

Five years I have spent working towards a Ph.D. have been a valuable experience. I am very grateful for the support and encouragement I have received throughout my study from my supervisor, Marc M. Baarmand, and for the countless discussions I had with him, and for times that he has read this thesis to correct my writing. Also, I would like to thank Igor Vodopiyanov for the guidance and cooperation during my Ph.D. study. Additionally, I would like to appreciate the valuable suggestions and comments that Roberto Chierici, Tim Christiansen and Claudio Campagnari made on my analysis.

I also would like to thank my friends Mike Ralich, Samir Guragain and Ziyad Saleh for all their help and friendship.

I would like to thank all the members of Ph.D. committee: Hamid Rassoul, Joseph Dwyer, Terry Oswalt and Jay Kovats for their invaluable advice and great help.

I am indebted for my parents for their support throughout my Ph.D. and throughout my life.

Lastly, I would like to thank my beloved fiance, very-near-future wife and best friend Seda for her love and encouragement.

Dedication

To Seda, my Mom, Dad and brothers for all of their unending support

Contents

1 The Standard Model **1**

1.1 Quantum Field Theory 4

1.2 Quantum Electrodynamics 6

1.3 Quantum Chromodynamics 9

1.4 Unified Electroweak Theory 10

2 Top Quark Physics **14**

2.1 Introduction 14

2.2 Top Production and Decay 17

2.2.1 Strong $\mathbf{t\bar{t}}$ Pair Production 18

2.2.2 Top Decay 21

2.2.3 Electroweak Single Top Production 23

3 The CMS Experiment at LHC **26**

3.1 Large Hadron Collider 26

3.2 CMS Detector 33
3.2.1 Tracking System 36
3.2.2 Electromagnetic Calorimeter 40
3.2.3 Hadronic Calorimeter 43
3.2.4 Magnet 47
3.2.5 Muon System 48
3.2.6 Trigger 51

4 Measurement of Spin Correlation in Top Quark 54

4.1 Spin Correlation in $\mathbf{t\bar{t}}$ 54
4.1.1 Introduction 54
4.1.2 Software and Monte Carlo Event Samples 59
4.1.3 Event Reconstruction 62
4.1.4 Event Selection 64
4.1.5 Results 71
4.1.6 Systematic Uncertainties 87
4.1.7 Conclusions for $\mathbf{t\bar{t}}$ Production 91
4.2 Spin Polarization in $\mathbf{t}$-channel Single Top Quark Production . . 93
4.2.1 Introduction 93
4.2.2 Software and Monte Carlo Event Samples 98
4.2.3 Event Selection 100

4.2.4 Results 105
4.2.5 Systematic Uncertainties 115
4.2.6 Conclusions for Single Top Production 118
4.3 Future Plan 121

List of Figures

1.1 An example Feynman diagram describing the electromagnetic interaction. When the time axis is taken from left to right, the diagram represents a production of a electron-positron pair from a photon. It can be interpreted as an emission of a photon from an electron in the Bremsstrahlung radiation if the axis is rotated by 90 degrees. This diagram itself violates conservation of energy-momentum, and the interaction of this form occurs only when the photon is virtual and gets absorbed immediately by another particle, or when it occurs by a presence of other particles. . . 8

1.2 Example diagrams of strong interaction showing production of a quark-antiquark pair from a gluon (a) and gluon self-interaction (b). (a) can be interpreted as color change of a quark from blue to red through a gluon which carries anti-blue and red. 11

2.1 Average top mass measurement from Tevatron results [11] (left) and $t\bar{t}$ cross section from the CDF experiment [12] (right) . . . 19
2.2 Annihilation of quark and anti-quark pair into $t\bar{t}$ 20
2.3 Feynman graphs for the production of a $t\bar{t}$ pair via the gluon fusion in lowest order. a) t-channel amplitude b) u-channel c) gluon fusion vertex 21
2.4 Semileptonic decay channel of $t\bar{t}$ 23
2.5 Feynman diagrams for single top production. 24

3.1 The structure and experiments of LHC 28
3.2 Schematic view of the cross section of the LHC dipole. Superconducting magnets surrounding the two beam pipes create strong field to bend the particle trajectory. 29
3.3 Cross section and production rate of different physics processes at LHC in different energy/mass scales. 32
3.4 An exploded view of the CMS detector 34
3.5 A schematic showing a transverse slice through the sub-detectors of the Compact Muon Solenoid, highlighting the paths taken by a number of particle types. 35
3.6 Layout of CMS tracking system 38
3.7 A schematic of the pixel tracker. 39

3.8 A sample of a lead tungstate crystal is shown. 41

3.9 A layout of one quarter of ECAL in the $r - z$ projection 42

3.10 Longitudinal view of a quarter of the CMS detector. HCAL consists of HB, HE, HF and additional scintillator out the magnet coil (HO) 47

3.11 A schematic of one quadrant of the muon system. Drift Tubes (DT), Resistive Plate Chambers (RPC) and Cathode Strip Chambers (CSC). are shown. 49

3.12 The CMS DAQ system. 52

4.1 ALPGEN generated opening angle distributions. The number of events corresponds to an integrated luminosity of $2\,\mathrm{fb}^{-1}$. Left: cosine of lepton-b quark. Right: cosine of lepton-lower energy q. 58

4.2 E_{iso}^{calo} (left) and $p_{T\ iso}^{tracker}$ (right) distributions of the electrons matched to the generated ones in semileptonic electron channel events. Note that the P_T threshold cut on tracks is $1.0\,\mathrm{GeV}$ [53]. 66

4.3 Sum of b-tagging discriminator of two b jets 69

4.4 Left: Distributions from the reference subsample of the highest total log-LR value (P_C^{max}) of the correct and wrong jet combinations in the signal events. Normalized to $2\,\mathrm{fb}^{-1}$. Right: Purity vs. P_C^{max}. 71

4.5 The highest total log-LR value (P_C^{max}) distributions from the reference subsample before (left) and after (right) $RelIso > 0.9$ cut. Both are normalized to $2\,\mathrm{fb}^{-1}$. 72

4.6 Muon relative isolation distributions for the reference subsample (without QCD events) (left) and for the analysis subsample plus QCD events (right). The fit curves are superimposed. 73

4.7 Resolution of $cos(\phi_{l\text{-}b})$ (left) and $cos(\phi_{l\text{-}q})$ (right) 75

4.8 Reconstructed top quark invariant mass spectra: t decaying into three jets (left), t decaying into muon, neutrino and b jet (right). 77

4.9 Reconstructed opening angle distributions: l-b angle (left) and l-q angle (right). 78

4.10 Response matrices from the reference subsample: l-b angle (left) and l-q angle (right). 79

4.11 Pull distributions from unfolding the $\cos(\phi_{l\text{-}b})$ distribution with regularization parameter $\tau = 3$. 81

4.12 Pull distributions from unfolding the $\cos(\phi_{l\text{-}q})$ distribution with regularization parameter $\tau = 3$. 82

4.13 Background subtracted and unfolded opening angle distributions (black points): l- angle (left) and l-q angle (right). The black lines represent a global fit of both angular distributions. The number of events corresponds to an integrated luminosity of $2\,\mathrm{fb}^{-1}$. 84

4.14 Ratio of the analysis (full simulation) to the reference (fast simulation) selection efficiency for the opening angle distributions: l-b angle (left) and l-q angle (right). 86

4.15 Background subtracted and unfolded opening angle distributions (black): l-b angle (left) and l-q angle (right). The black lines represent a global fit of both angular distributions, which gives $A_D = 0.199 \pm 0.036$. The number of events corresponds to an integrated luminosity of $2\,\text{fb}^{-1}$. 87

4.16 MadGraph generated angular distributions for the spectator basis. The number of events corresponds to an integrated luminosity of 2 fb^{-1}. Left: $cos(\phi_{l\text{-}s})$ in the t rest frame. Right: $cos(\phi_{l\text{-}s})$ in the $\bar{t}$ rest frame. 97

4.17 MadGraph generated angular distributions for the beamline basis and $|\eta_{spec.jet}| > 2.5$. The number of events corresponds to an integrated luminosity of 2 fb^{-1} before the η cut. Left: $cos(\phi_{l\text{-}z})$ in the t rest frame. Right: $cos(\phi_{l\text{-}z})$ in the $\bar{t}$ rest frame. 97

4.18 b-tag discriminator distributions for b-jet (matched to the b-quark) and non-b-jet (not matched to the b-quark). 101

4.19 Transverse momentum and pseudorapidity distributions of the final state objects matched to the generated ones in t-channel single top production. 102

4.20 Reconstructed W mass (without neutrino P_Z) (left) and top quark mass (b-tag jet combined with W) (right). The W and t mass window requirements are shown. 104

4.21 $\Delta\phi$ between the top quark and the spectator jet > 2.5 radians (left), $|\vec{\Sigma}_T| < 50$ (right). 105

4.22 χ^2 obtained from the fit of the neutrino components < 5. . . . 106

4.23 Muon relative isolation distributions for the reference subsample (without QCD events) (left) and for the analysis subsample plus QCD events (right). The fit curves are superimposed. 107

4.24 Reconstructed t and $\bar{t}$ quark invariant mass spectra. 109

4.25 Reconstructed angular distributions in top events only: l-s angle (left) and l-z angle (right). 109

4.26 Resolution of $cos(\phi_{l\text{-}s})$ (left) and $cos(\phi_{l\text{-}z})$ (right) in top events. 110

4.27 Response matrices from the reference subsample: l-s angle (left) and l-z angle (right). 111

4.28 Pull distributions from unfolding the $\cos(\phi_{l\text{-}s})$ distribution with regularization parameter $\tau = 4$. 112

4.29 Pull distributions from unfolding the $\cos(\phi_{l\text{-}z})$ distribution with regularization parameter $\tau = 4$. 113

4.30 Background subtracted and unfolded opening angle distributions in single t events (black points): l-s angle (left) and l-z angle (right). The black lines represent the fit of angular distributions. The number of events corresponds to an integrated luminosity of $2\,\mathrm{fb}^{-1}$. 115

1 Sum of b-tagging discriminator of two b jets 130

2 Transverse momentum of the hadronically decaying t quark divided by the average transverse momentum of the hadronically decaying t quarks over all possible jet combinations. 131

3 Probability obtained from the kinematic fit of the two light jets with W-mass constraint. 131

4 Mass of the hadronically decaying t. 132

5 Mass of the hadronically decaying W. 132

6 Mass of the leptonically decaying t estimated with neutrino $P_z = 0$. 133

7 Mass of the hadronically decaying t using the modified light jets parameters from the kinematic fit with W-mass constraint. . . . 133

8 Probability obtained from the fit of the neutrino components. . 134

List of Tables

1.1 The Standard Model fermions. The index, i, on each quark runs from 1 to 3 and represents its color. 2

1.2 The Standard Model interaction mediators and Higgs boson . . 3

2.1 Upper part: number of $t\bar{t}$ events produced at the Tevatron and expected $t\bar{t}$ production rates at the LHC and at a future e^+e^- linear collider (ILC), where $\mathcal{L}$ is the integrated luminosity of the respective collider in units of fb^{-1}. Lower part: Number of t and $\bar{t}$ events at the Tevatron and expected number at the LHC produced in single top reactions. 18

3.1 Beam parameters for nominal proton and heavy ion runs. 31

4.1 Spin analyzing power κ_f of the top quark daughter particles. . . 56

4.2 Analysis subsample. 61

4.3 Reference subsample. 62

4.4 QCD samples. 62

4.5 Selection flow for the analysis subsample and the QCD samples. 76

4.6 Results of the Gaussian fits for the $\cos(\phi_{l\text{-}b})$ (left) and $\cos(\phi_{l\text{-}q})$ (right) pull distributions with regularization parameter $\tau = 3$. . 83

4.7 Results obtained for each source of systematic uncertainty considered and the total systematic uncertainty. The total gives the sum of the systematic errors in quadrature. 92

4.8 Analysis subsample. 99

4.9 Reference subsample. 100

4.10 QCD samples. 100

4.11 Selection flow for the analysis subsample plus the QCD samples. 108

4.12 Results of the Gaussian fits for the $\cos(\phi_{l\text{-}s})$ (left) and $\cos(\phi_{l\text{-}z})$ (right) pull distributions with regularization parameter $\tau = 4$. . 114

4.13 Results obtained for each source of systematic uncertainty considered and the total systematic uncertainty. The total gives the sum of the systematic errors in quadrature. 120

Chapter 1

The Standard Model

The Standard Model [1, 2] best describes the elementary particles and their interactions based on the experimental observations of the past 60 years. It is a quantum field theory formulated on the $SU(3)_C \times SU(2)_L \times U(1)_Y$ gauge group where the subscripts indicates the color (C) exchange in QCD, left-handed current (L) and hyper charge (Y) involved in the Electroweak interaction. $SU(3)_C$ represents Quantum Chromodynamics (QCD), the theory of strong interactions, and $SU(2)_L \times U(1)_Y$ is the unified Electroweak (EW) theory which describes electromagnetic (EM) and weak interactions as different manifestations of a single system. Within the SM, there are three types of elementary particle: leptons, quarks and mediators. The leptons and quarks are summarized in Table 1.1. They are all spin 1/2 fermions, each with a corresponding anti-particle (not shown), and fall into three distinct generations. Quarks are distinguishable

from leptons in that they interact via the strong force and come with a red, blue or green strong charge or color.

Table 1.1: The Standard Model fermions. The index, i, on each quark runs from 1 to 3 and represents its color.

		charge (e)	spin	interaction
leptons	$e \quad \mu \quad \tau$	-1	$\frac{1}{2}$	EM, weak
	$\nu_e \quad \nu_\mu \quad \nu_\tau$	0	$\frac{1}{2}$	weak
quarks	$u_i \quad c_i \quad t_i$	$+\frac{2}{3}$	$\frac{1}{2}$	Strong, EM, weak
	$d_i \quad s_i \quad b_i$	$-\frac{1}{3}$	$\frac{1}{2}$	Strong, EM, weak

The interaction of the particles is mediated via the exchange of spin = 1 gauge bosons: the photon (γ), the W, Z and the gluons (g), which are the mediators of the electromagnetic, weak and strong forces, respectively. Higgs boson is one quantum component of the theoretical Higgs field. In empty space, Higgs field has an amplitude different from zero; i.e., a non-zero vacuum expectation value. The existence of this non-zero vacuum expectation plays a fundamental role: it gives mass to every elementary particle which has mass, including Higgs boson itself. Higgs boson, which has spin 0 and no anti-particle, has not been observed experimentally yet. The mediators and Higgs boson are summarized in Table 1.2

Table 1.2: The Standard Model interaction mediators and Higgs boson

			charge (e)	spin	mass (GeV)
interactions	Weak	Z^0	0	1	91.2
		W^-	-1	1	80.4
		W^+	$+1$	1	80.4
	EM	γ	0	1	0
	Strong	gluons (8)	0	1	0
	Higgs	H	0	0	not observed yet

Since photons are massless particles, the EM force has an infinite range. The coupling strength of the EM interaction is $\alpha \approx 1/137$ at low energies, but increases as the energy increases. The theory of the EM interaction was independently formulated first as Quantum Electrodynamics (QED) which showed a remarkable agreement with the experimental observations. Since QED itself is a unified theory of electricity and magnetism, the next step was to include another type of force.

The mediators of the weak forces are required to be massive, otherwise the cross section of the weak interaction diverges to infinity. The weak interaction is unique in that it violates parity which is conserved in the EM and strong interactions, and it allows mixing of quark flavors. The different EM and weak interactions are successfully incorporated in the unified EW theory where the

photon and the weak bosons are represented as combinations of four gauge fields required by the $SU(2)_L \times U(1)_Y$ local gauge theory.

Characteristic to the strong interaction is the particular property that the coupling constant decreases with energy and increases with distance (asymptotic freedom). Hence, the quarks are only observed as bound states hadrons. Another consequence of the quark confinement is that forcing the quarks at large separation by enough energy leads to the creation of quark-antiquark pairs. In QCD, these phenomena are explained in terms of color, where all observable stable states must be color singlets. Each quark flavor may take one of the three colors, red (r), green (g) or blue (b), and a stable hadron must be a colorless combination of these quarks. Gluons are represented as combinations of two colors such that the eight gluon states form an SU(3) octet, hence are not observable as free particles.

In total, the SM describes sixty-one elementary particles: thirty-six quarks, twelve leptons, twelve mediators and one Higgs.

1.1 Quantum Field Theory

Quantum Field Theory (QFT) proposed by Paul Dirac in the late 1920's, is a theory of canonically quantized fields operating on a vacuum. This corrects several limitations to quantum mechanics such as the possibility of particle cre-

ation/annihilation and the negative probabilities introduced when incorporating special relativity.

The Dirac (Equation 1.1) and Klein-Gordon (Equation 1.2) Lagrangian densities describes the free fermion and boson fields, respectively.

$$\mathcal{L}_{Dirac} = \bar{\phi}(x)(i\gamma^{\mu}\partial_{\mu} - m)\phi(x) \,, \tag{1.1}$$

$$\mathcal{L}_{KG} = \frac{1}{2}\partial^{\mu}\phi(x)\partial_{\mu}\phi(x) - \frac{1}{2}m^2\phi^2(x) \,, \tag{1.2}$$

where γ^{μ} are the Dirac matrices and m is the particle mass. Instead of the quantum mechanical interpretation of these equations, the wavefunction, ϕ, is now a free field operating on a vacuum state. It is quantized by imposing commutation relations on the field and its conjugate momentum.

The evolution of a field with time can be described by a unitary transformation of the time independent field (or Schrödinger field), performed by an operator $e^{i\hat{H}t}$. Here, $\hat{H}$ is the Hamiltonian which can be expressed as a sum of the free field and interaction Hamiltonians, $\hat{H}_0 + \hat{H}_{int}$. To decouple these effects, the evolution is often considered in two separate steps. The evolution with $\hat{H}_0$ is known as the Dirac field, the evolution of the Dirac field with $\hat{H}_{int}$ is known as the Heisenberg field. The Equation 1.3 describes physics of any scattering process.

$$\phi_H(t) = U^{-1}(t)\phi_D(t)U(t) \,, \tag{1.3}$$

where $U(t) = e^{i\hat{H}_{int}t}$ and ϕ_H, ϕ_D are the Heisenberg and Schrödinger fields,

respectively. $U(t)$ evolves in time as shown in Equation 1.4

$$i\frac{dU(t)}{dt} = \hat{H}_{int}(t)U(t)\,. \tag{1.4}$$

The solution of Equation 1.4 with the boundary condition $U(t \to -\infty) = 1$ is given by

$$U(t) = e^{-i\int_{-\infty}^{t}\hat{H}_{int}(t')dt'}\,. \tag{1.5}$$

The scattering (S matrix), which describes the full transformation from inbound state at $t \to -\infty$ to an outbound state $t \to +\infty$, is defined by

$$S = U(t \to +\infty)\,. \tag{1.6}$$

Hence, *S-matrix element* can be given as

$$S_{fi} = \langle f, \phi_H(\to +\infty)|i, \phi_H(\to -\infty)\rangle\,. \tag{1.7}$$

For further details on QFT, some good introductory texts are [3, 4].

1.2 Quantum Electrodynamics

Quantum Electrodynamics (QED) is the theory which describes electromagnetic interactions in terms of particle exchange [5]. It is based on abelian gauge theory. Dirac lagrangian density is invariant under global transformations of the U(1) group with bispinor field of spin-1/2 particle (e.g. electron-positron field),

$$\phi \to \phi' = e^{i\theta}\phi\,, \tag{1.8}$$

where is θ a real constant number and the generator of the $U(1)$ group. However, it is not invariant under local gauge transformations,

$$\phi \rightarrow \phi' = e^{iq\theta(x)}\phi \,, \tag{1.9}$$

where $\theta(x)$ is a space-time dependent function (with a electromagnetic coupling constant q). In order to achieve the local gauge invariance, the covariant derivative must be introduced as

$$D_\mu = \partial_\mu + iqA_\mu \,, \tag{1.10}$$

where A_μ is vector field which is commonly referred to as gauge field . It transforms as

$$A_\mu \rightarrow A'_\mu = A_\mu + \partial_\mu\theta(x) \,. \tag{1.11}$$

The new gauged Dirac Lagrangian density then becomes:

$$\mathcal{L}_{Dirac} = \bar{\phi}(x)(i\gamma^\mu D_\mu - m)\phi(x) \tag{1.12}$$

$$= \bar{\phi}(x)i\gamma^\mu\partial_\mu\phi(x) - q\phi(\bar{x})\gamma^\mu A_\mu\phi(x) - m\phi(\bar{x})\phi(x) \,, \tag{1.13}$$

is now invariant under the local gauge transformations. The gauge invariant kinetic term for the field A_μ can be introduced using a field tensor as

$$F_{\mu\nu} = \partial_\mu A_\nu - \partial_\nu A_\mu \,, \tag{1.14}$$

and the complete QED Lagrangian describing the electromagnetic interaction becomes:

$$\mathcal{L}_{QED} = \bar{\phi}(x)i\gamma^\mu\partial_\mu\phi(x) - q\phi(\bar{x})\gamma^\mu A_\mu\phi(x) - m\phi(\bar{x})\phi(x) - F_{\mu\nu}F^{\mu\nu} \,. \tag{1.15}$$

The vector field A_μ can be identified as the photon field, and the third term describes the photon interacting with the fermions with strength q which is set equal to the electric charge. The Feynman diagram of electromagnetic interaction is shown in Figure 1.1.

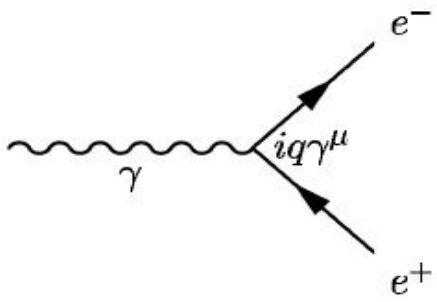


Figure 1.1: An example Feynman diagram describing the electromagnetic interaction. When the time axis is taken from left to right, the diagram represents a production of a electron-positron pair from a photon. It can be interpreted as an emission of a photon from an electron in the Bremsstrahlung radiation if the axis is rotated by 90 degrees. This diagram itself violates conservation of energy-momentum, and the interaction of this form occurs only when the photon is virtual and gets absorbed immediately by another particle, or when it occurs by a presence of other particles.

1.3 Quantum Chromodynamics

Quantum Chromodynamics (QCD) [6], the theory of strong interactions, is formulated in an analogous way to QED theory, by enforcing local gauge invariance on the free Dirac Lagrangian,

$$\mathcal{L}_0 = \bar{\phi_j}(x)(i\gamma^\mu \partial_\mu - m)\phi_i(x)\,, \tag{1.16}$$

where ϕ_j is the quark field with color index = 1,2,3. (This index will be omitted from the following equations for simplicity.) However, the $\mathrm{U(1)_Y}$ is now replaced by the non-abelian group $\mathrm{SU(3)_C}$, such that the local transformation of the fermion fields takes the form shown in Equation 1.17.

$$\phi \rightarrow \phi' = e^{i\theta_a(x)T_a}\phi\,. \tag{1.17}$$

T_a are the eight Gell-Mann matrices representing the generators of the $\mathrm{SU(3)_C}$ group and satisfying the commutation rules

$$[T_a, T_b] = if_{abc}T_c\,, \tag{1.18}$$

where f_{abc} are the structure constants of the group. The index runs over eight generators of the $\mathrm{SU(3)_C}$.

A similar covariant derivative which transforms under $\mathrm{SU(3)_C}$ gauge as

$$D_\mu = \partial_\mu + ig_s T_a G^a_\mu\,, \tag{1.19}$$

has to be introduced. However, the gauge freedom of G^a_μ is required to compensate the local phase transformations, so it transforms as

$$G^a_\mu \rightarrow G^{a\prime}_\mu = G^a_\mu - \frac{1}{\phi}\partial_\mu \phi_a - f_{abc}\phi_b G^c_\mu \, . \tag{1.20}$$

The complete Lagrangian density for QCD becomes:

$$\mathcal{L}_{QCD} = i\bar{\phi}\gamma_\mu \partial_\mu \phi - m\bar{\phi}\phi - g_s \bar{\phi}\gamma_\mu T_a G^a_\mu \phi - \frac{1}{4} G^a_{\mu\nu} G_a \mu\nu \, , \tag{1.21}$$

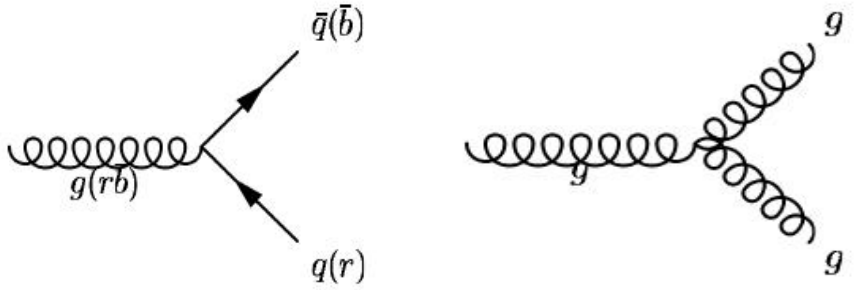
where the tensor field is defined by

$$G^a_{\mu\nu} = \partial_\mu G^a_\nu - \partial_\nu G^a_\mu - g_s f_{abc} G^a_\mu G^c_\nu \, . \tag{1.22}$$

The last term in Equation 1.22 which does not appear for the photon field in QED arises from the non-Abelian structure of the $\mathrm{SU(3)_C}$ group where the generators are matrices which do not commute. The third term of Equation 1.21 is interpreted as gluon field G^a_μ interacting with the quarks (See Figure 1.2, and the quadratic $G_\mu G_\nu$ contribution indicates that gluons self-interact as illustrated by the Feynman diagram in Figure 1.2.

1.4 Unified Electroweak Theory

Unification of electromagnetic force and weak force into single gauge theory was performed by Glashow-Weinberg- Salam model [7, 8, 9] based on $\mathrm{SU(2)_L \times U(1)_Y}$ group, resulting in 3+1 gauge fields. The subscript Y stands for hypercharge which is defined as



(a) (b)

Figure 1.2: Example diagrams of strong interaction showing production of a quark-antiquark pair from a gluon (a) and gluon self-interaction (b). (a) can be interpreted as color change of a quark from blue to red through a gluon which carries anti-blue and red.

$$Q = I_3 + \frac{Y}{2}\,, \tag{1.23}$$

where Q is the EM charge and I_3 is the third component of the weak isospin. Local field transformations within this theory is given as

$$\phi \rightarrow \phi' = e^{i\theta^a(x)T^a} e^{iYw(x)}\phi\,, \tag{1.24}$$

where T^a represents SU(2) algebra. The covariant derivative which makes the Lagrangian invariant under this transformation takes the form,

$$D_\mu = \partial_\mu - igT_aW_\mu^a - ig'YA_\mu\,. \tag{1.25}$$

where W_μ and A_μ are the gauge fields associated with SU(2) and U(1) groups respectively, g' and g are the U(1) and SU(2) gauge field coupling constants

respectively. The compensating electroweak gauge fields is necessary to balance the gauge freedom of ϕ. This gauge freedom is described by

$$W_\mu^i \rightarrow W_\mu^i + \frac{1}{2}\epsilon^{ijk}\phi_\mu W_\mu^k \, . \tag{1.26}$$

The free weak gauge field can be described in covariant form by

$$\mathcal{L}_{gauge} = \frac{1}{4}Tr(T^i)\mathbb{F}_{\mu\nu}^i T_i \mathbb{F}_i^{\mu\nu} \, . \tag{1.27}$$

The last term in Equation 1.28,

$$\mathbb{F}_{\mu\nu}^i = \partial_\mu W_\nu^i - \partial_\nu W_\mu^i + g\epsilon^{ijk}W_\mu^j W_\nu k \, , \tag{1.28}$$

does not appear in the corresponding equation for the electromagnetic field (Equation 1.14) and is a direct consequence of the non-abelian nature of the SU(2) group.

The physical electroweak fields are defined as linear combinations of the weak and electromagnetic gauge fields, as described by Equations 1.29, 1.30 and 1.31. Here, we see how the SU(2) and U(1) gauge theories are unified.

$$W_\mu^\pm = \frac{1}{\sqrt{2}}(W_\mu^1 \mp iW_\mu^2) \, , \tag{1.29}$$

$$Z_\mu = A_\mu sin\theta_w - W_\mu^3 cos\theta_w \, , \tag{1.30}$$

$$\gamma_\mu = A_\mu cos\theta_w + W_\mu^3 sin\theta_w \, , \tag{1.31}$$

where θ_w is the weak mixing angle (Weinberg angle) defined by

$$\frac{g'}{g} = tan\theta_w \, . \tag{1.32}$$

Due to the parity violating nature of the weak interaction, only left-handed chirality fermion states interact with the SU(2) gauge field, A^a_μ. To achieve this mathematically, the left-handed component of each field ϕ^i_L is represented by an SU(2) doublet and the right-handed component, ϕ_R, by a singlet. The full set of electroweak fermion doublets are listed in Table 1.1. They are paired off according to their generation and quark/lepton status. Each fermion has a corresponding right-handed singlet.

Including the kinetic terms for the gauge fields, the Lagrangian density for the EW processes can be written as

$$\begin{aligned}\mathcal{L}_{EW} &= i\bar{\phi_{Li}}\gamma\mu(\partial_{mu} + \frac{i}{2}gT^aW^a_\mu + \frac{i}{2}g'YA + \mu)\phi^i_L \\ &+ i\bar{\phi_R}\gamma^\mu(\partial_\mu + \frac{i}{g}'YA_\mu)\phi_R - \frac{1}{4}\mathbb{F}_{\mu\nu}\mathbb{F}_{\nu\mu} - \frac{1}{4}F_{\mu\nu}F_{\nu\mu}\,.\end{aligned} \tag{1.33}$$

No mass terms exist in the electroweak Lagrangian so far. Neither a fermion mass term of the form $m\bar{\phi}\phi = m(\bar{\phi_R}\phi_L + \bar{\phi_L}\phi_R)$, nor a boson mass term of $m_2A_\mu A^\mu$ is invariant under the electroweak gauge. Though experiment supports this prediction for the photon, all other SM particles do require a mass. For this reason electroweak symmetry must be broken.

Chapter 2

Top Quark Physics

2.1 Introduction

The top quark, the heaviest known fundamental particle, was discovered thirteen years ago [10, 13] at the Tevatron proton anti-proton collider. Before its discovery, theoretical and experimental observations led physicists to consider the existence of the top quark for decades. The discovery of third family in lepton sector immediately brought high expectation of the existence of the corresponding third family in the quark sector from a simple symmetry argument between the two types of fermions. Kobayashi and Maskawa pointed out that CP (charge×parity) violation, observed in Kaon decay, cannot be explained with four quark flavors but with six flavors. In 1977, the $b\bar{b}$ bound state Υ was discovered at Fermilab. With firm evidence of the existence of the third quark

family, the electroweak model required that the third family be a doublet not a singlet; for otherwise the b quark could only decay via the neutral current but this decay was not seen. The discovery of the top quark was therefore an expected and awaited event though it proved difficult mainly due to its mass being much larger than any of the other elementary particles.

At a hadron collider like the Tevatron, top quarks are predominantly produced together with their anti-quarks. Quite recently, the D0 [14] and the CDF [15] experiment reported also evidence for the observation of singly produced t and $\bar{t}$ quarks. For now, the Tevatron is the only source of these quarks. However, this should change soon when the CERN Large Hadron Collider (LHC) will start operation. Millions of top quarks will be produced already in the low luminosity phase $\mathcal{L} = 10\,\mathrm{fb}^{-1}$ of this collider, see Table 2.1. This will open up the possibility to explore this quark with high precision.

The top quark couples to all known fundamental interactions. Because of its large mass, it is expected to couple strongly to the forces that break the electroweak gauge symmetry. New physics might be preferentially coupled to it. It is therefore a sensitive probe to new physics. While the interactions of the top quark have not been explored in great detail so far, its mass has been experimentally determined very precisely, see Figure 2.1 left. Refinements in the analysis and increase in the accumulated data are reducing the errors on the measurements, and the current best measurement of the top mass is accurate to

less than 2 GeV [11] with the measured value of $170.9 \pm 1.1(\text{stat}) \pm 1.5(\text{sys})$. Top quark events are also a major source of background for many search channels, and precise understanding of top signal is crucial to claim new physics. Also, top quark events provide an essential tool for understanding and calibrating the detector: triggering, b-tagging, jet energy scale can all benefit from top signal.

The top quark is an extremely elusive object. Because its mass is so large, it can decay into on-shell W bosons, i.e., the two-particle decay mode $t \to bW^+$ is kinematically possible. The SM predicts the top quark to decay almost exclusively into this mode, which leads to the prediction that the average proper lifetime of the t quark is extremely short, $\tau_t = 1/\Gamma_t = 5 \times 10^{-25}$ s where $\Gamma_t \backsimeq 1.3$ GeV is decay width of t quark and much smaller than the experimental resolution at the Tevatron or at the LHC. At present, no reasonable method is known how to directly determine Γ_t at a hadron collider. For comparison, the mean lifetime of b quarks, which is the next heaviest quark, is almost 13 orders of magnitude larger, $\tau_b = 1.5 \times 10^{-12}$ s . The lifetime τ_t is an order of magnitude smaller the hadronization time $\tau_{had} = 1/\Lambda_{QCD} \sim 3 \times 10^{-24}$ s, which characterizes the time it takes for an (anti-)quark produced in some reaction to combine with other produced (anti-)quarks and form a color-neutral hadron due to confinement. Therefore, top quarks are not able to form top mesons $t\bar{q}$ or baryons tqq' .

Top quarks, like the other quarks, carry color charge they transform as a

color triplet under the $SU(3)_C$ gauge group of the strong interactions. The top quark is the $I_3 = 1/2$ weak-isospin partner of the b quark. The electric charge of the top quark is therefore $Q_t = 2/3$ in units of the positron charge $e > 0$ according to the SM.

Although a dedicated experimental verification has so far not been made, there is no doubt that the top quark, as observed at the Tevatron, is a spin 1/2 fermion. The observed decay $t \to bW^+$, the known spins of W and b, and the conservation of total angular momentum imply that the top quark is a fermion. If the spin of the top quark were 3/2, the $t\bar{t}$ cross section at the Tevatron would be much larger than the measured one. A direct experimental evidence for the top quark having spin 1/2 would be the observation of the resulting polarization and spin-correlation effects. Definite measurements are expected to be done at the LHC [16]. Spin properties and correlation of top quark in $t\bar{t}$ are discussed in more detail in section 4.1.

2.2 Top Production and Decay

Top quark are produced at LHC in two ways; Strong $t\bar{t}$ pair and electroweak single top production. The $t\bar{t}$ cross section is about 2.5 times larger than the single top cross section.

Table 2.1: Upper part: number of $t\bar{t}$ events produced at the Tevatron and expected $t\bar{t}$ production rates at the LHC and at a future e^+e^- linear collider (ILC), where $\mathcal{L}$ is the integrated luminosity of the respective collider in units of fb^{-1}. Lower part: Number of t and $\bar{t}$ events at the Tevatron and expected number at the LHC produced in single top reactions.

$t\bar{t}$ pairs	dominant reaction	$N_{t\bar{t}}$
Tevatron $p\bar{p}$ (1.96 TeV)	$q\bar{q} \to t\bar{t}$	$\sim 7 \cdot 10^4 \times \mathcal{L}$
LHC: pp (14 TeV)	$gg \to t\bar{t}$	$\sim 9 \cdot 10^5 \times \mathcal{L}$
ILC: e^+e^-(400 GeV)	$e^+e^- \to t\bar{t}$	$\sim 800 \times \mathcal{L}$
Single top	dominant reaction	$N_t + N_{\bar{t}}$
Tevatron	$u + b \to d + t$	$\sim 3 \cdot 10^3 \times \mathcal{L}$
LHC	$u + b \to d + t$	$\sim 3.3 \cdot 10^5 \times \mathcal{L}$

2.2.1 Strong $t\bar{t}$ Pair Production

Top quarks are dominantly produced in pairs ($t\bar{t}$) via strong interaction. The leading order processes for the production of a $t\bar{t}$ pair in hadron-hadron collisions are

$$\begin{aligned} q(p_1) + \bar{q}(p_2) &\to t(p_3) + \bar{t}(p_4) \text{ and} \\ g(p_1) + g(p_2) &\to t(p_3) + \bar{t}(p_4)\,, \end{aligned} \tag{2.1}$$

where q is quark, g is gluon and $p = (E, p_x, p_y, p_z)$ is the four momenta of the partons. About 13% of top pairs are produced by quark anti-quark annihilation.

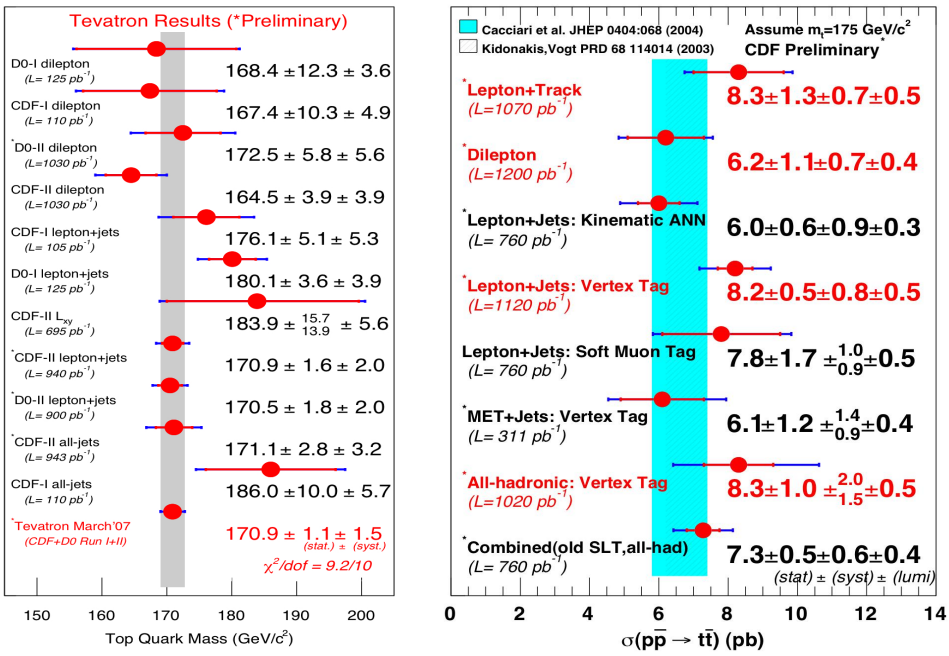


Figure 2.1: Average top mass measurement from Tevatron results [11] (left) and $t\bar{t}$ cross section from the CDF experiment [12] (right)

Feynman graph for production of $t\bar{t}$ pairs via quark anti-quark annihilation is shown Figure 2.2. The bulk of $t\bar{t}$ pairs, about 87% is expected to produced by gluon fusion processes whose lowest Feynman graphs are shown in Figure 2.3.

The differential partonic cross section of $2 \rightarrow 2$ scattering process is given by

$$d\hat{\sigma} = \frac{1}{2(p_1+p_2)^2} \frac{d^3p_3}{(2\pi)^3 2E_3} \frac{d^3p_4}{(2\pi)^3 2E_4} (2\pi)^4 \delta^4(p_1+p_2-p_3-p_4) |\overline{M}|^2 \,, \qquad (2.2)$$

where $\frac{1}{2(p_1+p_2)^2}$ is flux of incoming partons and $|\overline{M}|^2$ is the squared matrix ele-

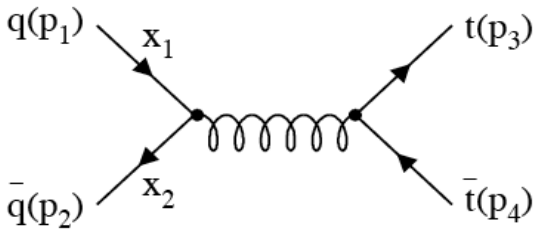


Figure 2.2: Annihilation of quark and anti-quark pair into $t\bar{t}$

ments averaged over initial and summed over final color and spin states

$$|\overline{M}|^2(q\bar{q} \to t\bar{t}) = (4\pi\alpha_s)^2 \frac{8}{9}\left(2\frac{(p_1\cdot p_3)^2 + (p_2\cdot p_3)^2}{(p_1+p_3)^4} + \frac{m_t^2}{(p_1+p_2)^2}\right) \tag{2.3}$$

and

$$\begin{aligned}|\overline{M}|^2(gg \to t\bar{t}) = (4\pi\alpha_s)^2 &\left(\frac{(p_1+p_2)^4}{24(p_1\cdot p_3)(p_2\cdot p_3)} - \frac{3}{8}\right) \\ &+ \times \left(4\frac{(p_1\cdot p_3)^2 + (p_2\cdot p_3)^2}{(p_1+p_2)^4} + \frac{m_t^2}{(p_1+p_2)^2} - \frac{m_t^4(p_{1+}p_2)^4}{(p_1\cdot p_3)^2(p_2\cdot p_3)^2}\right)\end{aligned} \tag{2.4}$$

are matrix elements for $t\bar{t}$ production mechanisms. The differential hadronic cross section then becomes

$$d\sigma = \int_0^1 \int_0^1 dx_1 dx_2 f_1(x_1, Q^2) f_2(x_2, Q^2) d\hat{\sigma}\,, \tag{2.5}$$

where f's are parton density function which give probability of finding a parton ($q, \bar{q}$ or g) with momentum fraction $x \in (0,\, 1)$ in the proton at a given Q scale which is ambiguous but of the order of the invariant top quark mass squared.

The $t\bar{t}$ production at the LHC with a center of mass energy of $\sqrt{s} = 14\,\text{TeV}$ gives a leading order (LO) cross-section of about 560 pb assuming a top mass of

$m_t = 170.2\,\text{GeV}$. Calculations of the next to leading order (NLO) cross section predict about 906 pb. At $\sqrt{s} = 10\,\text{TeV}$, LO and NLO cross-sections are 318 and 414 pb, respectively [17].

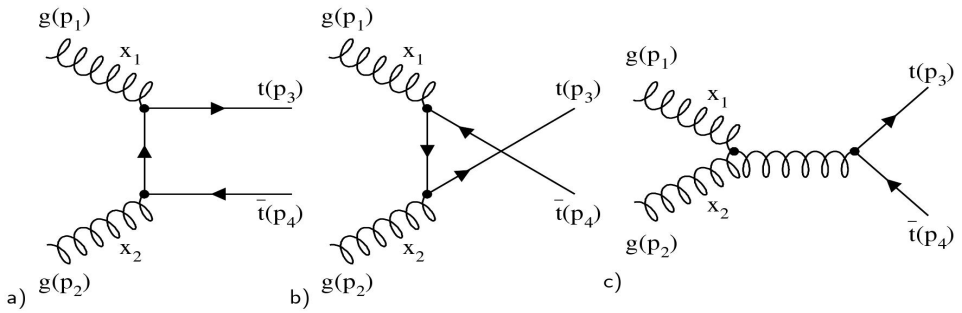


Figure 2.3: Feynman graphs for the production of a $t\bar{t}$ pair via the gluon fusion in lowest order. a) t-channel amplitude b) u-channel c) gluon fusion vertex

2.2.2 Top Decay

The branching fraction of top quarks decaying into b quarks,

$$B_b = \frac{\Gamma(t \to Wb)}{\Gamma(t \to Wq)}\,, \tag{2.6}$$

has been measured by CDF experiment at Fermilab at $B_b = 0.99$ [18]. Within the three generation standard model, this ratio can be expressed by the Cabibbo-Kobayashi-Maskawa (CKM) matrix elements [19] as

$$B_b = \frac{|V_{tb}|^2}{|V_{tb}|^2 + |V_{ts}|^2 + |V_{td}|^2}\,, \tag{2.7}$$

where denominator is exactly equal to 1 due to unitary of CKM Matrix. The top quark decays 99.83% of time into a b quark and a W boson. W boson

decays into either lepton+neutrino or two light quarks. The branching ratios are, for Γ_W, $m_b \neq 0$ and including QCD corrections:

$$B(t \to bl^+v_l) = 0.108 \quad (l = e, \mu, \tau), \qquad B(t \to bq\bar{q}) = 0.337 \times |V_{q\bar{q}}|^2 \,. \quad (2.8)$$

Using the central values of the respective CKM matrix elements, we have then $B(t \to bu\bar{d}) = B(t \to bc\bar{s}) = 0.328$, $B(t \to bu\bar{s}) = 0.017$ and $B(t \to bc\bar{b}) = 6 \times 10^{-4}$. The $t\bar{t}$ signals are then classified according to decays of W^+W^- bosons from $t\bar{t} \to bW^+ + bW^-$ as dileptonic and semileptonic (lepton+jets), and fully hadronic decay channels.

From Equation 2.8, we obtain a branching fraction of 10.5%, 43.5% and 45.5% for the dilepton, semilepton and all jets modes, respectively. Many top-physics analyzes (will) use dilepton and lepton + jets final states with $l = e, \mu$ only. In this case, the corresponding branching ratios are 4.7%, 29% and 45.5%.

Figure 2.4 indicates $t\bar{t}$ decay topology in the case of the semileptonic decay channel. The two incoming gluons carrying the proton momentum fractions are x_1 and x_2, respectively. The top quarks decay in a W boson and a b quark. Here, one W boson decays to a charged lepton and the corresponding (anti-)neutrino. The other W boson, which decays into 2 light quarks and b quark, will be detected through the jets of their fragmentation products.

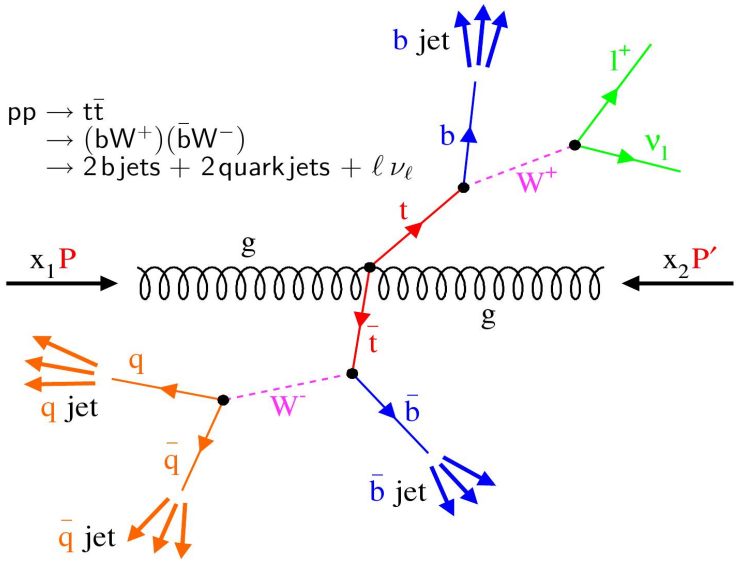


Figure 2.4: Semileptonic decay channel of $t\bar{t}$

2.2.3 Electroweak Single Top Production

In the hadronic production of single (anti-)top quarks, the weak interactions are involved in an essential way. Therefore, these reactions provide, besides top-quark decay, another important opportunity to study the charged weak current interactions of this quark. Also, single top quarks are produced highly polarized due to $V - A$ structure of weak interaction, so single top provides a good laboratory for studying the spin of the top quark which will be discussed in section 4.2. New physics could appear in single top events. It provides the possibility to investigate fourth generation of the quarks and the existence of W'.

In the SM, there are three main hadronic production modes, see Figure 2.5

- t-channel: the dominant process involves the exchange of a space-like W ($Q^2_W < 0$) boson . This process is also called W-gluon fusion, because the b-quark ultimately arises from a gluon splitting to $b\bar{b}$. There are two processes, 2-2 (leading order process) shown in Figure 2.5 (left t-channel diagram) and 2-3 (next-to-leading process) (right t-channel diagram).

- s-channel: involves the production of a time-like W ($Q^2_W > 0$) boson, which then decays to a top and a bottom quark.

- tW-channel: involves the production of a real W ($Q^2_W = m^2_W$) boson.

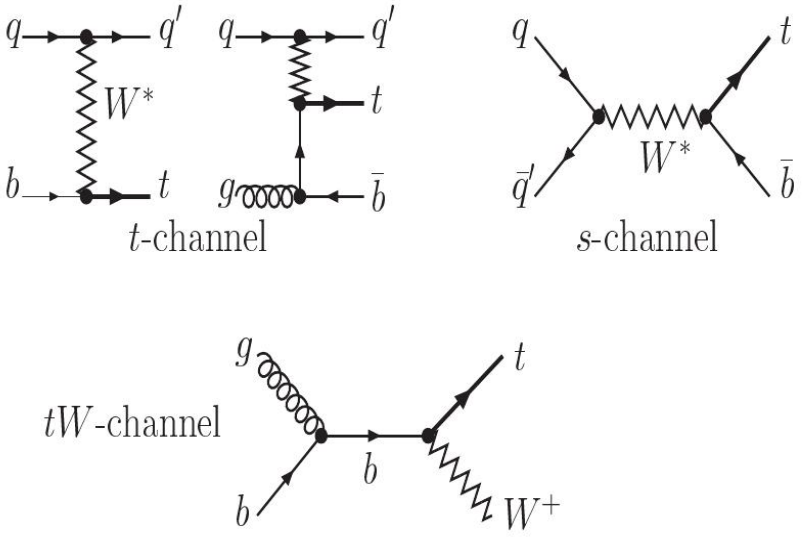


Figure 2.5: Feynman diagrams for single top production.

An initial state u, $\bar{d}$, $\bar{s}$, or c quark is required for t production, whereas $\bar{t}$ production requires an initial state $\bar{u}$, d, s or $\bar{c}$ quark. Since the LHC is a

proton-proton collider and the protons contain more valence u quarks than d quarks, the cross sections for t and $\bar{t}$ production are not equal in t-channel and s-channel. The NLO cross sections at $\sqrt{s} = 14\,\text{TeV}$ are 152.6 pb and 90.0 pb for the t-channel in t and $\bar{t}$ production, respectively, and 6.55 pb and 4.07 pb for the s-channel in t and $\bar{t}$. For the associated W production (tW) channel, the cross sections for t and $\bar{t}$ production are the same, about 60 pb [20]. At $\sqrt{s} = 10\,\text{TeV}$, NLO cross sections of t and $\bar{t}$ in t-channel are 85.786 pb and 47.306 pb, respectively [21]. For both t and $\bar{t}$, the cross section is the same, 29 pb in tW channel and they are 3.03 pb and 1.76 pb for t and $\bar{t}$, respectively in s channel [22].

Chapter 3

The CMS Experiment at LHC

3.1 Large Hadron Collider

The Large Hadron Collider (LHC) [23, 24] is a proton-proton (p-p) and lead-ion (Pb-Pb) collider, which is housed at CERN across the Swiss-French border. The LHC tunnel built in the existing Large Electron-Positron (LEP) [25] tunnel is located about 50 to 175 m underground. Its circumference is 27 km. It can collide protons at the center of mass energy of 14 TeV which will be the highest collision energy ever reached. Beside that, it also will collide lead (Pb) ions with energy of 2.76 TeV/nucleon. Particles will travel in two different pipes and collide in bunches at four nominal interaction points, where two general purpose detectors: Compact Muon Solenoid (CMS) [26, 27] and A Toroidal LHC Apparatus (ATLAS) [28] and two special-purpose detectors: Large Hadron

Collider beauty (LHCb) [29] and A Large Ion Collider Experiment (ALICE) [30] will be placed to collect the data of each physics event. Main objective of CMS and ATLAS is to perform detailed measurements of Standard Model physics, for example investigate QCD in multi-jet and top events, as well as observe and study new physics effects not described by the SM. LHCb will be specifically dedicated to b-physics, i.e., mainly to the study of CP violation in the B-sector in order to obtain precise measurements of the CKM mixing matrix. Finally, the fourth detector, ALICE, is focused on the properties of quark-gluon plasma in heavy ion collisions. This phase of matter is interesting, since it is believed to have existed during the first 20 or 30 microseconds after the Big Bang. The B-physics programme will be carried out at the low luminosity running of the LHC to avoid too many overlapping events. For the heavy ion programme, the proton beams in the LHC accelerator will be replaced by ion beams. The schematic picture of LHC is shown in Figure 3.1.

The linear accelerators (Linac2, Linac3), the booster, the Low Energy Ion Ring, the Proton Synchrotron (PS) and the Super Proton Synchrotron (SPS) are the components of injector complex at LHC. Firstly, Linac2 and Linac3 will accelerate protons up to 50 MeV, then booster will provide a kick them up to 1.4 GeV. In the PS and the SPS which has two fast pulsed magnet systems each of which produces magnetic pulses of 1.3 Tesla-meters with a risetime of at most 900 ns, they will gain the energy up to 25 GeV and then up to 450

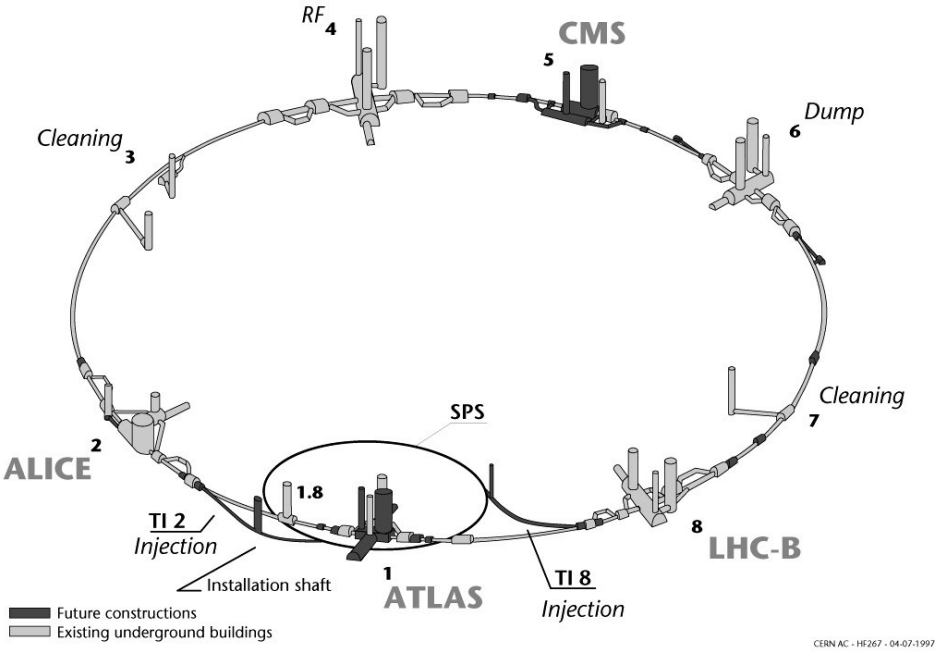


Figure 3.1: The structure and experiments of LHC

GeV, respectively. Finally, they will be injected from SPS into the LHC where they will reach their nominal energy of 7 TeV (for the proton beam). Twelve injections are performed for each counter-rotating beam. Approximately, 4 SPS cycles are necessary to fill the LHC taking $\sim$ 3 minutes. The magnetic field needed to make the protons orbit each ring at 7 TeV is 8.33 Tesla. To achieve this, the total number of magnets used around the ring is approximately 9300. The beams pass through 1232 dipole magnets each of which is 35 tonnes and 15 m long. There will be 8 RF cavities per beam and the field strength at peak energy is 5.5 MV/m. Superconducting magnets are operated at fluid He temperature which is $1.9°K$, so that the highest possible field is achieved at an

affordable power consumption. The operating temperature of the He will be provided by a huge cryogenics supply system. In total, 40000 of such cryogenic units will be placed around the 27 km circumference LHC ring. The cross section of the LHC dipole is shown in Figure 3.2.

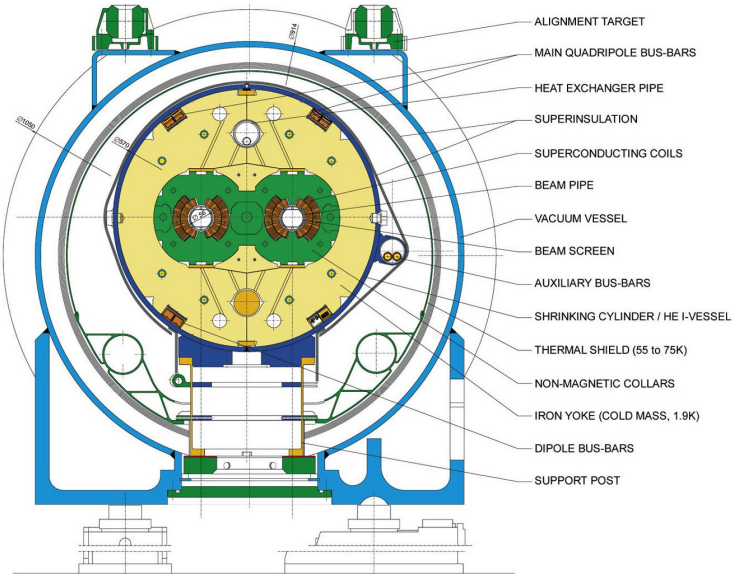


Figure 3.2: Schematic view of the cross section of the LHC dipole. Superconducting magnets surrounding the two beam pipes create strong field to bend the particle trajectory.

In LHC, the bunch structure is quite complicated. The separation of bunches in time is 25 ns and in space around 7.5 m which is maintained with trains of 72 occupied and 12 empty bunches. A longer spacing of 950 ns is allocated every 3-4 trains for LHC injections. The other spacing in the bunch structure are used for synchronization, calibration, and resetting the front-end-electronics. These

bunches will have transverse spread $\sigma_x = \sigma_y$= 15 cm and the bunch length, σ_z, will be 11.24 cm and 7.55 cm at injection and collision, respectively.

The event rate of physics processes can be computed through

$$R = \sigma \times \mathcal{L}\,, \tag{3.1}$$

where σ is the cross section and $\mathcal{L}$ is luminosity. The accelerator luminosity can be obtained by

$$\mathcal{L} = \frac{f {N_p}^2 F(\theta)}{4\pi\sigma_x\sigma_y} \quad \text{with} \quad F = \frac{1}{\sqrt{1 + (\frac{\theta_c\sigma_z}{2\sigma_z\sigma_y})^2}}\,, \tag{3.2}$$

f is collision frequency, N_p is the number of particles in the bunches and $F(\theta)$ is the factor for the luminosity reduction due to crossing angle, θ_c. In order to obtain the luminosity of $10^{34}\,\mathrm{cm}^{-2}\mathrm{s}^{-1}$, each beam along the LHC tunnel will have 2808 bunches with 10^{11} protons. The average number of inelastic p-p interactions expected during each beam crossing is about 20 at this full luminosity. In addition, the short bunch spacing of 25 ns results in further pile-up [1], which comes from the soft remnants overlapping from the two previous bunch crossings and some early effects from the subsequent one. The structure of the Pb beam does not impose such pile-ups; however, due to the number of nuclei involved at each collision event the detector will suffer from much higher particle occupancies.

[1] Pile-up events are the separate and soft partonic interactions in a single-bunch crossing

Table 3.1: Beam parameters for nominal proton and heavy ion runs.

beam parameter	p (high lumi.)	Pb	units
design luminosity	10^{34}	10^{27}	$\mathrm{cm}^{-2}\mathrm{s}^{-1}$
energy at collision	7	2.56	TeV
number of particles per bunch	1.15×10^{11}	7×10^{7}	
bunch spacing	25	9.98	ns
number of inelastic collision events per beam crossing	~ 20	~ 7	
number of pile-up events	$+1 - 2$	none	

Although the proton collision energy is 14 TeV, the maximum parton energy available will be $\sqrt{x_1 x_2 s}$ where x_1 and x_2 are the momentum fraction of proton's momentum carried by each parton in a frame in which the proton's momentum is large, and $\sqrt{s}$ is the center of mass energy. LHC will be able to probe the physics at several TeV. The high luminosity running leads to around 1 billion proton-proton interactions per second, since the total proton-proton cross-section at 7 TeV is $\sim$ 110 mb. This total cross-section can be separated in contributions from inelastic scattering (60 mb), elastic scattering (40 mb) which produce particles with very small angles to the beam axis, and single diffractive events (12 mb); it is only the inelastic scattering that causes particles to be generated at high angles with respect to the beam axis (high p_T values). In Figure 3.3 cross sections of different physics process at LHC are shown. For example $t\bar{t}$

production at the LHC with a center of mass energy of $\sqrt{s} = 14$ TeV gives a leading order (LO) cross-section of about 560 pb assuming a top mass of $M_t = 171\,\text{GeV}$. Calculations of the next to leading order (NLO) cross section predict about 908 pb [17].

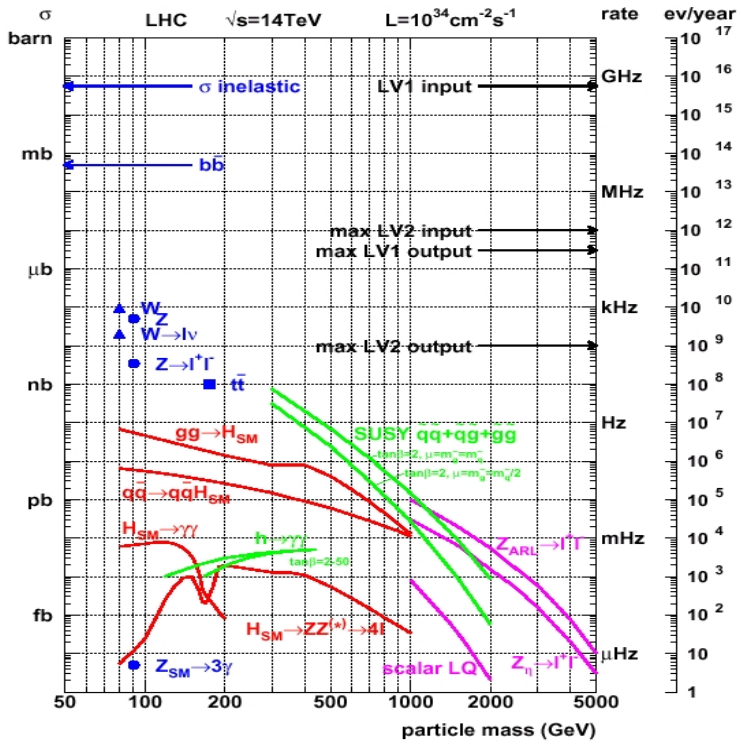


Figure 3.3: Cross section and production rate of different physics processes at LHC in different energy/mass scales.

3.2 CMS Detector

The Compact Muon Solenoid (CMS) is 4π general purpose detector that will be used at LHC. The CMS has 3 very important features, granulatiy, hermiticity and radiation hardness. The important physics events will have high transverse momentum objects, so high granularity is very essential to measure the position of objects precisely and also to separate the deposition of the object in interest in the pile-up and underlying events. Hermiticity is particularly important when noninteracting particles including those from possible new physics are involved, since their signature will be the missing energy of the entire system. Each sub-detector also has endcaps to ensure good coverage in the direction of the beams. The high luminosity LHC environment will cause an additional challenge to the sensors and the readout electronics, as they are required to survive the high radiation environment as well as to deliver fast enough response to tackle the collision rate of 40 MHz. The CMS, which is shape of a cylinder $\sim$ 21 m long and with a diameter $\sim$ 15 m, is very large and advanced detector made up of several sub-detectors, which are positioned in concentric layers around each other ('onion' structure) and each of them dedicated to different and complementary types of measurements. Starting from inside to outside, the CMS detector consists of the pixel detector, silicon tracker measuring charged particle trajectories in the magnetic field and hence their momenta, electromag-

netic calorimeter (ECAL) which measures the energy of electrons and photons, hadronic calorimeter (HCAL) which measures the energies of strongly interacting particles, superconducting coil, which deflects the charged particles so their momentas can be measured, the muon detectors which is used for muon identification and measurements of their momentum.

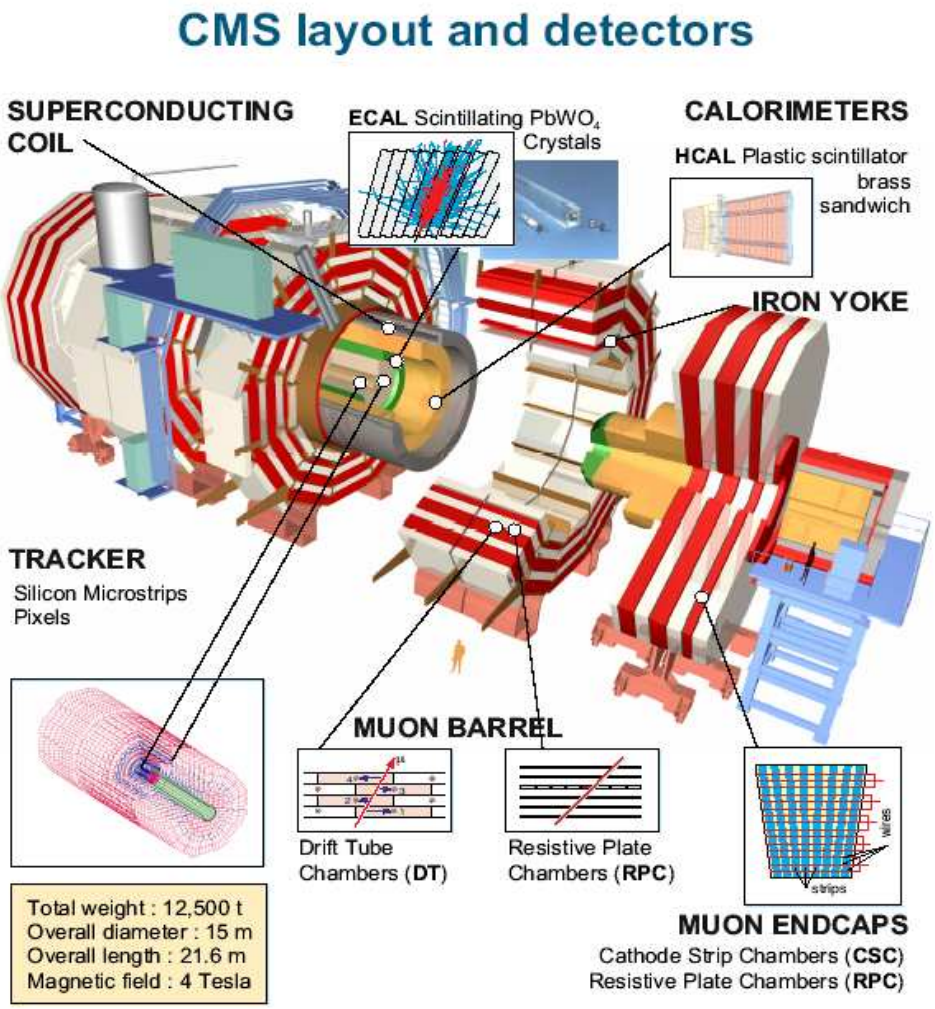


Figure 3.4: An exploded view of the CMS detector

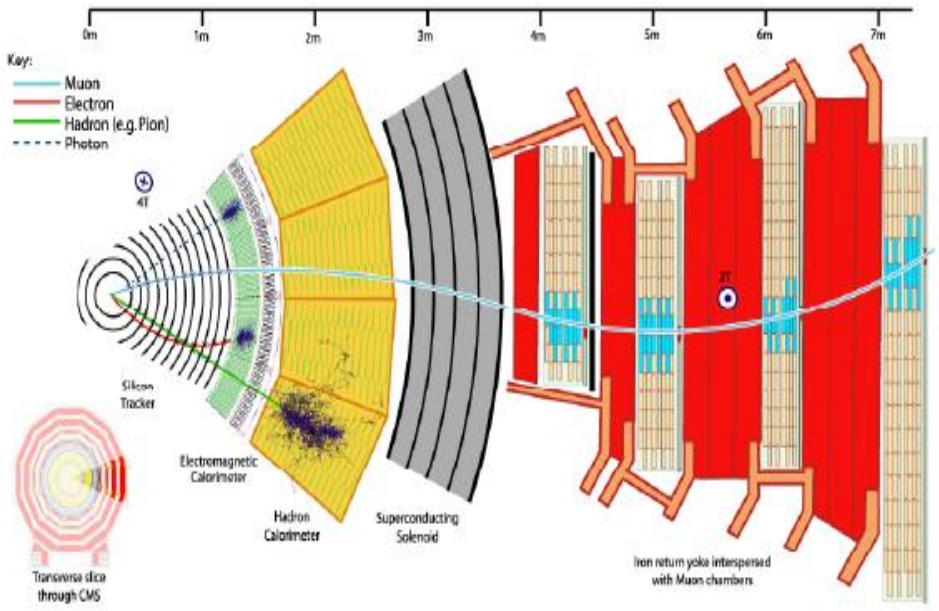


Figure 3.5: A schematic showing a transverse slice through the sub-detectors of the Compact Muon Solenoid, highlighting the paths taken by a number of particle types.

The CMS superconducting magnet generates 4 Tesla field (corresponding to about 2.7 GJ of stored energy) which is essential for having a high momentum resolution and distinguishing particles in high multiplicity events. An overall picture of the CMS can be seen in Figure 3.4.

Particles enter the CMS through both ends of the beam pipe, and timed such that two beams collide at its center. The outgoing particles from the interaction then pass radially through the concentric layers, as shown in Figure 3.5.

CMS is located on the collision point 5 at the LHC, see Figure 3.1. The coordinate convention is such that the z-direction is parallel to the beam line pointing to the north-west (at the Jura mountains), the y-direction is vertical, and the x-direction is horizontal and points to the center of the LHC ring. The center of the detector is the origin of the coordinate system. The azimuthal angle ϕ is defined with relative to the positive x-axis and the polar angle θ is defined relative to the positive z-axis. The pseudo-rapidity can be defined as $\eta = \ln(\tan(\theta/2))$. Thus, the momentum and energy measured transverse to the beam direction, denoted by $p_T = p\sin\theta$ and $E_T = E\sin\theta$, respectively, are computed from the x and y components.

3.2.1 Tracking System

The CMS tracker is designed to reconstruct high p_T muons, electrons, and hadrons with high momentum resolution and efficiency and to measure the decay

vertices of long-living unstable particles. Therefore, the all-silicon approach has been chosen for the tracking system. The tracking system is composed of finely segmented silicon sensors (pixels and strips) which measure the momenta of charged particle and track them through ionization they produce along their paths. The tracker system consists of a single detector in the barrel and two in the endcaps. In the barrel part, there are three pixel layers and ten silicon strip layers. Four of the 10 silicon strip layers make the Inner Barrel (TIB) and 6 of them form the Outer Barrel (TOB). In the endcaps, there are two pixel layers and three inner disk (TID) and nine outer forward silicon disk detectors which enable the coverage to go up to $|\eta| = 2.5$. The tracking system reconstructs high p_T with resolution of $\delta P/P \approx [15(P_T/\,\mathrm{TeV}) \oplus 0.5]\%$ for $|\eta| < 1.6$ and with the resolution of $\delta P/P \approx [60(P_T/\,\mathrm{TeV}) \oplus 0.5]\%$ as it approaches to $|\eta| = 2.5$. The layout of CMS tracking detectors is shown in Figure 3.6. A detailed description of the entire CMS tracker design can be found in Reference [31].

Pixel tracker

The pixel tracker has 3 barrel layers: 4.4 cm, 7.3 cm and 10.2 cm from the beam-pipe with a length of 53 cm and 2 endcap discs spreading from 6 cm to 15 cm in radius, placed on each side at |z| = 34.5 cm and 46.5 cm. 66 million pixels of size $\sim 100 \times 150\,\mu\mathrm{m}^2$ are arranged across 768 and 672 modules in the barrel and endcaps, respectively. To maximize vertex resolution an almost square

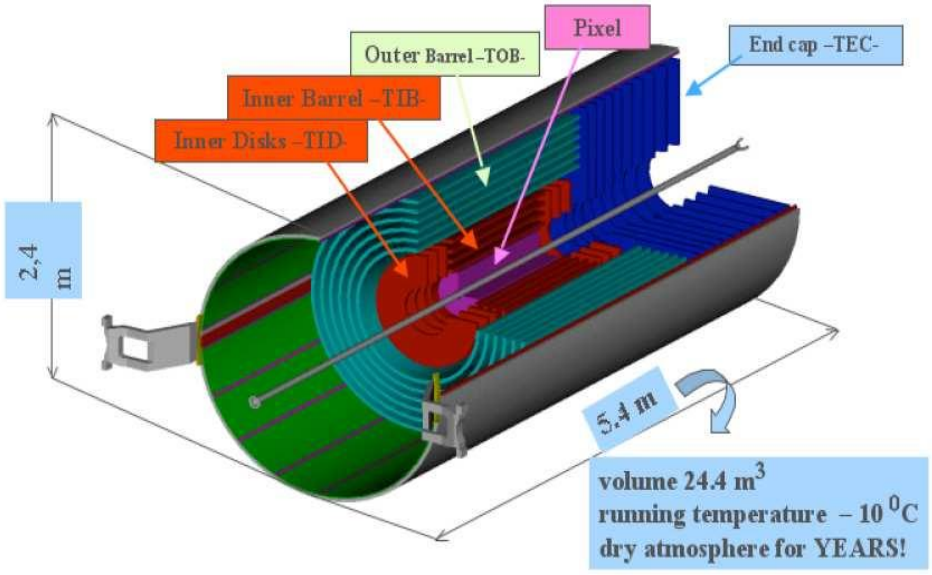


Figure 3.6: Layout of CMS tracking system

pixel shape has been adopted. A Lorentz angle of 23° in the barrel improves the $r - \phi$ resolution through charge sharing. The endcap discs are assembled with a turbine-like geometry with blades rotated by 20° to also benefit from the Lorentz effect. The resultant spatial resolution is 10 μm in $r - \phi$ and 20 μm in z, allowing a primary vertex resolution of ∼40 μm in z-axis. The layout of pixel detector can be seen in Figure 3.7

Strip tracker

The particle flux is low enough to justify the use of a Silicon Strip Tracker (SST) outside the pixel detector. Here, 9.6 million microstrips are divided between six regions: a TIB, two TID, a TOB and two endcaps (TEC). The basic unit of

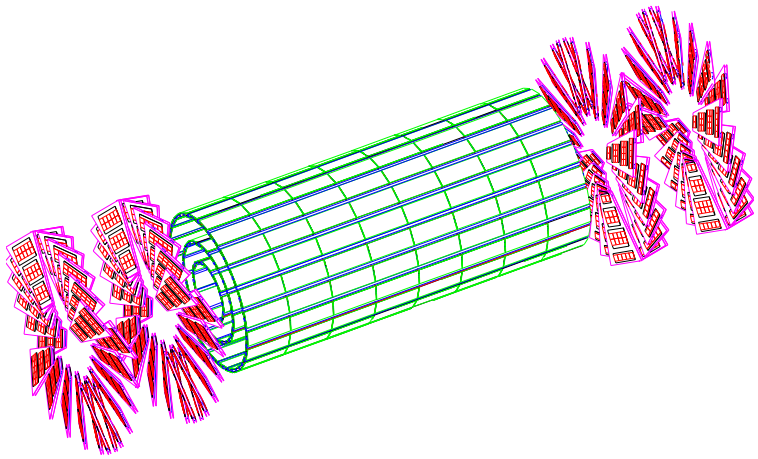


Figure 3.7: A schematic of the pixel tracker.

this sub-detector is called a module, each housing 512 or 768 strips,

The Silicon Strip Tracker is composed of almost 15400 modules, mounted on carbon-fiber support structures. The silicon strip length is set to 11.9 cm for radii < 59 cm and 18.9 cm beyond. The longer detectors are thicker (500 μm) than the shorter ones (320 μm) to maintain a constant signal/noise. Barrel and endcap strips lie along the z and radial directions, allowing precise measurement of the r and ϕ and the z and ϕ coordinates, respectively. To improve the track resolution and resolve tracking ambiguities, some double sided modules are used, each of which consists of a regular module and a stereo counterpart angled at 100 mrad back-to-back. They provide a three-dimensional hit measurement in r, ϕ and z. This layout allows the tracker to provide 8 to 14 hit measurements

for high momentum tracks.

3.2.2 Electromagnetic Calorimeter

The Electromagnetic Calorimeter (ECAL) which has been designed to measure the electromagnetically interacting particles photon and electrons with high precision is a hermetic, homogeneous detector. It has been also optimized to discover the Higgs boson, because a good energy resolution is necessary to separate $H_0 \rightarrow \gamma\gamma$ from the large $\pi_0 \rightarrow \gamma\gamma$ background. The ECAL is scintillating detector in which scintillation light is emitted with a time scale on the order of the LHC bunch crossing time (25 ns),

ECAL, which is made up of Tungstate ($PbW0_4$) crystal of high density (8.3 g/cm^3), is composed of almost 61200 crystals in ECAL barrel (EB) and 7324 in ECAL endcaps (EE). The reason why Tungstate crystal is chosen as sensitive material is because it has short radiation length (X_0) [2], $X_0 \simeq 0.89$ cm, small Moliere radius [3] of 2.2 cm and radiation hardness. The distance of the front face of the EB crystals to the interaction point faces is 1.29 m. A picture of crystal is given in Figure 3.8.

In the barrel part, each crystal, 23 cm long equivalent to $\sim$ 26 radiation

[2]Radiation length, X_0, is the average length in a specific material in which a relativistic charged particle will lose 67% of its energy by bremsstrahlung.

[3]Moliere radius is the radius of a cylinder containing on average 90% of the shower's energy deposition.

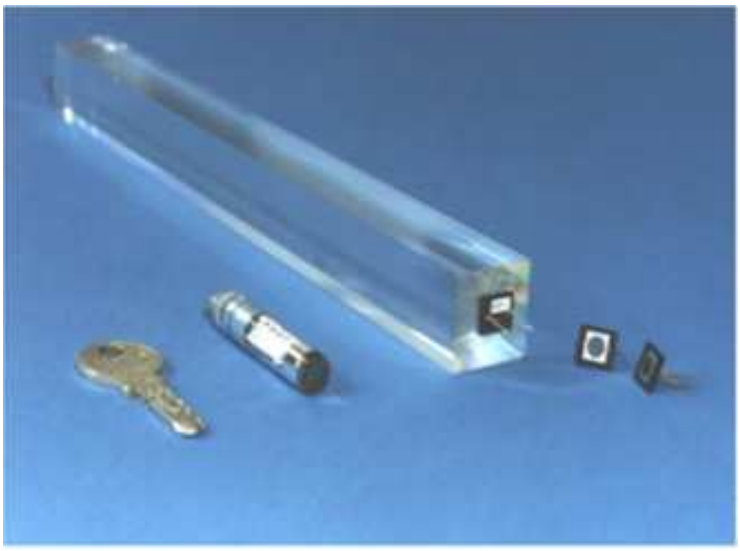


Figure 3.8: A sample of a lead tungstate crystal is shown.

lengths (X_0), covers $\Delta\eta \times \Delta\phi = 0.0174 \times 0.0174$ corresponding to $22 \times 22\,\mathrm{mm}^2$ at the front face and $26 \times 26\,\mathrm{mm}^2$ at the back. The EB covers up to $|\eta| = 1.48$. In order for the particles not to escape between the inter-crystal dead areas, the crystals are tilted 3° with respect to pointing axis originating from interaction point.

Crystals are grouped into sets of 2×5 titled submodules. A set of 10×17 submodules forms a single supermodule. The geometry an η coverage of subcomponents of ECAL is illustrated in Figure 3.9.

The endcap part covering a pseudorapidity $1.48 < |\eta| < 3.0$ contains 14648 crystals. The distance of the front face of EE crystals to the interaction point is 3.14 m. Endcap crystals are 22 cm long equivalent to $24.7X_0$ with a front-face

of $2.86 \times 2.86\,\mathrm{cm}^2$ corresponding to $\Delta\eta \times \Delta\phi = 0.0175 \times 0.0175$ and back face of $30 \times 30\,\mathrm{mm}^2$ corresponding to $\Delta\eta \times \Delta\phi = 0.05 \times 0.005$. Again, all are tilted in the same way that they make an angle of 3° with pointing axis. Crystals are grouped into 5×5 arrays called supercrystals, which in turn are grouped into 4 quadrants. There are 2 preshower detectors sitting in front of each endcap. They cover $1.48 < |\eta| < 2.6$. These are designed to help electron identification and to improve rejection of $\pi_0 \to \gamma\gamma$ decaying into two closely separated photons, which is fulfilled by resolving the low opening angle between photons in this region. The preshower detector are sampling calorimeter with 2 layers. The first layer consists of lead radiators, and the second layer is composed of silicon strip sensors behind each radiator.

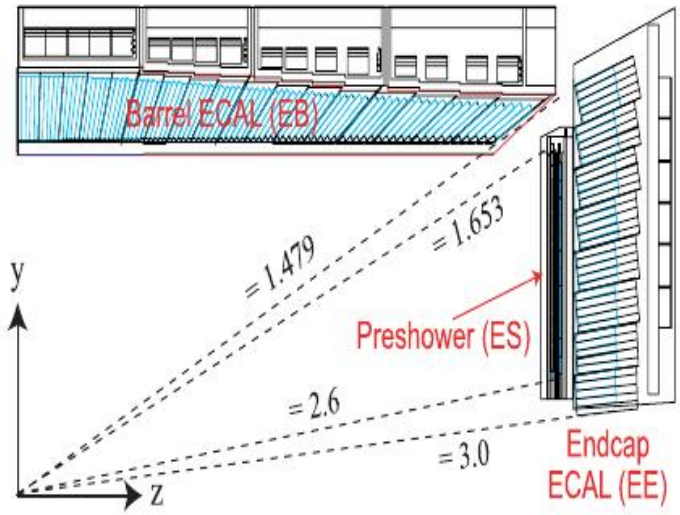


Figure 3.9: A layout of one quarter of ECAL in the $r - z$ projection

The energy resolution of ECAL can be parameterized by Equation

$$\frac{\sigma}{E} = \frac{S}{\sqrt{E}} \oplus \frac{N}{E} \oplus C \,, \tag{3.3}$$

where S is the stochastic uncertainty in the signal generating process, N is the electronic noise and C is constant term which represents uncertainties in energy leakage through the rear of the crystals inter-crystal calibration and non-uniformity of light collection along the crystal. S and N terms drop at high energies, which make the C constant term dominant. For good precision physics studies, C constant term is required to be no more than 0.5%. From test beam measurement, the terms are found as follows: $N = 124$ MeV, $S = 3.63\%$ and $C = 0.26\%$. Further details can be found in the ECAL TDR [32].

3.2.3 Hadronic Calorimeter

The CMS Hadronic Calorimeter (HCAL) is designed to detect jets and measure their energies. It also complements identification of electrons, muons and photons, besides that, it plays an important role in the identification of neutrinos by measuring missing energy. HCAL is a sampling calorimeter made of plastic scintillator tiles interleaved with brass absorber plates. The reason why brass has been chosen as absorber material is because it has short enough interaction length [4], is easy to machine and nonmagnetic. The energy measurement is

[4]Interaction length, λ_I, is the mean path length required to reduce the energy of relativistic charged particles by the factor 1/e, or 0.368, as they pass through matter.

made through ionization which is converted to electrical signal and then digitized. HCAL is housed behind ECAL with the HCAL barrel (HB) and HCAL endcap (HE) subdetectors. HB, which is composed of 32 towers covering pseudorapidity of $|\eta| < 1.48$, has total number of 2304 towers with the segmentation $\Delta\eta \times \Delta\phi = 0.087 \times 0.087$. It has a length of 9 m and and extends from 1.8 m to 2.9 m in the radial direction. HE, which covers the region $1.48 < |\eta| < 3.0$, has also same number of towers as HB does. Its inner and outer radii are 0.4 m and 3 m, respectively. Since the main purpose of HCAL design is to provide good containment and hermiticity for missing energy measurement and to reduce the non-Gaussian tails in the energy resolution, material inside the magnet coil is maximized in terms of interaction length (λ_I). The thickness of the HB is $\sim 5\lambda_I$ along which hadron shower can not be fully contained. Therefore, an additional layer of scintillators known as hadron outer (HO) is placed outside the magnetic coil extending to $|\eta| = 1.26$. They increased the effective thickness of hadron calorimeter of $\sim 11\lambda_I$. The blue light produced in the scintillators are wavelength shifted to green by wavelength shifting (WLS) fibers embedded in the scintillator tile grooves. The light collected from all the tiles of a tower are channeled to Hybrid Photo Diode (HPD) photo-detectors that convert the light to electrical signals and then amplified. The channeling is done by clear fibers into the same pixel of an HPD. HPDs are capable of operating at high magnetic fields (up to 4 Tesla) perpendicular to the surface of the HPD. Clearly, all the

front-end electronics must be able to operate at high CMS magnetic fields and high neutron flux ($\sim 10^{11}$ cm^{-2}).

The performance of the combined EB+HB system is measured in test beams. The energy resolution of the combined EB+HB system for beam momenta in $2 - 300$ GeV range, can be parameterized as

$$\frac{\sigma}{E} = \frac{0.71}{\sqrt{E}} \oplus \frac{0.97}{E} \oplus 0.08\,. \tag{3.4}$$

when both EB and HB are calibrated by 50 GeV electrons.

Forward Calorimeter is placed at a distance of 11.15 m from the interaction point and has an outer radius of 1.3 m with a cylindrical hole at its center to accommodate the beam pipe. It covers pseudorapidity of $3.0 < |\eta| < 5.0$. It is optimized for measuring high energy jets. Each HF module consists of 18 wedges, each wedge covering a 20° azimuthal angle. There are 13 towers in η with $\Delta\eta \approx 0.175$ except for the first tower with $\Delta\eta \approx 0.111$ and last tower with $\Delta\eta \approx 0.3$. In the ϕ direction, segmentation for all towers is 10° except the last two towers which cover 20°. In total, there are 900 towers and 1800 channels in the 2 HF modules. HF along with HB and HE provides hermetic coverage, so that more precise missing energy measurement as well as measurement of forward jet energy can be made. These features of HF play a crucial role in search of Standard Higgs, Supersymmetric (SUSY) particles and top quark. For example, Higgs boson which is generated through WW

or ZZ production mechanism can only be detected by two forward jets in the region $3.0 < |\eta| < 5.0$. Likewise, HF is very important for search of the SUSY particle. As HF will receive a high radiation dose about 0.1 GRad/year, it uses radiation-hard quartz fibers as the active medium, and steel absorbers, composed of 5 mm thick grooved plates for the absorber. Signals in the fibres are generated Cerenkov Radiation resulting from relativistic charged particles in the electromagnetic component of the showers surpassing Cherenkov thresholds [33] and then channeled by the fibres to photomultipliers. Charged hadrons are detected mainly through π^0 production. Since there are difference responses for electrons and pions, HF utilizes two different length (143 cm and 165 cm) of quartz fibres which are placed 5 mm apart in a square grid and read-out separately. With two different length of fibers, it is possible to distinguish the electromagnetic and hadronic showers in HF.

The HF calorimeter in which signals in the fibres are produced is not sensitive to neutron and radioactive nucleus, and very responsive to high energetic particles. Stochastic and constant terms in the HF energy resolution are determined in test beams. When the long and short fiber sections are used, the stochastic and constant terms for the electromagnetic energy resolution are 198% and 9%, respectively, and 280% and 11% for the hadronic energy resolution [34]. Photoelectron statistics of the photomultiplier dominates the electromagnetic energy resolution, and π^0 fluctuations dominate the hadronic energy resolution.

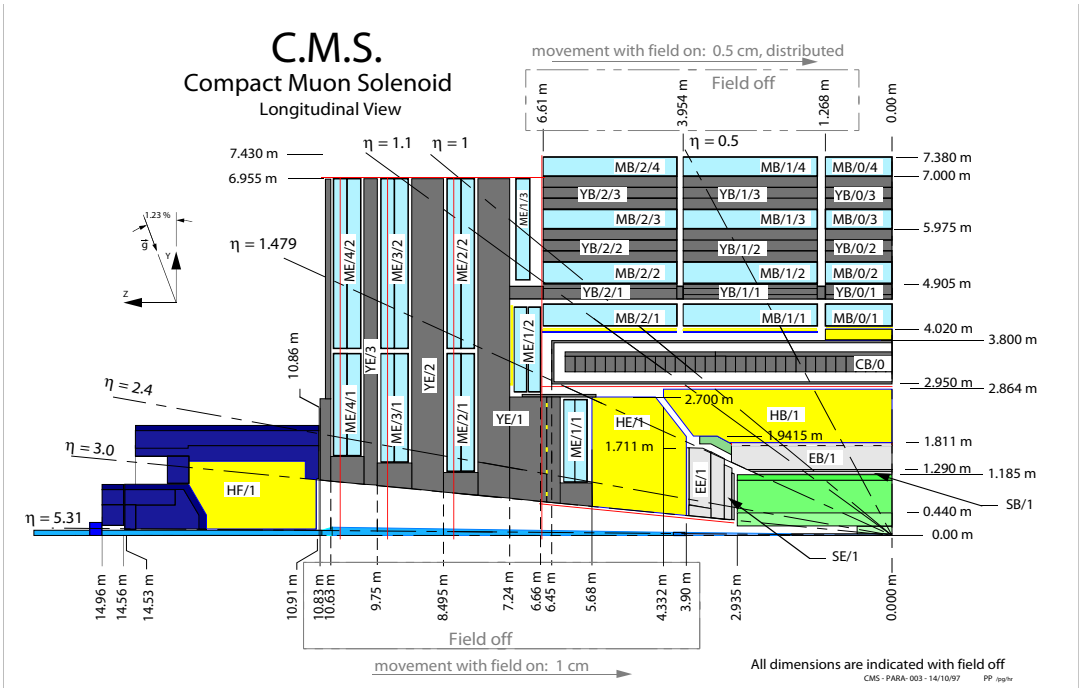


Figure 3.10: Longitudinal view of a quarter of the CMS detector. HCAL consists of HB, HE, HF and additional scintillator out the magnet coil (HO)

3.2.4 Magnet

Large superconducting solenoid with a radius of ~ 3 m produces uniform 4 Tesla magnetic field, required to achieve a muon momentum resolution of $\sim 10\%$ at a momentum of 1 TeV. It is designed to contribute information on particle momenta from the bending of the tracks. Except for the outer hadron calorimeter (HO), the calorimeters and the tracking detectors are situated within this coil to minimize resolution loss as the particles pass through. The iron return yoke

interspersed with muon chambers, returns the magnetic flux. Details on the CMS magnet can be found in the Magnet TDR [35].

3.2.5 Muon System

The muon system is the tracking device situated in the outermost region of the CMS detector, where trajectories of muons, the only particle flavor (except neutrinos) to penetrate the calorimeter, in the region $|\eta| < 2.4$, is recorded. The challenge of the muon system is to provide fast recognition, efficient reconstruction and online background suppression, which are required for triggering purposes. There are four layers of muon stations in the barrel and the endcaps interleaved with the iron return yokes, each providing track segments reconstructed from a few distributed hits. These will later be combined with information from the inner silicon tracking system to form complete muon tracks [36].

The CMS muon system employes three different types of detectors, the drift tubes (DT) in the barrel $|\eta| < 1.2$, cathode strip chambers (CSC) in the endcaps $0.9 < |\eta| < 2.4$. Both assisted by resistive plate chambers (RPC) located at barrel and endcaps $0 < |\eta| < 2.1$. The DT and CSC detectors are used to obtain a precise position measurement. The DT layers provide a final spacial resolution of 100 μm and the CSCs provide 80-450 μm depending on the station. The RPCs are dedicated trigger detectors with good timing resolution of ~ 3

ns that are not used for tracking except for resolving ambiguities [36].

DTs assembled in drift chambers containing 12 layers of tubes are aluminum tubes with a stainless steel wire in the middle. There are four stations of chambers, interleaved in the iron yoke plates. Every chamber has 12 planes of DTs which are organized in three independent sub-units made up of four planes with parallel wires. Two sub-units measure the coordinate in the bending plane, the third measures the track coordinate along the beam. Measurements in a chamber are combined to form an oriented segment used later on for track reconstruction.

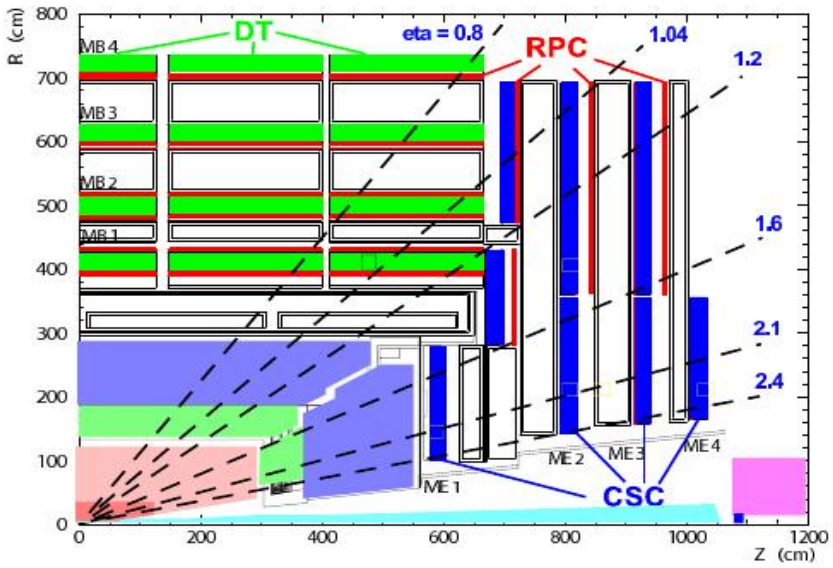


Figure 3.11: A schematic of one quadrant of the muon system. Drift Tubes (DT), Resistive Plate Chambers (RPC) and Cathode Strip Chambers (CSC). are shown.

In both endcaps, instead of DTs, CSCs are employed. CSCs are multiwire proportional chambers where the cathode is subdivided into strips perpendicular to the anode wires. The forward environment is indeed very different from the central one, since the high particle flux requires a finer granularity and a faster response. Moreover, CSCs can sustain the highly varying magnetic field present in this transition region between the solenoid and the return yoke. RPC are used in both the barrel and the endcaps. They are slightly faster, more robust, but have a less good spatial resolution. A RPC consists of two parallel resin plates, with a high bulk resistivity , separated by a gas-filled gap of a few millimeters. On the outside, electrodes are made of conductive graphite paint. Avalanches in the gas induce a fast charge on the cathodes, that can be exploited without costly electronics. RPCs complement drift tubes and CSCs, acting as additional sensitive planes in higher trigger levels and offline reconstruction.

In total, the muon system has 250 DTs, 540 CSCs and 912 RPCs.

The muon system can provide very pure muon sample with no loss and identifying narrow physics signal peaks over backgrounds. The muon system (combined with the tracker) can identify muons with high efficiency and with good momentum resolution in $|\eta| < 2.5$. The momentum resolution is limited by the bending angle measurement which depends on the accuracy of the tracking and multiple scattering. The resolution is directly proportional to the square root of the amount of material in the muon system in units of X_0. For high p_T

($\sim 1\,\text{TeV}$), the momentum resolution is proportional to the spatial resolution of the muon chambers. Up to the last muon station the thickness of the absorber is 16 λ_I, up to $|\eta| \sim 2.5$. Good muon identification is achieved by absorption of charged particles before the muon system in ECAL and HCAL.

3.2.6 Trigger

Because of huge data volume at LHC, the pre-selection of events has to be carried out online by the triggers and the Data Acquisition (DAQ) system. About 20 inelastic p-p events are produced at each bunch crossing at full LHC luminosity. However, only a small fraction of them are hard scattering interactions containing physics processes of interest, and the rest are underlying events minimum bias events, generally containing soft jets of hadrons. The CMS detector produces $\sim$ 1 MB of data at each crossing (25 ns). Only a small portion of the data can be kept since current storage capacity is limited to about $\sim$ 100 MB/s or about 100 crossings per second. Hence, a Trigger and Data Acquisition (DAQ) system is required to select the interesting data with a rejection factor of $\sim 10^6$. At CMS, the events are filtered in two stages; using Level-1 (L1) and High-Level Triggers (HLT).

The L1 triggers first reduce the event rate from 40 MHz to 100 kHz (50 kHz at low luminosity), discarding any low p_T events. The L1 trigger uses custom electronics with programmable chips, which will be located inside the counting

room next to the underground interaction hall. 3.2 second is needed by the L1 trigger to come to a decision to store or not to store the data. This time is mainly governed by the time needed for a signal to be transferred from the front-end electronics to the L1 logic system. The time needed for the trigger calculations is less than about 1 μs. The data wait in the pipe-line buffers for 3.2μs/25 ns = 128 bunch crossings before it is decided that it will be kept or not.

The L1 trigger uses calorimeter, muon system, and global (combination) triggers, that combine the data from calorimeters and the muon system. The trigger-primitive objects (photons, electrons, muons and jets) are constructed using the detector systems. These objects are created only if the p_T or E_T are above some thresholds. Also, the sum E_T and missing transverse energy ($\not{E}_T$), which are determined globally, are included as trigger primitive objects.

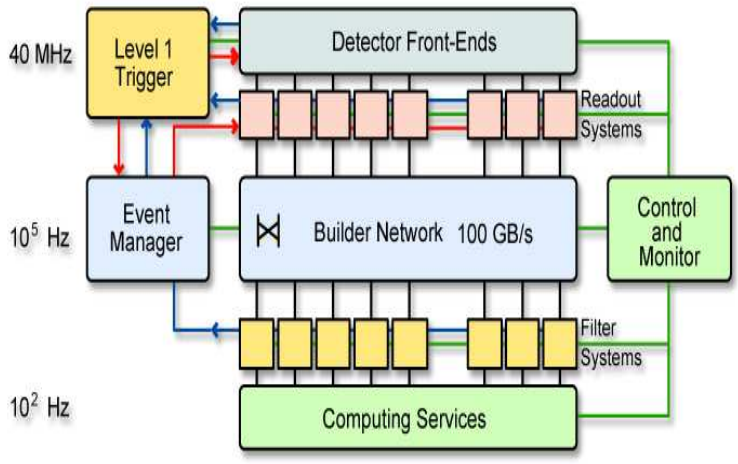


Figure 3.12: The CMS DAQ system.

HLT reduces the 100 kHz L1 event rate to $\sim$ 100 Hz. All calculations beyond L1 are performed in a single filter farm of about 1000 dual-CPU computers. The HLT is highly flexible when it comes to changes in the decision trees. HLT first does partial event reconstruction using the calorimeters and the muon system. At this stage, it refines the objects created at L1. Then it combines the data from pixel and tracker for further rejection. The design of the HLT makes it possible that the offline reconstruction algorithms can be used in the HLT. The schematics of the CMS trigger and DAQ system are displayed in Figure 3.12 For further details, see the trigger CMS technical design reports [37] [38]

Chapter 4

Measurement of Spin Correlation in Top Quark

4.1 Spin Correlation in $t\bar{t}$

4.1.1 Introduction

The top quark decays before either hadronization, governed by the scale $1/\wedge_{QCD}$, or depolarization governed by the scale $\wedge^2_{QCD}/m_t$, can take place. Moreover, the top quark spin flip time is much larger than its lifetime and the probability of a spin flip due to emission of one or several gluons via chromomagnetic dipole transition is very small. Therefore, the spin properties of the top and anti-top quarks (t and $\bar{t}$) are reflected directly in the angular distribution of the jets, W

bosons, or leptons into which they decay. These distributions are determined by t and $\bar{t}$ polarizations and spin correlations induced by the production mechanisms and depend on the interactions responsible for their decay. Hence, the analysis of these distributions will be an important tool to obtain detailed information about the top quark spin and possible deviations from the Standard Model (SM) couplings. The present measurement of spin correlation performed at Tevatron is limited by the small sample of top quarks collected [39].

The dominant SM top quark decay mode is $t \rightarrow W^{+}b$; $W \rightarrow l^{+}\nu$ or $W \rightarrow q\bar{q}$. The top spin polarization can be analyzed through the angular distribution of its decay products [40]

$$\frac{1}{N}\frac{dN}{dcos\theta_f} = \frac{1}{2}\left(1 + \kappa_f \, cos\theta_f\right), \tag{4.1}$$

where θ_f is the angle between the direction of particle f in the top quark rest frame and the direction of the top spin vector (in the helicity basis, chosen for this analysis, this is the direction of the momentum of the top quark in the $t\bar{t}$ center-of-mass frame). The distributions for spin-down and spin-up top quarks differ in the sign in front of the $cos\theta_f$ term. The degree to which a decay product is correlated to the spin of the parent top quark is encoded in the spin analyzing power κ_f of the particle [41]. Charged leptons and d-type quarks, which are almost 100% correlated with the top spin direction, are optimal spin analyzers. Table 4.1 gives the spin analyzing powers for several top decay daughter particles

at leading order (LO) and next-to-leading order (NLO) [42].

Table 4.1: Spin analyzing power κ_f of the top quark daughter particles.

particle	b	W^+	l^+	$\bar{s}, \bar{d}$	$u, \bar{c}$	lower energy q
κ_f (LO)	-0.41	0.41	1	1	-0.31	0.51
κ_f (NLO)	-0.39	0.39	0.998	0.93	-0.31	0.47

When top quarks are produced in pairs, they are essentially unpolarized [43]: spin-up and spin-down top quarks are produced in equal numbers. However, there is an asymmetry when the top and anti-top quarks are examined as a pair. In general, the number of pairs where both quarks have spin up or spin down ($N_{||}$) is not equal to the number of pairs where one quark is spin up and the other is spin down (N_X). Then, correlations can be seen in the so called opening angle distribution [44]

$$\frac{1}{N}\frac{dN}{dcos\phi} = \frac{1}{2}\left(1 - D\, cos\phi\right), \tag{4.2}$$

where ϕ is the angle between the flight directions of any two chosen decay products defined in the t and $\bar{t}$ rest frames, respectively, and D is the $t\bar{t}$ spin correlation, which is related to $\langle \mathbf{S_t} \cdot \mathbf{S_{\bar{t}}} \rangle$, where $\mathbf{S_t}, \mathbf{S_{\bar{t}}}$ are the spin operators of the t and $\bar{t}$, according to the formula [44]

$$D = \frac{1}{3}\kappa_1\kappa_2\langle \mathbf{S_t} \cdot \mathbf{S_{\bar{t}}} \rangle\,. \tag{4.3}$$

Using

$$\mathbf{S_t} \cdot \mathbf{S_{\bar{t}}} = \sum_{i=1} (\mathbf{S_t} \cdot \hat{\mathbf{e}}_\mathbf{i})(\mathbf{S_{\bar{t}}} \cdot \hat{\mathbf{e}}_\mathbf{i}) \,, \tag{4.4}$$

where $\hat{\mathbf{e}}_{i=1,2,3}$ forms an arbitrary orthonormal basis (for instance in the x, y, z directions), D can be represented in terms of a sum over double spin asymmetries

$$D = \frac{1}{12} \kappa_1 \kappa_2 \sum_{i=1}^{3} A_i \,, \tag{4.5}$$

where

$$A_i = 4 \langle (\mathbf{S_t} \cdot \hat{\mathbf{e}}_\mathbf{i})(\mathbf{S_{\bar{t}}} \cdot \hat{\mathbf{e}}_\mathbf{i}) \rangle = \frac{N(t_\uparrow \bar{t}_\uparrow) + N(t_\downarrow \bar{t}_\downarrow) - N(t_\uparrow \bar{t}_\downarrow) - N(t_\downarrow \bar{t}_\uparrow)}{N(t_\uparrow \bar{t}_\uparrow) + N(t_\downarrow \bar{t}_\downarrow) + N(t_\uparrow \bar{t}_\downarrow) + N(t_\downarrow \bar{t}_\uparrow)} \,, \tag{4.6}$$

and $N(t_{\uparrow/\downarrow} \bar{t}_{\uparrow/\downarrow})$ denotes the number of events for top quark pair with spins up or down with respect to axis i in the chosen orthonormal basis.

Unfolding D for the spin analyzing power of the daughter particles, κ_1 and κ_2, the 'spin asymmetry coefficient' can be defined as

$$A_D = \frac{\sum_{i=1}^{3} A_i}{12} = \frac{D}{\kappa_1 \kappa_2}. \tag{4.7}$$

In this study, A_D is measured in the semileptonic $t\bar{t}$ decay channel, when one W decays leptonically and the other hadronically. Two opening angles with the highest correlations are considered: the angle between the lepton (muon) from the leptonic side and the b quark from the hadronic side ($\phi_{l\text{-}b}$), and the angle between the muon and the low energy light quark from the hadronic side ($\phi_{l\text{-}q}$).

The ALPGEN [45] Monte Carlo (MC) event generator for hard multiparton processes in hadronic collisions at LO is used to estimate the spin correlation in the $t\bar{t}$ decay products. The κ_f values at LO level for daughter particles lepton, b quark and q(lower energy) are 1,-0.41 and 0.51, respectively. The κ_f for q(lower energy) is estimated as a statistical average for the lower energy jet, since the flavor of the light quark is not determined in jet measurements. The opening angle distributions generated by ALPGEN and using the CTEQ5L Parton Distribution Function (PDF) are presented in Figure 4.1.

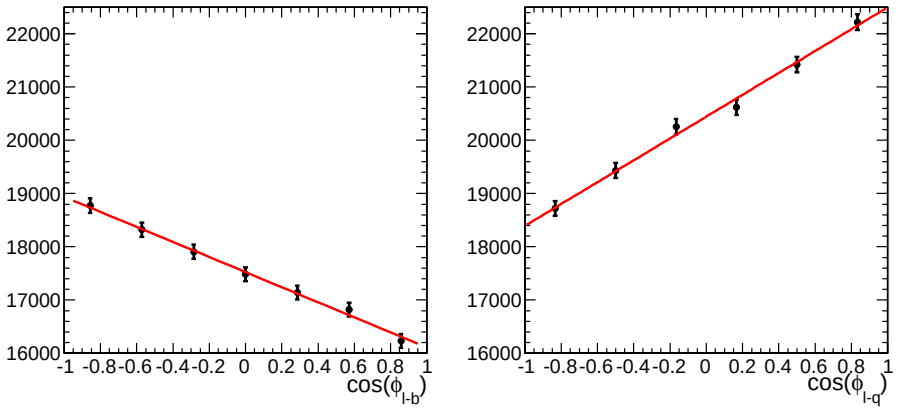


Figure 4.1: ALPGEN generated opening angle distributions. The number of events corresponds to an integrated luminosity of $2\,\mathrm{fb}^{-1}$. Left: cosine of lepton-b quark. Right: cosine of lepton-lower energy q.

Both angular distributions shown in Figure 4.1, are fitted globally according to Formula 4.2 and 4.7 with the following function:

$$P_1\,(1 + P_2\,cos\phi)\ . \tag{4.8}$$

From parameter P_2 and using the appropriate κ_f values, the asymmetry coefficient A_D is found to be:

$$A_D = 0.196 \pm 0.008 \tag{4.9}$$

The $t\bar{t}$ MC event samples used in this study (see Section 4.1.2) are also produced at LO. Therefore, using the LO spin analyzer values (Table 4.1) the LO spin asymmetry coefficient will be measured. Note that the spin correlation in $t\bar{t}$ production estimated at NLO is found to be close to that at LO [44].

4.1.2 Software and Monte Carlo Event Samples

In this analysis, event generation, detector simulation and physics reconstruction have been carried out using the CMS data model and software framework CMSSW [46]. Specifically, the `CMSSW_2_2_X` release along with the dedicated software packages *Top Quark Analysis Framework* (TQAF) [47] and *Physics Analysis Tool* (PAT) [48] are used. The alignment and calibration are assumed to be perfect (ideal scenario) in the detector simulation.

At 10 TeV, the estimated cross section for $t\bar{t}$ production at NLO is 414 pb [17]; for an integrated luminosity of 2 fb^{-1} this gives rise to 122666 events in the semileptonic final state, where in the leptonic branch only muon (12/81 branching fraction) is considered. This represents the "signal sample" in this analysis.

The background processes considered are the following:

- $t\bar{t}$ final states different from those treated as the signal,
- W+jets (leptonic: $W \to l\nu, l = e, \mu, \tau$) and Z+jets (leptonic: $Z \to l^+l^-$),
- single-top t-channel (leptonic: $W \to l\nu$) and single-top in associated production with a W boson (tW),
- QCD: `InclusiveMuPt15` ($\hat{P}_T > 20\,\text{GeV}$, $P_T^\mu > 15\,\text{GeV}$) and `InclusiveMu5Pt50` ($\hat{P}_T > 50$ GeV, $P_T^\mu > 5$ GeV) samples.

The MadGraph MC [49] event generator is used to generate the $t\bar{t}$, W+jets, Z+jets and single-top (tW and t) event samples. The simulation of QCD processes is performed with the pythia [50] MC. Note that the MadGraph $t\bar{t}$ event production was done without the full $t\bar{t}$ spin correlations and consequently the opening angle $\phi_{l\text{-}b}$ and $\phi_{l\text{-}q}$ distributions are flat. To account for the spin correlations, the MadGraph $t\bar{t}$ signal events are weighted according to the alpgen opening angle distributions shown in Figure 4.1.

In order to have two statistically independent samples, the MC event samples are separated into two subsamples: one, full-simulation, is regarded as the "analysis" subsample used for the measurement of spin asymmetry coefficient; the other, fast-simulation (except for single-top samples which are full-simulation), is regarded as the "reference" subsample used for the determination

of the selection efficiency (detector response matrix for unfolding procedure) and background.

Since the inclusive muon QCD samples do not have sufficient statistics for a reliable estimate of background, they are not included in the analysis and reference subsamples. However, they are used with the data-driven method to estimate the QCD background.

The non-QCD (analysis and reference subsamples) and the QCD samples with number of events and the corresponding integrated luminosities are given in Tables 4.2, 4.3 and 4.10. Since the samples are generated with LO generators, an inclusive k-factor (1.306 for $t\bar{t}$ and 1.13 for W and Z) is applied to scale to NLO cross sections [17]. The number of simulated signal events in the analysis and reference subsamples correspond to 2 fb^{-1} and 20 fb^{-1} integrated luminosities, respectively.

Table 4.2: Analysis subsample.

Process	Dataset	Events	$\sigma \times BR$ (pb)
$t\bar{t}$	/TTJets-madgraph/Fall08_IDEAL_V11_redigi_v10/GEN-SIM-RECO	828 K	414
W+jets ($W \to l\nu$)	/WJets-madgraph/Fall08_IDEAL_V9_v1/GEN-SIM-RECO	10.2 M	45199
Z+jets ($Z \to l^+l^-$)	/ZJets-madgraph/Fall08_IDEAL_V9_reco-v2/GEN-SIM-RECO	1.2 M	4181
single-top tW	/SingleTop_tWChannel/Summer08_IDEAL_V11_redigi_v2/GEN-SIM-RECO	25 K	29
single-top t ch. ($W \to l\nu$)	/SingleTop_tChannel/Summer08_IDEAL_V11_redigi_v3/GEN-SIM-RECO	100 K	42.9

Table 4.3: Reference subsample.

Process	Dataset	Events	$\sigma \times BR$ (pb)
$t\bar{t}$	/TTbar-madgraph/Winter09_IDEAL_V11_FastSim_v1/GENSIM-DIGI-RECO	8.28 M	414
W+jets ($W \to l\nu$)	/Wjets-madgraph/Winter09_IDEAL_V11_FastSim_v1/GEN-SIM-DIGI-RECO	87.0 M	45199
Z+jets ($Z \to l^+l^-$)	/Zjets-madgraph/Winter09_IDEAL_V11_FastSim_v1/GEN-SIM-DIGI-RECO	8.5 M	4181
single-top tW	/SingleTop_tWChannel/Summer08_IDEAL_V11_redigi_v2/GEN-SIM-RECO	135 K	29
single-top t ch. ($W \to l\nu$)	/SingleTop_tChannel/Summer08_IDEAL_V11_redigi_v3/GEN-SIM-RECO	100 K	42.9

Table 4.4: QCD samples.

Process	Dataset	Events	$\sigma \times BR$ (pb)
QCD	/InclusiveMuPt15/Summer08_IDEAL_V9_v1/GEN-SIM-RECO	6.1 M	121000
QCD	/InclusiveMu5Pt50/Summer08_IDEAL_V9_v1/GEN-SIM-RECO	6.8 M	280000

4.1.3 Event Reconstruction

Muon

Muon candidates are reconstructed by extending their trajectories from the muon chambers to the tracker, where the tracks are then reconstructed in the region of interest using a Kalman filter technique [52]. The muon momentum scale as well as trigger and reconstruction efficiencies will be determined in real $Z \to \mu\mu$ events using the so-called "tag and probe method". More details about the muon identification algorithm can be found in [51].

Electron

Electron candidates are reconstructed starting from electromagnetic calorimeter towers, which are later matched to the track seeds in the pixel detector. The Electron trajectories are then reconstructed from the seed to the calorimeters towers using a Gaussian-Sum filter technique [52]. The electron energy scale, trigger and reconstruction efficiencies will be determined in real $Z \rightarrow ee$ events using the "tag and probe method".

Jet and Missing Energy

An iterative cone algorithm [52] with a cone radius of $\Delta R = \sqrt{\Delta\phi^2 + \Delta\eta^2} = 0.5$ is adopted to reconstruct jets using calorimeter towers as input. By default, a response correction (also called the MC-Jet calibration), which is derived by comparison with particle level jets, is applied to the reconstructed jet transverse energies depending on jet E_T and position in the detector. Similarly, the missing transverse energy ($\not\!\!E_T$) in the event is reconstructed using calorimeter towers. $\not\!\!E_T$ is corrected using the corrections applied to the calorimetric energy contained in jets. The momenta of reconstructed muons are also taken into account in the $\not\!\!E_T$ reconstruction.

b-tagging

Jets are identified as originating from a b quark using the "Jet Probability" algorithm [54]. This method is based on the track impact parameter; it entails computing the compatibility of a set of tracks with having come from the primary vertex. If this probability is low, the jet is likely to be a b quark jet.

4.1.4 Event Selection

Almost 100% of the time the top quark decays to W boson and b quark, while the W boson decay has a leptonic branching ratio of 36/81 and a hadronic branching ratio of 45/81 (in the absence of QCD corrections). The final state topology of the $t\bar{t}$ semileptonic muon decay channel consists of four quarks, of which two are heavy, a muon and a neutrino:

$$pp \rightarrow t\bar{t} + X \rightarrow (bW^+)(bW^-) + X \rightarrow bb + qq + \mu\nu_\mu + X,$$

leading to at least four hadronic jets, of which two originate from a b quark, an isolated muon and missing transverse energy in the event.

Skim Selection

The skim selection contains the following online and offline selections:

- Online selection: all events must satisfy the `HLTMu15` trigger condition, which requires the presence of a non-isolated muon with $p_T > 15$ GeV.

The trigger menus have been defined for LHC luminosities of $10^{32}\mathrm{cm}^{-2}\mathrm{s}^{-1}$.

- Offline selection: a reconstructed muon with $p_T > 20$ GeV and at least one jet with uncalibrated $E_T > 30$ GeV are required.

Offline Pre-selection

- At least four jets with pseudorapidity $|\eta| < 2.4$. The jets from the $t\bar{t}$ decay are often accompanied by additional jets because of parton shower and higher order processes. The silicon tracker covers up to $|\eta| = 2.4$, so $|\eta| < 2.4$ cut on jets facilitates the use of b-tagging. The leading jet must have $E_T > 60$ GeV and the next leading jet $E_T > 40$ GeV and the other jets $E_T > 30\,\mathrm{GeV}$.

- At least one muon with $p_T > 20$ GeV. This and $|\eta| < 2.1$ cut, which correspond to the acceptance of muon trigger, largely reduce the QCD background. No isolation requirement is applied at this stage, so that the data-driven QCD estimation based on muon isolation can be performed in the last step of event selection.

- Events are vetoed if there is an electron with $p_T > 20\,\mathrm{GeV}$, $|\eta| < 2.4$, $p_{T\ iso}^{tracker} <$ 2 GeV, $E_{iso}^{calo} < 6$ GeV and the tight electron-ID selection. $p_{T\ iso}^{tracker}$ is the sum of the transverse momenta of all tracks found within a cone of $\Delta R < 0.3$ around the lepton direction excluding the lepton track, and

E_{iso}^{calo} is the total calorimeter deposits (excluding those associated with the lepton) in a cone of $\Delta R < 0.3$ around the lepton direction. Figure 4.2 shows the $p_{T\ iso}^{tracker}$ and E_{iso}^{calo} distributions of the electrons matched to the generated ones using $t\bar{t}$ semileptonic electron channel events.

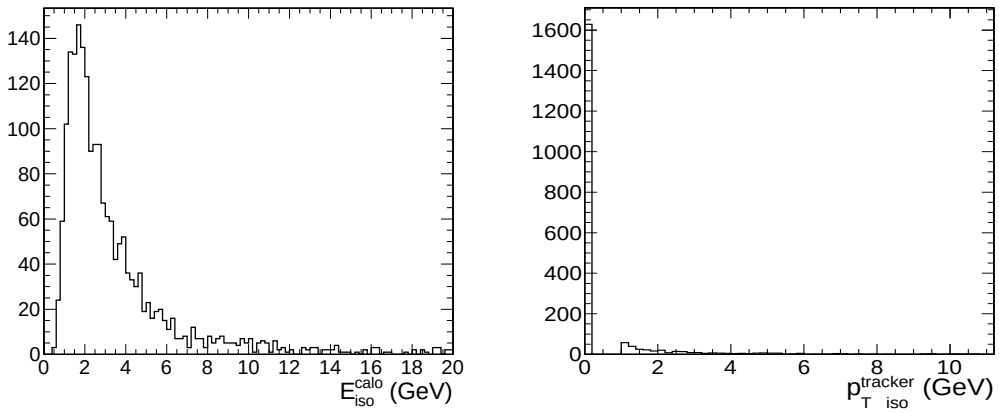


Figure 4.2: E_{iso}^{calo} (left) and $p_{T\ iso}^{tracker}$ (right) distributions of the electrons matched to the generated ones in semileptonic electron channel events. Note that the P_T threshold cut on tracks is 1.0 GeV [53].

At this point in event selection, the signal selection efficiency is 31.4%.

Jet Combination Selection Based on Likelihood Ratio (LR)

For the muon plus jets events passing the above pre-selection cuts, a jet-combination selection is devised to select the correct jet combination for the semileptonic (muon) $t\bar{t}$ decay channel topology.

For each event, all sets of 4-jet combinations in the event meeting the re-

quirements on jet E_T given above are considered. Since the two light jets can not be distinguished, there would be $4!/2 = 12$ combinations in each set and $\frac{n!}{(n-4)!\cdot 2}$ combinations per event, where n is the number of jets satisfying the jet requirements in the event. The correct jet combination is defined as the Monte Carlo best jet combination [55] for a $t\bar{t}$ signal event if a good jet-parton match is found using the criteria

$$\Delta R(\text{each of 3 partons, jet}) < 0.4 \;\;\&\;\; \Delta R(\text{fourth parton, jet}) < 1\,,$$

and the wrong jet combinations are all other jet combinations in the signal and background events.

An optimization study was performed to find the minimum number of jet-combination observables providing good selection efficiency, signal to background ratio and avoiding observables that could potentially bias the measurement of the asymmetry coefficient A_D. The following 8 observables with strong separation of correct and wrong jet combinations form an optimum set:

- Sum of b-tagging discriminator of two b jets
- Transverse momentum of the hadronically decaying t quark divided by the average transverse momentum of the hadronically decaying t quarks over all possible jet combinations.
- Probability obtained from the kinematic fit of the two light jets with W-mass constraint [56, 57].

- Mass of the hadronically decaying t.
- Mass of the hadronically decaying W.
- Mass of the leptonically decaying t estimated with neutrino $P_z = 0$.
- Mass of the hadronically decaying t using the modified light jets parameters from the kinematic fit with W-mass constraint mentioned above.
- Probability obtained from the fit of the neutrino components. That fit minimizes the following χ^2:

  $$\chi^2 = \left(\frac{M(l\nu)-M_W}{\sigma^{lept}_{M(W)}}\right)^2 + \left(\frac{M(bl\nu)-M_t}{\sigma^{lept}_{M(t)}}\right)^2 + \left(\frac{p_T(\nu)-\not{E}_T}{\sigma_{p_T(\nu)}}\right)^2 + \left(\frac{\phi(\nu)-\phi(\not{E}_T)}{\sigma_{\phi(\nu)}}\right)^2 + \left(\frac{P_z(\nu)-P_z}{\sigma_{P_z(\nu)}}\right)^2.$$

  The initial values of p_T and azimuthal angle ϕ of the neutrino are taken from the $\not{E}_T$ measurements. The initial value of the longitudinal neutrino momentum P_z is derived using the W-mass. The resolutions σ are obtained from the MadGraph $t\bar{t}$ Monte Carlo. The resolutions $\sigma_{p_T(\nu)}$ and $\sigma_{\phi(\nu)}$ are found as function of $\not{E}_T$. M_W and M_t are 80.4 GeV and 170.9 GeV, respectively, taken from MadGraph $t\bar{t}$ Monte Carlo.

For observable x_i, the distribution

$$f_i(x_i) = C_i(x_i)/(C_i(x_i) + W_i(x_i)) \tag{4.10}$$

is calculated, where $C_i(x_i)$ and $W_i(x_i)$ are the distributions for the correct and wrong jet combinations, respectively. Each distribution is weighted according

to the number of jet combinations it is made of. $C_i(x_i)$, $W_i(x_i)$ and $f_i(x_i)$ distributions for an example observable (Sum of b-tagging discriminator of two b jets) is show in Figure 4.3, see Appendix for all observables.

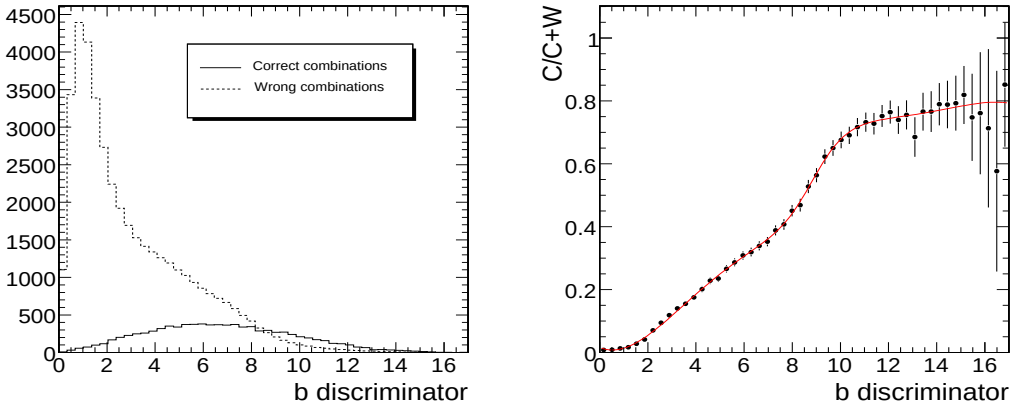


Figure 4.3: Sum of b-tagging discriminator of two b jets

The likelihood ratio $P_i(x_i)$ for the observable x_i is then computed by

$$P_i(x_i) = \frac{f_i(x_i)}{(1 - f_i(x_i))} \,. \tag{4.11}$$

The likelihood ratios of all observables are combined into a total log-likelihood ratio

$$P_C = \sum_i log(P_i(x_i)^{\frac{1}{\sum_j c_{ij}}}) \,, \tag{4.12}$$

where c_{ij} is the correlation factor between i-th and j-th observables.

For each event, the best jet combination is chosen as that with the highest total log-likelihood ratio P_C and denoted by P_C^{max}. From here onwards, only one jet combination, corresponding to the P_C^{max}, per event is considered. In

Figure 4.4, the distribution of P_C^{max} is shown for the correct and wrong jet combinations for the signal events; the correct jet combination is the P_C^{max} combination matching to the MC best jet combination, and the wrong jet combination is the P_C^{max} combination not matching the MC best jet combination as well as the combinations in the signal event without good jet-parton matching. The purity versus P_C^{max} plot, where purity is defined as $S/(S+B)$ with S=number of signal events with correct combination and B=number of signal events with wrong combination, is also shown in Figure 4.4.

The $P_C^{max} > -3.6$ cut is chosen based on an optimization of the selection efficiency and the angular measurement resolution - maximum efficiency with sufficient purity to allow good angular measurements. This cut results in a 52.5% purity, see the right plot in Figure 4.4. The signal events with $P_C^{max} > -3.6$ with the correct or with the wrong jet combination are then considered to make up the "selected" sample of signal events.

Muon Relative Isolation

In order to distinguish muons from W decays from those in b/c hadron decays, an isolation requirement is applied on muon candidates. The muon relative isolation is computed using E_{iso}^{calo} and $p_{T\ iso}^{tracker}$

$$RelIso = \frac{p_T^{\mu}}{p_T^{\mu} + E_{iso}^{calo} + p_{T\ iso}^{tracker}} \, . \tag{4.13}$$

The P_C^{max} distributions before and after the $RelIso > 0.9$ cut are shown in

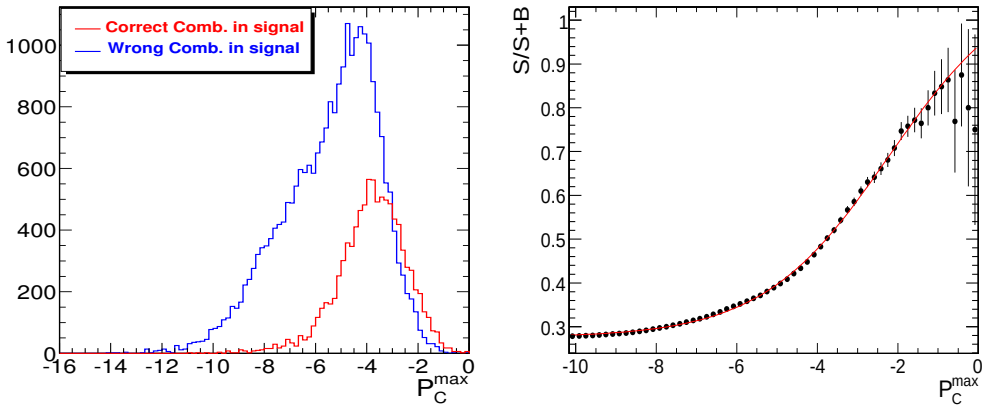


Figure 4.4: Left: Distributions from the reference subsample of the highest total log-LR value (P_C^{max}) of the correct and wrong jet combinations in the signal events. Normalized to 2 fb^{-1}. Right: Purity vs. P_C^{max}.

Figure 4.5. After this final cut, the contributions from the correct and wrong combinations in the signal events are 53% and 47%, respectively. The cut value of 0.9 is motivated by the data-driven QCD background estimation discussed in Section 4.1.5.

4.1.5 Results

Data-driven QCD Background Estimation

It is difficult to estimate the QCD background from the available Monte Carlo event samples. The QCD processes have large cross sections and small selection efficiencies, making it difficult to generate sufficient QCD events for a robust estimate. Furthermore, there will be systematic uncertainties on the estimated

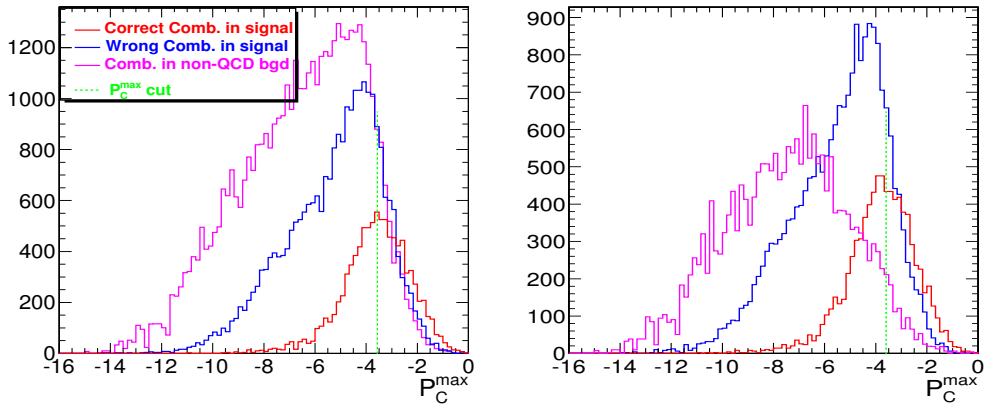


Figure 4.5: The highest total log-LR value (P_C^{max}) distributions from the reference subsample before (left) and after (right) $RelIso > 0.9$ cut. Both are normalized to 2 fb^{-1}.

QCD background, which have to be determined from data. Therefore, a data-driven QCD background determination is essential; in this analysis, the method of Muon Relative Isolation is adopted.

After all the selection cuts but RelIso, the RelIso distribution for the reference subsample (without QCD events) and the RelIso distribution for the analysis subsample plus QCD events are produced, Figure 4.6. The reference RelIso distribution, Figure 4.6 left, is fitted with an appropriate function $F(x)$, which represents the shape of non-QCD contribution in RelIso distribution. Then, the analysis plus QCD RelIso distribution, Figure 4.6 right, representing the "data" distribution with yet unknown QCD contribution, is fitted with the sum of the non-QCD function $F(x)$ with free normalization and an exponential

representing the QCD contribution:

$$P_0\, F(x) + P_1\, \exp(P_2\, x)\,, \tag{4.14}$$

where $P's$ are the fit parameters. The integral of the exponential component from 0.9 to 1.0 represents the QCD background contribution to the signal region, which is estimated along with its error as 271 ± 15 events, in agreement with 5 events actually passing the selection in the QCD sample, corresponding to 240 ± 110 QCD events in $2\,\mathrm{fb}^{-1}$. The $RelIso > 0.9$ cut results in both good signal selection and low residual QCD background.

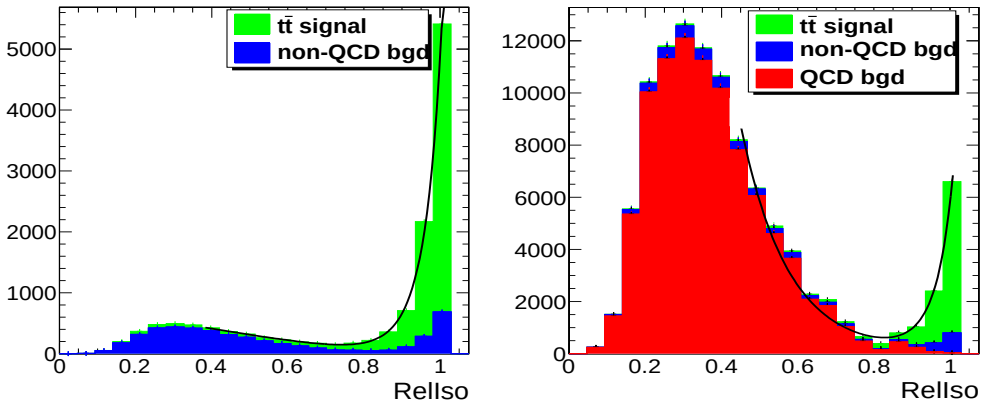


Figure 4.6: Muon relative isolation distributions for the reference subsample (without QCD events) (left) and for the analysis subsample plus QCD events (right). The fit curves are superimposed.

Signal and Background Yields

Table 4.5 summarizes the selection results obtained using the analysis subsample plus the QCD samples. Note that all event numbers are scaled to 2fb^{-1}. The main contribution to the total background (58%) is from the $t\bar{t}$ processes different from those treated as signal. Since the QCD background is estimated with the RelIso method, there are no QCD angular distributions. Therefore, both the analysis and reference non-QCD background distributions are scaled to account for the additional 271 QCD background events. The signal to background ratio is found to be 6.3 in the analysis subsample with an overall efficiency of 6.9%.

Figure 4.8 shows the invariant mass of the reconstructed top quarks plus background and the background only after all the selection. Figure 4.9 shows the reconstructed opening angle distributions after the selection. The $cos(\phi_{l\text{-}b})$ and $cos(\phi_{l\text{-}q})$ resolutions are determined by taking the difference between cosine of the generated and reconstructed angles using the $t\bar{t}$ signal events from the analysis subsample with good jet-parton matching, i.e. satisfying the criteria mentioned in Section 4.1.4. The resolutions are found to be 0.14 and 0.17 for $cos(\phi_{l\text{-}b})$ and $cos(\phi_{l\text{-}q})$, respectively, see Figure 4.7; a bin size approximately two times the resolution results in 7 and 6 bins for these distributions.

Note that in these figures the signal plus background is obtained from the analysis subsample and corrected for the QCD background contribution as mentioned above, and the background is obtained from the reference subsample.

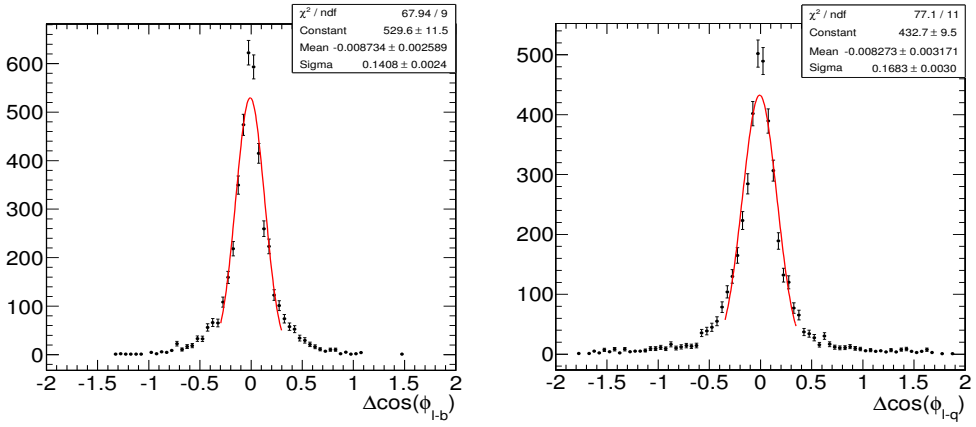


Figure 4.7: Resolution of $cos(\phi_{l\text{-}b})$ (left) and $cos(\phi_{l\text{-}q})$ (right) .

Unfolding Angular Distributions

The measured opening angle distributions are affected by detector finite resolution, non-linear response and limited acceptance, as well as event selection. These effects cause smearing and bin-to-bin migration that need to be unfolded. Here, a method of unfolding based on the Singular Value Decomposition (SVD) of the response matrix [58] is used. Mathematically, the relation between the distribution $T(x)$ of the true variable x, to be determined in an experiment, and the measured distribution $M(y)$ of the measured quantity y is given by the integral equation

$$M(y) = \int R(y,x)T(x)\,dx, \tag{4.15}$$

where $R(y,x)$ is the response function representing the effect of the detector and selection. Since the analysis deals with histograms, Equation 4.15 must be

Table 4.5: Selection flow for the analysis subsample and the QCD samples.

	Signal	Other $t\bar{t}$	W+Jets	Z+Jets	single-top tW	single-top t ch. (lep.)	QCD
# Events in 2 fb^{-1}	122666	705200	$9.04 \cdot 10^7$	$8.36 \cdot 10^6$	58000	85800	$8.02 \cdot 10^8$
Online Selection	80879	70526	72125	15058	8450	14455	$2.96 \cdot 10^7$
Offline Pre-Selection	39502	28305	18507	3290	2023	855	369580
$P_C^{max} > -3.6$	9721	4692	89	7	185	63	90180
N_μ (RelIso > 0.9) $= 1$	8352	817	62	7	120	46	271

represented by the matrix equation

$$M = RT, \tag{4.16}$$

where the i-th elements of vector M and vector T are the i-th bin content of M (measured distribution) and T (true distribution), respectively, and R is the response matrix, element R_{ij} of which gives the fraction of events from T_j ending up measured in bin M_i. The response matrix for $\cos(\phi_{l\text{-}b})$ and $\cos(\phi_{l\text{-}q})$ are presented in Figure 4.10. They are obtained by tracking the generated and reconstructed values for each event after all selection cuts.

The response matrix R must be inverted to extract T

$$T = R^{-1}M. \tag{4.17}$$

In principle, the result is satisfactory only for a matrix with dominating di-

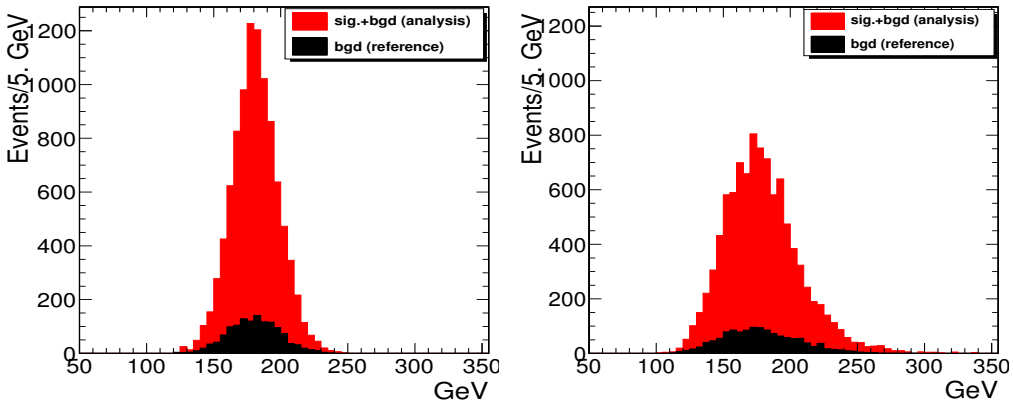


Figure 4.8: Reconstructed top quark invariant mass spectra: t decaying into three jets (left), t decaying into muon, neutrino and b jet (right).

agonal; the result looks less satisfactory if the matrix describes large migration to neighboring bins. Also statistical fluctuations in the measured distribution introduce spurious, non-physical oscillations in the solution for the true distribution. The SVD method used here can remove rapidly oscillatory solutions and is well suited for the measured distributions in this analysis.

Determination of Regularization Parameter

In the SVD method a regularization term is added in the unfolding process to suppress the rapidly oscillatory solutions. The regularization term depends on one parameter τ; a small value of τ will bias the unfolding result towards the MC truth input. A large value will give a result that is dominated by statistical fluctuations. (With the maximum τ value, the number of bins, there is no

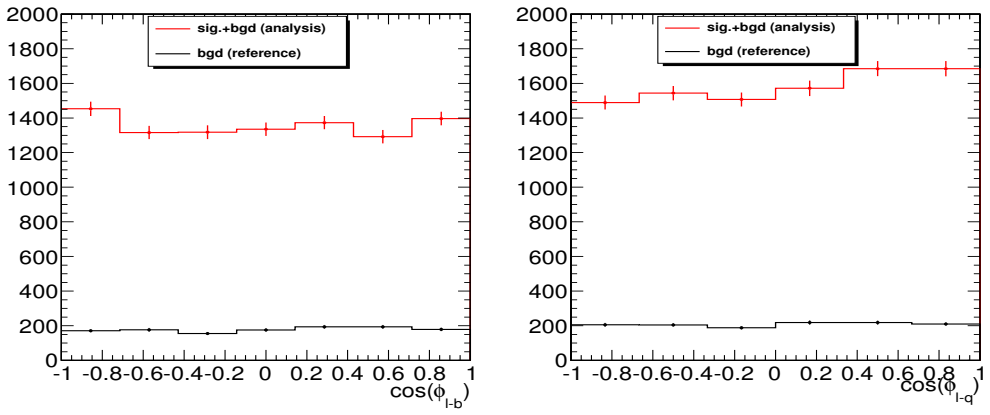


Figure 4.9: Reconstructed opening angle distributions: l-b angle (left) and l-q angle (right).

regularization in solution.)

The optimum τ values for l-b and l-q are determined separately by estimating the unfolding bias in a set of toy tests. The quantity used to gauge the agreement between the unfolded and original true distributions is the sum of χ^2 over bins

$$S = \sum_i \left(\frac{U_i^\tau - T_i}{\sigma(U_i^\tau)}\right)^2, \tag{4.18}$$

where U^τ is the unfolded measured distribution, T is the original true distribution and $\sigma(U^\tau)$ is the error of the unfolded measured distribution. The minimum S obtained at a particular τ value indicates that the deviation of U^τ from the true distribution T is minimized and thence that τ value is the optimum one.

For the toy tests $22\,\mathrm{fb}^{-1}$ fast simulated $t\bar{t}$ signal events are used for constructing the $\cos(\phi_{l\text{-}b})$ and $\cos(\phi_{l\text{-}q})$ response matrix and the toy measured dis-

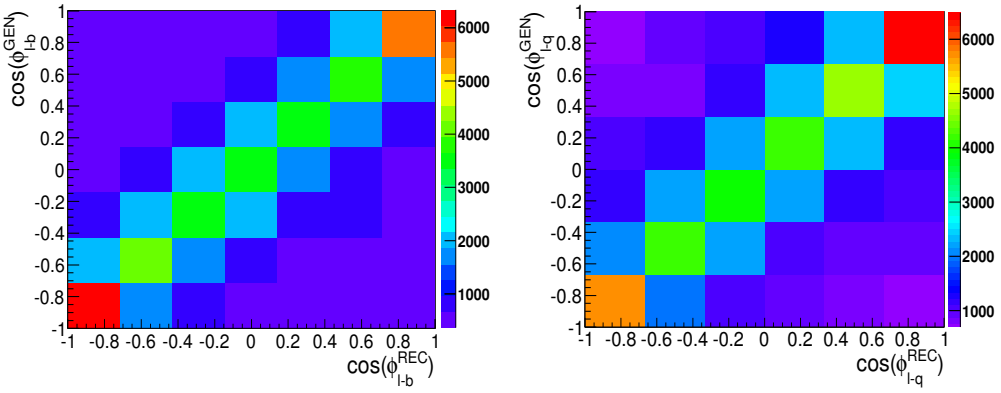


Figure 4.10: Response matrices from the reference subsample: l-b angle (left) and l-q angle (right).

tributions to be unfolded. The following steps are done for each τ value:

1 The response matrix is obtained from a sample of $20\,\mathrm{fb}^{-1}$,

2 The measured distribution to be unfolded is obtained from a sample of $2\,\mathrm{fb}^{-1}$,

3 1000 toy measured distributions, each of which $2\,\mathrm{fb}^{-1}$, are randomly generated from the shape of the distribution obtained in Step 2 (using `GetRandom()` method of Histogram class of `ROOT` [59]),

4 Perform unfolding and calculate S,

5 Repeat Steps 1-4 100 times for statistically different $20\,\mathrm{fb}^{-1}$ response matrices (randomly generated from the shape of the original).

From the above steps, it is determined that $\tau = 3$ is the optimum value for the regularization parameter. Using this τ value, Steps 1-4 are repeated with the measured distribution from the analysis subsample to obtain the pull distributions. The pull value for bin i is calculated as

$$pull_i = \frac{U_i - T_i}{\sigma(U_i)}. \tag{4.19}$$

Figure 4.11 and 4.12 show the resulting pull distributions for each bin of $\cos(\phi_{l\text{-}b})$ and $\cos(\phi_{l\text{-}q})$ distributions. The mean and sigma values obtained from a Gaussian fit to the pull distributions are given in Tables 4.6. These results are used to determine the systematic uncertainty coming from the unfolding procedure, see Section 4.1.6.

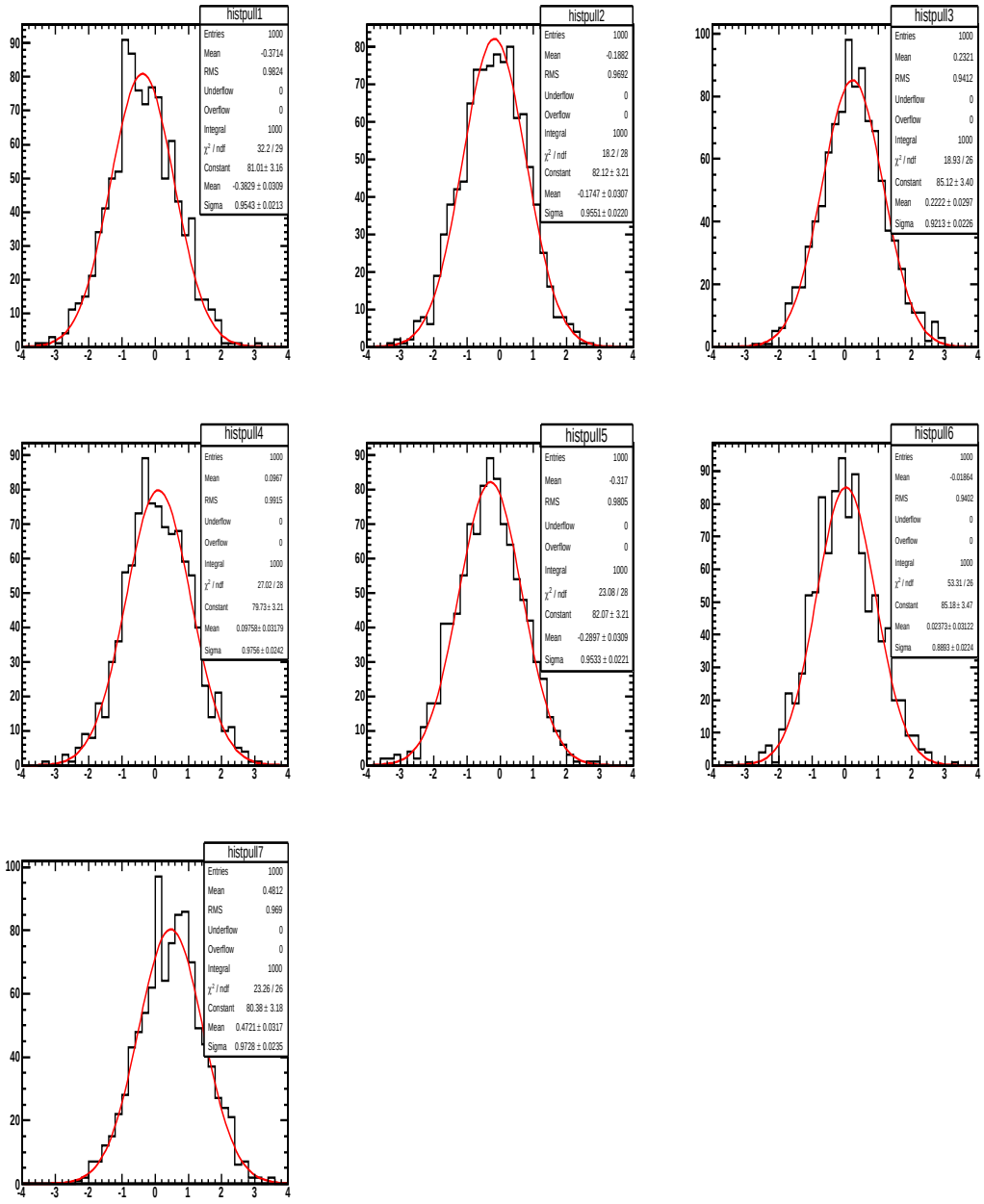


Figure 4.11: Pull distributions from unfolding the $\cos(\phi_{l\text{-}b})$ distribution with regularization parameter $\tau = 3$.

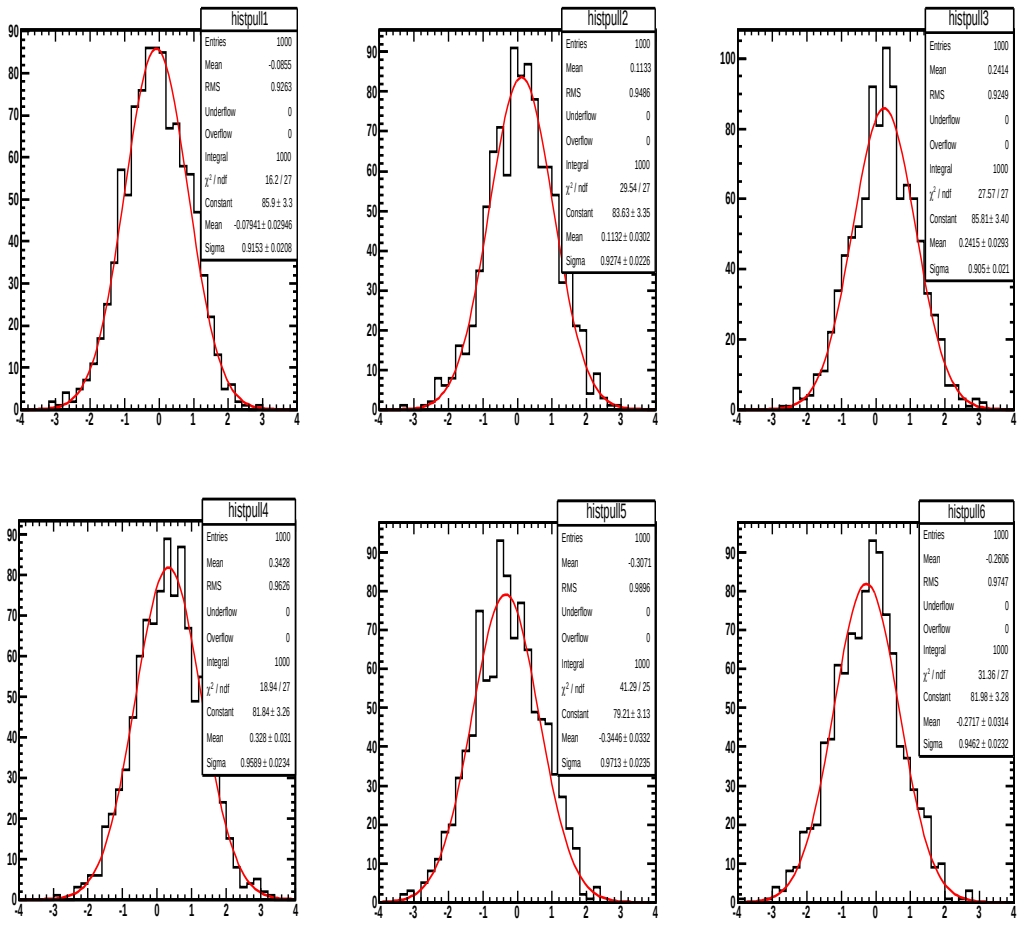


Figure 4.12: Pull distributions from unfolding the $\cos(\phi_{l\text{-}q})$ distribution with regularization parameter $\tau = 3$.

Table 4.6: Results of the Gaussian fits for the $\cos(\phi_{l\text{-}b})$ (left) and $\cos(\phi_{l\text{-}q})$ (right) pull distributions with regularization parameter $\tau = 3$.

bin	mean	σ
1	-0.383 ± 0.031	0.954 ± 0.021
2	-0.175 ± 0.031	0.955 ± 0.022
3	0.222 ± 0.030	0.921 ± 0.022
4	0.097 ± 0.032	0.976 ± 0.024
5	-0.289 ± 0.031	0.953 ± 0.022
6	0.024 ± 0.031	0.889 ± 0.022
7	0.472 ± 0.032	0.973 ± 0.024

bin	mean	σ
1	-0.08 ± 0.030	0.915 ± 0.021
2	0.1132 ± 0.030	0.927 ± 0.022
3	0.242 ± 0.030	0.905 ± 0.021
4	0.328 ± 0.031	0.959 ± 0.023
5	-0.345 ± 0.033	0.971 ± 0.024
6	-0.272 ± 0.031	0.946 ± 0.023

Estimation of the Spin Asymmetry Coefficient

The final measurement of the opening angle distribution is obtained by subtracting, bin-by-bin, the background obtained from the reference subsample from the total of signal plus background (Figure 4.9) obtained from the analysis subsample. The resulting distributions are unfolded as described above to obtain the true distributions shown in Figure 4.13.

The asymmetry coefficient A_D is then obtained as the parameter of a global fit of both angular distributions in Figure 4.13 using Formulae 4.2 and 4.7:

$$A_D = 0.214 \pm 0.034, \tag{4.20}$$

which agrees within the statistical errors with that obtained from the fit of ALPGEN generated opening angle distributions, see Figure 4.1.

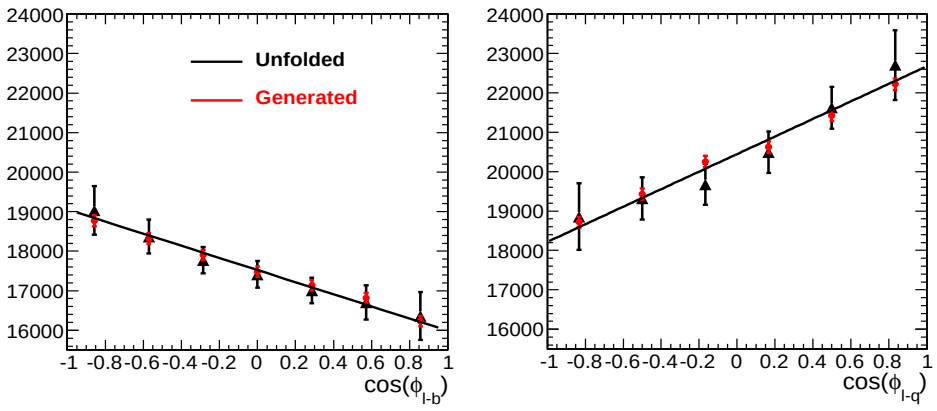


Figure 4.13: Background subtracted and unfolded opening angle distributions (black points): l- angle (left) and l-q angle (right). The black lines represent a global fit of both angular distributions. The number of events corresponds to an integrated luminosity of $2\,\mathrm{fb}^{-1}$.

Note that the above A_D measurement is obtained from the $t\bar{t}$ event samples built with the SM spin asymmetry. The event selection in this analysis emphasized selection criteria with minimum or no impact on the angles to be measured so not to bias the A_D measurement. Nevertheless, in order to show that the measurement of A_D is not biased and is independent of the assumed spin asymmetry, two other spin symmetry scenarios are considered: "no spin asymmetry" and "spin asymmetry with opposite slope".

For each scenario, the reference subsample is modified to produce the desired

effect: for no spin asymmetry the MadGraph $t\bar{t}$ signal events are left with no weighting for spin correlation; for spin asymmetry with opposite slope the events are weighted according to the alpgen opening angle distributions shown in Figure 4.1 but with the opposite sign slopes.

Using the alpgen generated angular distributions for both *l*-*b* and *l*-*q* for each scenario and the new response matrix derived from the corresponding reference subsample, the unfolding is applied to the background subtracted reconstructed angular distributions from the analysis subsample, Figure 4.9, to find the true distributions and the new A_D value. The results are $A_D = 0.2156 \pm 0.0338$ for no spin asymmetry, and $A_D = 0.2160 \pm 0.0338$ for spin asymmetry with opposite slope, in agreement with the standard value $A_D = 0.214 \pm 0.034$.

Next, the amount of spin asymmetry in the analysis subsample is varied to check the measurement sensitivity to such variations. The MadGraph $t\bar{t}$ signal events in the analysis subsample are weighted to account for spin asymmetry but with a slope that is $\pm 25\%$ of the standard value. The reference subsample, i.e. the response matrices and the generated *l*-*b* and *l*-*q* angular distributions, are kept unchanged with the SM spin asymmetry. The A_D values found are 0.167 ± 0.034 and 0.264 ± 0.034 in agreement with the expected values $0.214 \times 0.75 = 1.61$ and $0.214 \times 1.25 = 0.268$ within the statistical error.

It can be concluded that the analysis method and the event selection do not introduce a bias in the measurement of A_D.

Finally, given that MC event samples used for the analysis subsample are processed with the full detector simulation and the events for the reference subsample are processed with the fast detector simulation, effects due to possible differences between the two subsamples should be investigated. The selection efficiency estimated using the reference subsample is found to be less than that using the analysis subsample by about 12%. However, the shapes of selection efficiency as a function of l-b and l-q angles are very similar, as shown in Figure 4.14, thence no consequence to the A_D measurement.

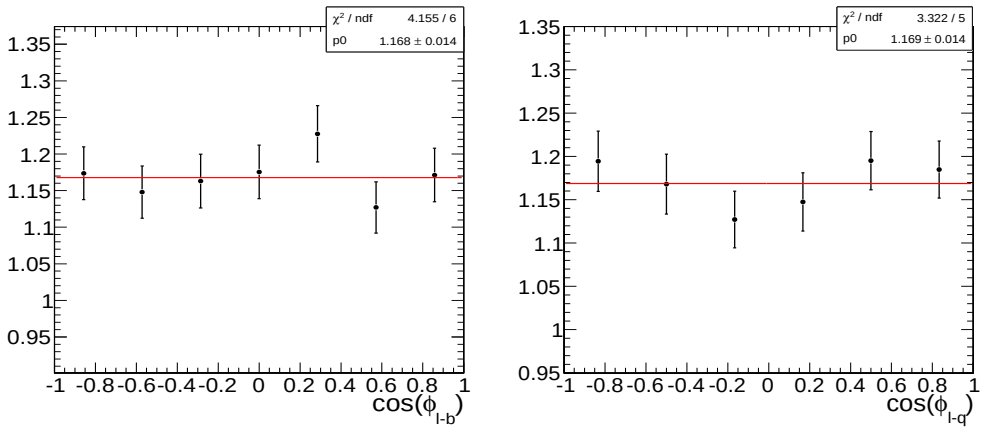


Figure 4.14: Ratio of the analysis (full simulation) to the reference (fast simulation) selection efficiency for the opening angle distributions: l-b angle (left) and l-q angle (right).

Furthermore, the A_D measurement is repeated using the fast-simulation samples only, that is both the analysis and reference subsamples are made from events processed with the fast detector simulation. Then, $A_D = 0.199 \pm 0.036$,

which agrees within the statistical errors with both the full-simulation result above and the ALPGEN generated one, see Figure 4.15.

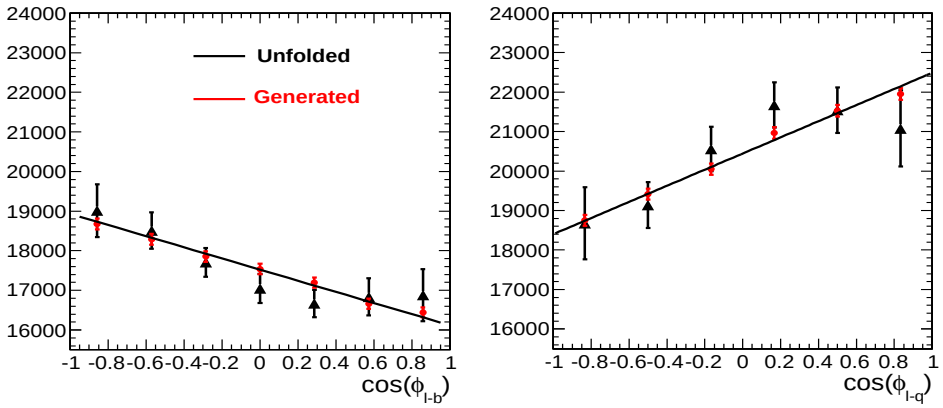


Figure 4.15: Background subtracted and unfolded opening angle distributions (black): *l*-*b* angle (left) and *l*-*q* angle (right). The black lines represent a global fit of both angular distributions, which gives $A_D = 0.199 \pm 0.036$. The number of events corresponds to an integrated luminosity of $2\,\mathrm{fb}^{-1}$.

4.1.6 Systematic Uncertainties

Systematic Uncertainties at Generation Level

- **PDF**: The impact of parton distribution function is estimated by taking the difference between the measurements obtained with the default PDF CTEQ5L and two others, CTEQ6L, MRST2002. The variation in A_D is found to be +3.2% for CTEQ6L and -1.8% for MRST2002.

- **Top mass and $t\bar{t}$ cross section**: As shown in [60], the top mass and $\sigma_{t\bar{t}}$

uncertainties lead to negligible variation in $t\bar{t}$ spin correlation.

- **W+jets and Z+jets cross sections**: The cross sections for W+jets and Z+jets background processes are varied by +100% and −50% [61], (large variation to account for Wbb background not considered in this study), this results in −1.0% and +0.5% variation in A_D, respectively.

- **Jet multiplicity**: Uncertainties in initial state and final state radiations (ISR and FSR), heavy quark fragmentation, underlying events and pile up rate could result in an underestimation of the number of non-$t\bar{t}$ jets (not matched to any partons coming from signal $t\bar{t}$ events with good-jet parton match). The rate of such additional non-$t\bar{t}$ jets with $p_T > 30\,\mathrm{GeV/c}$ and $|\eta| < 2.5|$, which could potentially be involved in the selection flow, is estimated to be 7.8% [60]. To account for this effect, a conservative 10% additional jets per event are generated while processing the analysis subsample. This results in -4.0% variation in A_D. Technique used: Before the selection, a jet with randomly generated p_T, η and b-discriminator parameters is added to the event jet collection in 10% of events. The jet p_T, η and b-discriminator distributions are prepared for this sort of jet from the MadGraph $t\bar{t}$ event samples. The event energy is conserved and the extra jet introduced is taken into account in the calculation of missing energy, as well as merged with an existing jet if they overlap.

- **Sensitivity to $t\bar{t}$ modeling**: The PYTHIA MC $t\bar{t}$ samples are used to test the sensitivity of $t\bar{t}$ spin correlation measurement to the modeling of $t\bar{t}$ used in simulation. PYTHIA does not simulate $t\bar{t}$ spin correlation, therefore events are properly weighted as was done with the MADGRAPH samples, see Section 4.1.2. The result obtained from the PYTHIA event sample $A_D = 0.18 \pm 0.03$ is consistent within the statistical errors with the MADGRAPH's $A_D = 0.21 \pm 0.03$, leading to negligible systematic uncertainty as the difference in A_D values are simply due to statistically independent samples.

Systematic Uncertainties at Reconstruction Level

- **b-tagging**: The impact of the b-tagging efficiency is studied by changing the b identification discriminator in the corresponding jet-combination observable (sum of b-tagging discriminators of the two b jets) such that b-tagging efficiency varies by +6%and-6% [62]. The corresponding variation in A_D is -4.0% and +7.0%, respectively.

- **JES**: The uncertainty due to the jet energy scale uncertainty is evaluated by varying the jet energy by $\pm 2\%$, which is derived from [63]. A_D is varied by +6.3% and +13.0%, respectively. In semileptonic channel, the $t\bar{t}$ system has to be reconstructed using 4 jets and $\not{E}_T$, which are all subject to change in JES. Since the opening angles between two chosen

decay products are actually measured in the t and $\bar{t}$ rest frames (Lorentz-boosted to t or $\bar{t}$ rest frame), the JES variation goes into these calculations and consequently changes the flight direction of decay products. So the angular measurements are quite sensitive to JES. Similar spin correlation measurement was performed with singletop t-channel, see section 4.2.5. In this channel, there is only one top to be reconstructed, one jet (b-jet) and $\not\!\!E_T$ are subject to change in JES. JES systematic errors turn out to be -3% and $+7\%$. So one can argue: the more jets are involved in angular measurements, the more variation in spin correlation. Also, it is more probable that we pick up the wrong jets when JES is varied.

- **MET**: The Missing Transverse Energy $\not\!\!E_T$ is varied by $\pm 10\%$ as used in [61]. The variation in A_D turns out to be -1.4% and +9.0%, respectively. As discussed above in JES, variation in $\not\!\!E_T$ as much as 10% could change the angular measurements because of Lorentz-boosting of decay products to t and $\bar{t}$ rest frames.

Other Systematic Uncertainties

- **Uncertainty in QCD Background Estimation**: The uncertainty in the number of QCD events from the data-driven method is estimated using the statistical error of the fit performed with the $RelIso$ distribution, Figure 4.6 (right), plus varying the shape of the non-QCD distribution,

Figure 4.6 (left) by changing the W+jets and Z+jets contributions by $+100\%$ and -50% and varying the fit range in $RelIso$ by approximately one bin size (± 0.05). These add up to a $\pm 25\%$ error in QCD background resulting in $\pm 2.0\%$ variation in A_D.

- **Uncertainty from Unfolding Procedure** The mean values given in Table 4.6 are used to estimate the systematic uncertainty coming from the unfolding procedure. The $\cos(\phi_{l\text{-}b})$ and $\cos(\phi_{l\text{-}q})$ distributions are corrected, bin-by-bin, according to the shift in the mean from 0. Then, the modified distributions are used to extract A_D using the global fit as before. The variation in A_D is found to be $+5.0\%$.

Table 4.7 summarizes the systematic uncertainty results.

4.1.7 Conclusions for $t\bar{t}$ Production

The spin asymmetry coefficient of top quarks in $t\bar{t}$ production in proton-proton collisions at 10 TeV is measured using distributions of the opening angles between top and anti-top decay products. Based on a total integrated luminosity of two inverse femtobarns, the result is

$$A_D = 0.214 \pm 0.034\,(\text{stat.})^{+0.040}_{-0.024}(\text{sys.}). \tag{4.21}$$

Including the systematic uncertainties, the measurement has a total relative uncertainty of 25%.

Table 4.7: Results obtained for each source of systematic uncertainty considered and the total systematic uncertainty. The total gives the sum of the systematic errors in quadrature.

Source of systematic uncertainty	Uncertainty (%)
PDF (CTEQ6L and MRST2002)	$+3.2, -1.8$
Top Mass ($\pm 5\%$)	negligible
$t\bar{t}$ cross section ($\pm 10\%$)	negligible
W+jets and Z+jets cross sections ($+100\% - 50\%$)	$-1.0, +0.5$
Jet multiplicity ($+10\%$)	-10.0
Sensitivity to $t\bar{t}$ modeling	negligible
b-tagging efficiency ($\pm 6\%$)	$-3.0, +7.0$
JES ($\pm 2\%$)	$+6.3, +13.0$
MET ($\pm 10\%$)	$-1.4, +9.0$
QCD background estimation ($\pm 25\%$)	± 2.0
Unfolding Procedure	$+5.0$
Total	$+18.6, -11.$

4.2 Spin Polarization in t-channel Single Top Quark Production

4.2.1 Introduction

The study of top quark coupling to other particles is important in determining if the Standard Model mechanism for electroweak symmetry-breaking is the correct one, or if some type of new physics is responsible. Angular correlations among the decay products of polarized top quark provide a useful handle on these couplings. Although possessing a larger production cross section compared to single top, top quark pairs at the LHC do not dominantly populate a single spin configuration in any basis, because the initial state is primarily gg [40]. Furthermore, the Wg fusion in t-channel single top quark production, which we focus on in this study, is an electroweak process with the produced top quark coupled directly to a W boson. Because of the parity-violating $V - A$ structure of the coupling to the W boson, the decay products of a polarized top quark have a rich structure of angular correlations given by Equation 4.1. In particular the angular correlation between the spin orientation of the top quark and the charged lepton from its decay is an optimum observable since the lepton is maximally correlated, see Table 4.1. The degree of such correlation also depends on the choice of the top quark spin quantization axis. Since single

top quarks are 100% polarized in the direction of the d-type quark, the preferred emission direction of the charged lepton from the decaying top quark, as viewed in any frame, is the same as the direction of the d-type quark in that frame. But, it is not always possible to know the direction of the d-type quark. The best we can do is to choose a spin axis that maximizes the likelihood that we have picked the correct direction. The spectator and beamline bases, discussed below, are good choices in this sense. In this situation, we have a mixed sample containing both spin-up and spin-down top quarks, and the angular distribution in Equation 4.1 must be replaced by

$$\frac{1}{N}\frac{dN}{dcos\phi_f} = \frac{1}{2}\left(1 + A\,\kappa_f\,cos\phi_f\right), \tag{4.22}$$

where ϕ is the angle between the spin axis and momentum of f decay particle, which is a muon in this study, in t or $\bar{t}$ rest frame. The quantity $A = (N_\uparrow - N_\downarrow)/(N_\uparrow + N_\downarrow)$ is the spin asymmetry, where $N_{\uparrow/\downarrow}$ are the number of spin-up/down top quarks and $\kappa_f = 1$ is the muon spin analyzer power.

Spin Quantization Axis

Spectator Basis: The spectator basis [64] is the direction of the scattered light quark (the so-called spectator quark) in t ($\bar{t}$) rest frame in the t-channel single top quark production; it provides a good spin quantization basis for t quark, because in about 80% of the time, the spectator quark is a d-type quark in t production. For $\bar{t}$ quark, the situation is different in that there is only a d-

type quark in the final state about 31% of the time. But since the spectator quark is only slightly deflected by momentum transfer via the W boson in the Wg fusion process and the incoming d-type quark is nearly aligned with the spectator quark, using the spectator quark direction does not significantly degrade the degree of spin polarization. Therefore, the spectator basis provides a good spin quantization axis for both t and $\bar{t}$ quarks.

Beamline Basis: Since the d-type quark comes from one of the two beams, it is worthwhile to consider the beamline basis in addition to the spectator basis. The beamline basis is defined by decomposing the t ($\bar{t}$) spin along the direction of one of the proton beams in t ($\bar{t}$) rest frame [40]. There are two beamline basis coming from the $+z$ and $-z$ beam directions; we need to choose the beam that supplied the spectator quark, thence, the direction of the beamline basis of t ($\bar{t}$) must be chosen in such a way that it has the same sign as the spectator quark pseudorapidity. That is, if the pseudorapidity of the spectator jet is positive, the left-moving beam must be chosen; and if negative, the right-moving beam must be chosen. This assignment of the beamline can be improved by selecting events in which the spectator jet is restricted to the forward region: $|\eta| > 2.5$ is applied in this study.

Simulation Results

The MadGraph event generator for hard multiparton processes in hadronic collisions at LO is used to estimate the spin correlation in the single t and $\bar{t}$ decay products. The generated events are based on pp collisions at $\sqrt{s} = 10\,\text{TeV}$ and using the CTEQ6L PDF.

Two angular distributions of lepton (muon) for t and $\bar{t}$ are considered: the angle between the muon and the spectator quark ($\phi_{l\text{-}s}$), and the angle between the muon and the beamline axis ($\phi_{l\text{-}z}$). The generated angular distributions for t and $\bar{t}$ in the spectator and beamline bases are shown in Figures 4.16 and 4.17. Fitting these distributions with function $P_1\,(1 + P_2\,cos\phi)$ for t and function $P_1\,(1 - P_2\,cos\phi)$ for $\bar{t}$, and using parameter P_2 and $\kappa_f = 1$, the asymmetry coefficients in the spectator basis for t and $\bar{t}$ are obtained as

$$A_s^t = 0.927 \pm 0.009 \text{ and } A_s^{\bar{t}} = -0.889 \pm 0.012\,. \tag{4.23}$$

The asymmetry coefficients in the beamline basis, where $|\eta_{spec.jet}| > 2.5$, for t and $\bar{t}$ are obtained as

$$A_z^t = 0.884 \pm 0.012 \text{ and } A_z^{\bar{t}} = -0.915 \pm 0.017\,. \tag{4.24}$$

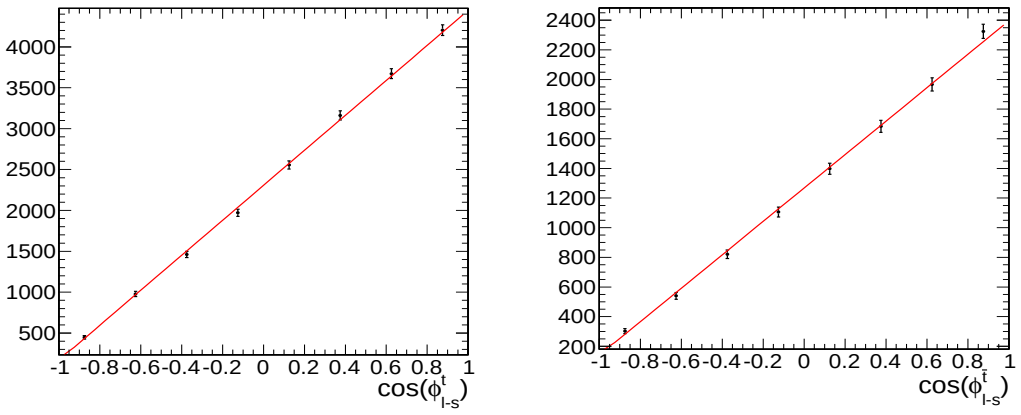


Figure 4.16: MadGraph generated angular distributions for the spectator basis. The number of events corresponds to an integrated luminosity of 2 fb^{-1}. Left: $cos(\phi_{l\text{-}s})$ in the t rest frame. Right: $cos(\phi_{l\text{-}s})$ in the $\bar{t}$ rest frame.

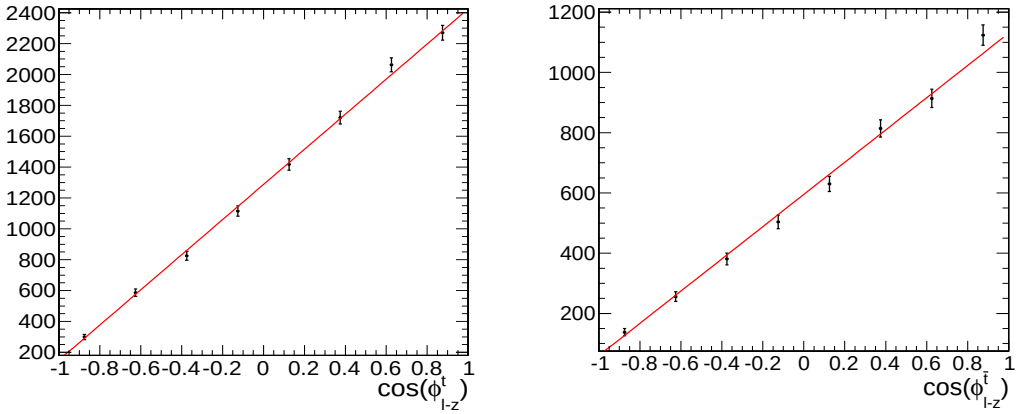


Figure 4.17: MadGraph generated angular distributions for the beamline basis and $|\eta_{spec.jet}| > 2.5$. The number of events corresponds to an integrated luminosity of 2 fb^{-1} before the η cut. Left: $cos(\phi_{l\text{-}z})$ in the t rest frame. Right: $cos(\phi_{l\text{-}z})$ in the $\bar{t}$ rest frame.

4.2.2 Software and Monte Carlo Event Samples

Event generation, detector simulation and physics reconstruction have been carried out using the CMSSW. Specifically, the `CMSSW_2_2_X` release along with the dedicated software package (PAT) are used. The alignment and calibration are assumed to be perfect (ideal scenario) in the detector simulation.

At 10 TeV, the estimated cross section for single t-channel production at NLO is 130 pb [21]; for an integrated luminosity of $2\,\mathrm{fb}^{-1}$ this gives rise to 28888 events in the leptonic final state, where in the leptonic branch only muon (1/9 branching fraction) is considered. This represents the "signal sample" in this analysis.

The background processes considered are the following:

- $t\bar{t}$ inclusive,
- W+jets (leptonic: $W \to l\nu$),
- VQQ ($V = W, Z$; $W \to l\nu, Z \to l^+l^-$; $Q = b, c$),
- Single top tW-channel,
- QCD: `InclusiveMuPt15` ($\hat{P}_T > 20$ GeV, $P_T^{\mu} > 15$ GeV)

The MadGraph MC event generator is used to generate the single top t-channel, single top tW-channel, $t\bar{t}$, W+jets and Z+jets event samples. The simulation of QCD processes is performed with the PYTHIA MC.

In order to have two statistically independent samples, the MC event samples are separated into two subsamples: one is regarded as the "analysis" subsample used for the measurement of spin asymmetry coefficient; the other is regarded as the "reference" subsample used for the determination of the selection efficiency (detector response matrix for unfolding procedure) and background.

Since the inclusive muon QCD sample does not have sufficient statistics for a reliable estimate of background, they are not included in the analysis and reference subsamples. However, they are used with the data-driven method to estimate the QCD background.

The non-QCD (analysis and reference subsamples) and the QCD samples with the number of events and the corresponding integrated luminosities are given in Tables 4.8, 4.9 and 4.10. The number of simulated signal events in the analysis and reference subsamples correspond to $2\,\mathrm{fb}^{-1}$ and $20\,\mathrm{fb}^{-1}$ integrated luminosities, respectively.

Table 4.8: Analysis subsample.

Process	Dataset	Events	$\sigma \times BR\,(\mathrm{pb})$
single-top t-ch. (lep.)	/SingleTop_tChannel/Summer08_IDEAL_V11_redigi_v3/GEN-SIM-RECO	85.8 K	42.9
$t\bar{t}$	/TTJets-madgraph/Fall08_IDEAL_V11_redigi_v10/GEN-SIM-RECO	473.25 K	414
W+jets (lep.)	/Wjets-madgraph/Winter09_IDEAL_V11_FastSim_v1/GEN-SIM-DIGI-RECO	35.15 M	45199
VQQ (lep.)	/VQQ-madgraph/Winter09_IDEAL_V12_FastSim_v1/GEN-SIM-DIGI-RECO	1.55 M	290
single-top tW-channel	/SingleTop_tWChannel/Summer08_IDEAL_V11_redigi_v3/GEN-SIM-RECO	65.56 K	29

Table 4.9: Reference subsample.

Process	Dataset	Events	$\sigma \times BR$ (pb)
single-top t-ch. (lep.)	/SingleTop_tChannel/Winter09_IDEAL_V12_FastSim_v2/GEN-SIM-DIGI-RECO	858 K	42.9
$t\bar{t}$	/TTJets-madgraph/Fall08_IDEAL_V11_redigi_v10/GEN-SIM-RECO	474.12 K	414
W+jets (lep.)	/Wjets-madgraph/Winter09_IDEAL_V11_FastSim_v1/GEN-SIM-DIGI-RECO	35.47 M	45199
VQQ (lep.)	/VQQ-madgraph/Winter09_IDEAL_V12_FastSim_v1/GEN-SIM-DIGI-RECO	1.56 M	290
single-top tW-channel	/SingleTop_tWChannel/Summer08_IDEAL_V11_redigi_v3/GEN-SIM-RECO	65.54 K	29

Table 4.10: QCD samples.

Process	Dataset	Events	$\sigma \times BR$ (pb)
QCD	/InclusiveMuPt15/Summer08_IDEAL_V11_redigi_v1/GEN-SIM-RECO	5.25 M	121000

4.2.3 Event Selection

In the t-channel single top quark production process with the W boson decays into a muon, the final state topology consists of one b-quark from top quark decay, a muon, a neutrino, a light quark and an additional b-quark. All final state objects have relatively large transverse momenta except for the additional b-quark, which is soft and difficult to observe and identify. The light quark tends to fly in the forward/backward direction, which will be useful for separation of signal from backgrounds. Then

$$pp \to t + b + q + X \to (bW^+) + b + q + X \to bb + q + \mu\nu_\mu + X,$$

leading to at least 3 hadronic jets, of which two originate from a b quark, an isolated muon and missing transverse energy in the event. Since the second b jet is most likely produced at high rapidities, i.e., outside the tracker acceptance of $|\eta| < 2.5$ and thus not allowing the b tagging to be performed, we expect most signal events to have only one b-tagged jet. The b-tag discriminator (based on Jet Probability algorithm) distributions for b-jet and non-b-jet are displayed in Figure 4.18. The kinematical distributions of the final state objects matched to the generated ones are shown in Figure 4.19

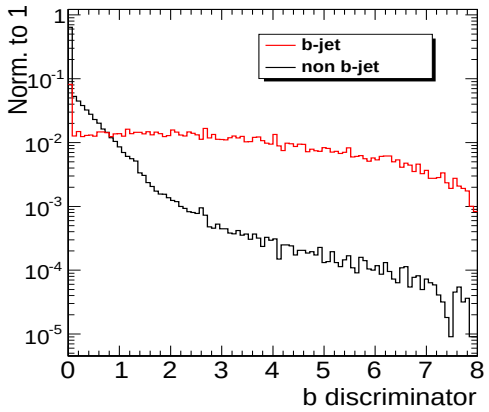


Figure 4.18: b-tag discriminator distributions for b-jet (matched to the b-quark) and non-b-jet (not matched to the b-quark).

Skim Selection

The skim selection contains the following online selection: Events must satisfy the `HLTMu15` trigger condition, which requires the presence of a non-isolated

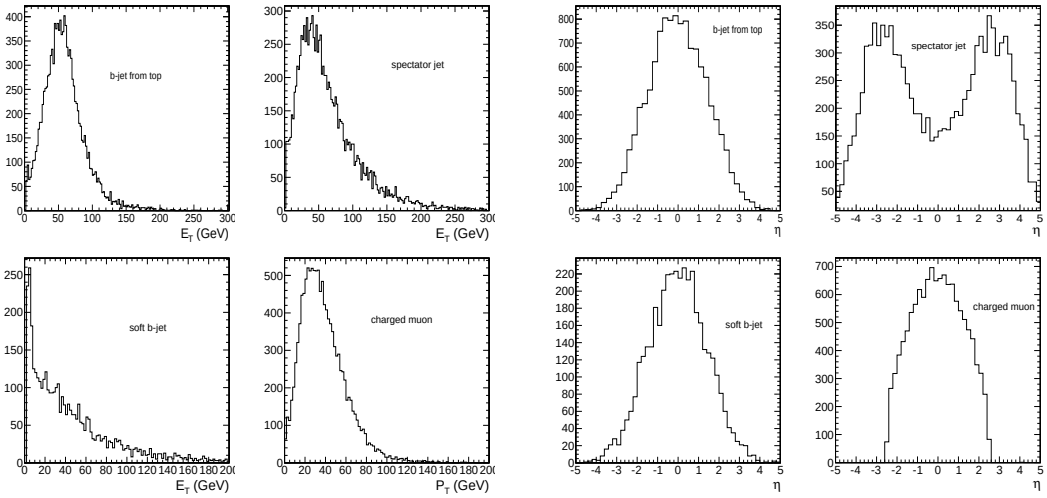


Figure 4.19: Transverse momentum and pseudorapidity distributions of the final state objects matched to the generated ones in t-channel single top production.

muon with $p_T > 15$ GeV. The trigger menus have been defined for the LHC luminosities of 10^{32} cm^{-2}s^{-1}.

Offline Pre-selection

- Only one jet $E_T > 30$ GeV in the region $|\eta| > 2.5$.
- Only one b-jet tagged (b-tag discriminator > 2.5) $E_T > 40$ GeV $|\eta| < 2.5$.
- At least one muon with $p_T > 20$ GeV and $|\eta| < 2.1$. No isolation requirement is applied at this stage, so that the data-driven QCD estimation based on muon isolation can be performed in the last step of event selection.

- Events are vetoed if there is an electron with $p_T > 20\,\text{GeV}$, $|\eta| < 2.4$, $p_{T\ iso}^{tracker} <$ 2 GeV, $E_{iso}^{calo} < 6$ GeV and the tight electron-ID selection.

- Events are vetoed if there is a 3rd jet (b-tag discriminator > 0.5) $E_T >$ 30 GeV, $|\eta| < 2.5$.

Offline Selection

The reconstruction of t and $\bar{t}$ quarks includes the following requirements:

- Reconstructed W mass based on muon and missing transverse energy (without P_Z) in the range $20 - 140\,\text{GeV}$, Figure 4.20 (left).

- Reconstructed top quark mass based on the b-tagged jet plus the W in the range $130 - 200$ GeV, Figure 4.20 (right). The neutrino four-vector is determined using transverse missing energy and the W and t masses. The initial values of P_T and azimuthal angle ϕ of neutrino are taken from the $\not\!\!E_T$ measurements. The initial value of the longitudinal neutrino momentum P_z is derived using the W-mass constraint. The neutrino components are determined by minimizing

  $$\chi^2 = \left(\frac{M(l\nu)-M_W}{\sigma_{M(W)}^{lept}}\right)^2 + \left(\frac{M(bl\nu)-M_t}{\sigma_{M(t)}^{lept}}\right)^2 + \left(\frac{p_T(\nu)-\not\!\!E_T}{\sigma_{p_T(\nu)}}\right)^2 + \left(\frac{\phi(\nu)-\phi(\not\!\!E_T)}{\sigma_{\phi(\nu)}}\right)^2 + \left(\frac{P_z(\nu)-P_z}{\sigma_{P_z(\nu)}}\right)^2,$$

  where the resolutions σ are obtained from the MadGraph $t\bar{t}$ Monte Carlo; the resolutions $\sigma_{p_T(\nu)}$ and $\sigma_{\phi(\nu)}$ are found as function of $\not\!\!E_T$.

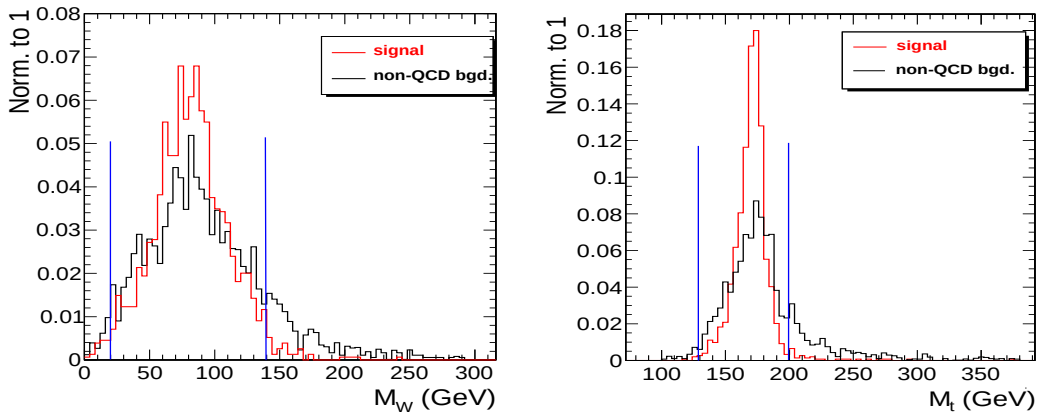


Figure 4.20: Reconstructed W mass (without neutrino P_Z) (left) and top quark mass (b-tag jet combined with W) (right). The W and t mass window requirements are shown.

- Azimuthal angle between the top quark and the spectator jet is required to be greater than 2.5 radians, Figure 4.21 (left).

- The magnitude of the vector sum of transverse momenta of all reconstructed objects, denoted as $|\vec{\Sigma}_T|$, where $\vec{\Sigma}_T = \vec{P}_{T,\,b\,jet} + \vec{P}_{T,\,\mu} + \vec{P}_{T,\,\nu} + \vec{P}_{T,\,spec.\,jet}$, must be smaller than 50 GeV, Figure 4.21 (right).

- χ^2 obtained from the fit of the neutrino components is less than 5, Figure 4.22.

- A final cut $RelIso > 0.98$, motivated by the data-driven QCD background estimation discussed in Section 4.2.4, is applied.

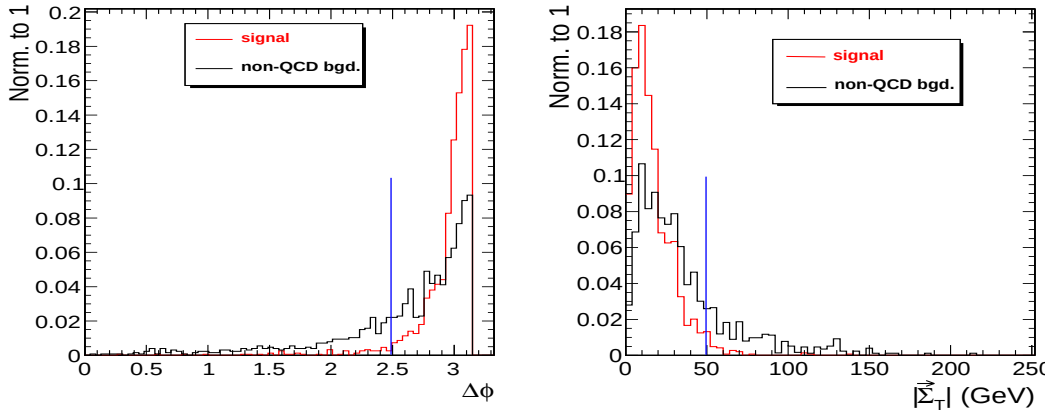


Figure 4.21: $\Delta\phi$ between the top quark and the spectator jet > 2.5 radians (left), $|\vec{\Sigma}_T| < 50$ (right).

The above selection requirements are optimized in Monte Carlo studies of the relevant reconstructed object matched to the corresponding generated objects.

4.2.4 Results

Data-driven QCD Background Estimation

After all the selection cuts but RelIso, the RelIso distribution for the reference subsample (without QCD events) and the RelIso distribution for the analysis subsample plus QCD events are produced, Figure 4.23. The reference RelIso distribution, Figure 4.23 left, is fitted with an appropriate function $F(x)$, which represents the shape of non-QCD contribution in RelIso distribution. Then, the analysis plus QCD RelIso distribution, Figure 4.23 right, representing the data distribution with yet unknown QCD contribution, is fitted with the sum of the

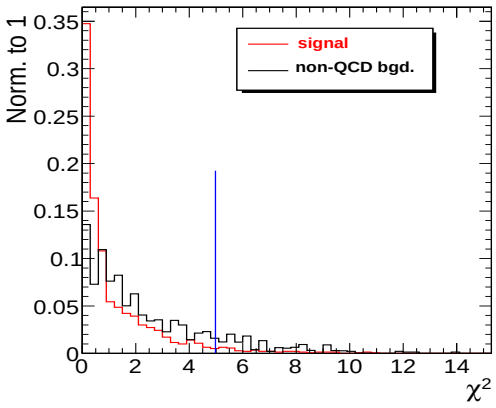


Figure 4.22: χ^2 obtained from the fit of the neutrino components < 5.

non-QCD function F(x) with free normalization and an exponential representing the QCD contribution:

$$P_0\, F(x) + P_1\, \exp(P_2\, x)\,, \tag{4.25}$$

where $P's$ are the fit parameters. The integral of the exponential component from 0.98 to 1.0 represents the QCD background contribution to the signal region, which is estimated along with its error as 258 ± 25 events, in agreement with 4 events actually passing the selection in the QCD sample, corresponding to 184 ± 92 QCD events in $2\,\text{fb}^{-1}$. The $RelIso > 0.98$ cut results in both good signal selection and low residual QCD background.

Signal and Background Yields

Table 4.11 summarizes the selection results obtained using the analysis subsample plus the QCD samples. Note that all event numbers are scaled to $2\,\text{fb}^{-1}$.

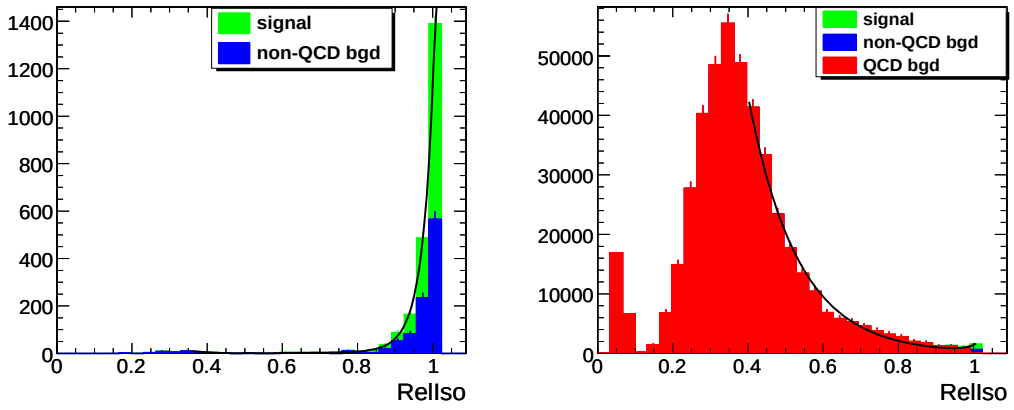


Figure 4.23: Muon relative isolation distributions for the reference subsample (without QCD events) (left) and for the analysis subsample plus QCD events (right). The fit curves are superimposed.

Since the QCD background is estimated with the RelIso method, there are no QCD angular distributions. Therefore, both the analysis and reference non-QCD background distributions are scaled to account for the additional 258 QCD background events. The signal to background ratio (S/B) is found to be 1.14 in the analysis subsample with an overall efficiency of 3.7%. Figure 4.24 shows the invariant mass of the reconstructed top and anti-top quarks plus background and the background only.

Since anti-top quark has almost half the cross section of top quark in single top t-channel production, the number of selected anti-top events is found to be almost half of that of selected top quarks. Also, the background contributions to top and anti-top are found to be approximately equal, resulting in the anti-

Table 4.11: Selection flow for the analysis subsample plus the QCD samples.

	Signal	$t\bar{t}$	W+Jets	VQQ	Single-top tW	QCD
# Events in $2\,\mathrm{fb}^{-1}$	28888	828000	$9.04 \cdot 10^7$	290000	29000	$8.02 \cdot 10^8$
Online Selection	24265	197064	1.434×10^7	66845	3632	$6.03 \cdot 10^8$
Offline Pre-Selection	1704	1820	1190	150	198	$1.13 \cdot 10^6$
Offline Selection	1376	395	519	59	48	430370
N_μ (RelIso > 0.98) $= 1$	1075	261	356	35	29	258

top S/B=0.71 compared to the top S/B=1.59. Due to large systematic errors coming from the low S/B ratio in anti-top events, only the selected top events are used to estimate the spin asymmetry coefficients.

Figure 4.25 shows the reconstructed angular distributions in only top events after the selection. Note that in these figures the signal plus background is obtained from the analysis subsample and corrected for the QCD background contribution as mentioned above, and the background is obtained from the reference subsample. The angular resolutions are determined by taking the difference between the cosine of the generated and reconstructed angles using the single top t-channel signal events from the analysis subsample with good jet-parton matching. The resolutions are found to be 0.121 and 0.124 for $cos(\phi_{l\text{-}s})$ and $cos(\phi_{l\text{-}z})$, respectively, see Figure 4.26. A bin size approximately two times the resolution results in 8 bins for the angular distributions.

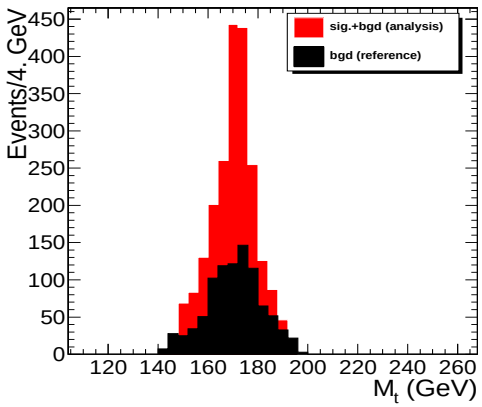


Figure 4.24: Reconstructed t and $\bar{t}$ quark invariant mass spectra.

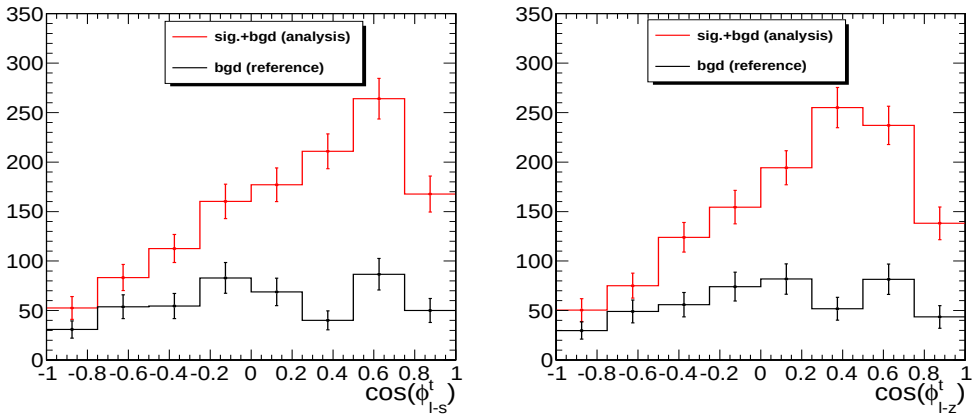


Figure 4.25: Reconstructed angular distributions in top events only: l-s angle (left) and l-z angle (right).

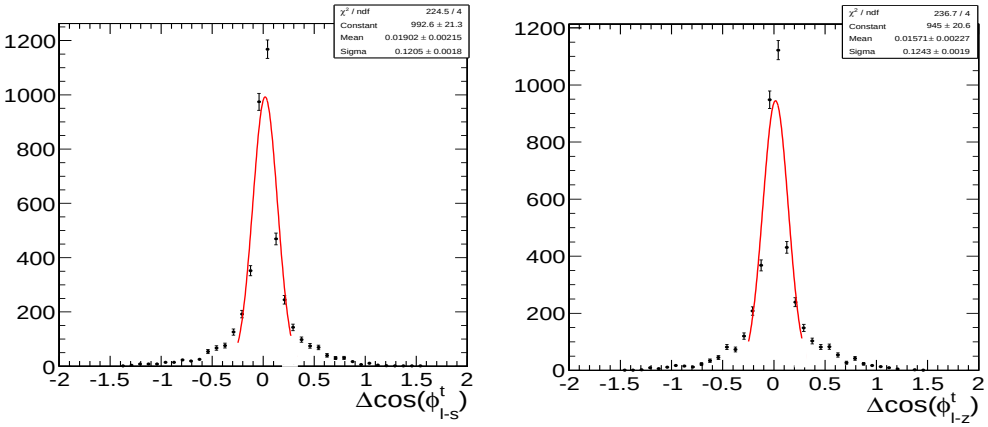


Figure 4.26: Resolution of $cos(\phi_{l\text{-}s})$ (left) and $cos(\phi_{l\text{-}z})$ (right) in top events.

Unfolding Angular Distributions

Figure 4.27 shows the response matrices for $\cos(\phi_{l\text{-}s})$ and $\cos(\phi_{l\text{-}z})$ for top events only. They are obtained by tracking the generated and reconstructed values for each event after all selection cuts. For the toy tests, $22\,\text{fb}^{-1}$ fast simulated single top t-channel signal events are used for constructing the $\cos(\phi_{l\text{-}s})$ and $\cos(\phi_{l\text{-}z})$ response matrices and the toy measured distributions to be unfolded. The same toy test steps described in Section 4.1.5 are followed for each τ value. It is determined that $\tau = 4$ is the optimum value for the regularization parameter. Using this τ value, Steps 1-4 are repeated with the measured distribution from the analysis subsample to obtain the pull distributions.

Figures 4.28 and 4.29 show the resulting pull distributions for each bin of $\cos(\phi_{l\text{-}s})$ and $\cos(\phi_{l\text{-}z})$ distributions. The mean and sigma values obtained from

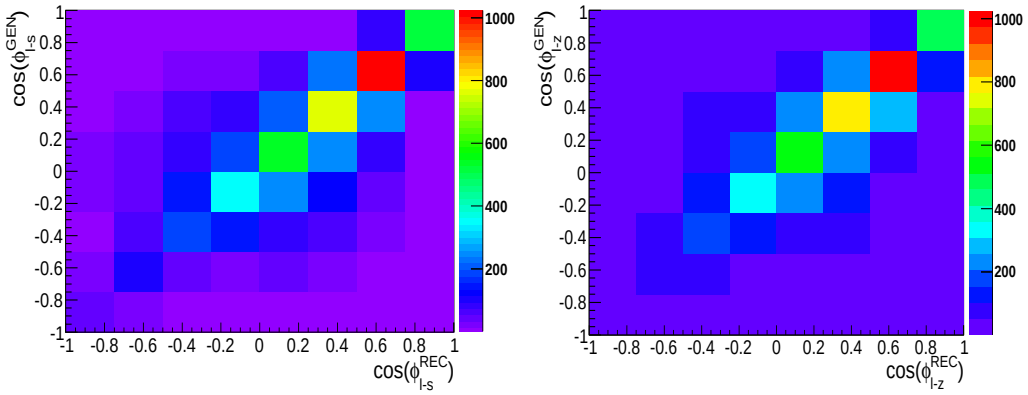


Figure 4.27: Response matrices from the reference subsample: l-s angle (left) and l-z angle (right).

a Gaussian fit to the pull distributions are given in Table 4.12. These results are used to determine the systematic uncertainty coming from the unfolding procedure, see Section 4.2.5.

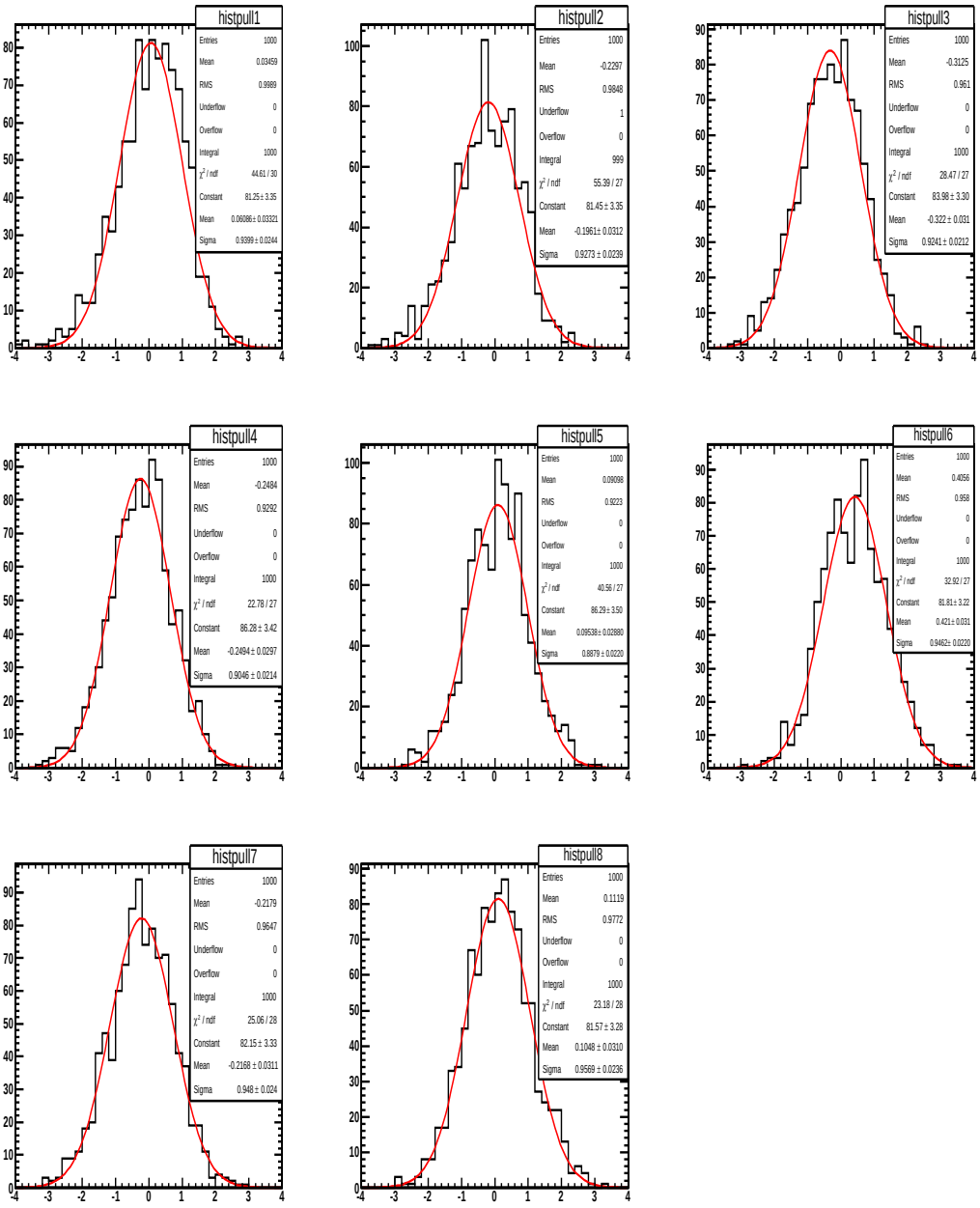


Figure 4.28: Pull distributions from unfolding the $\cos(\phi_{l\text{-}s})$ distribution with regularization parameter $\tau = 4$.

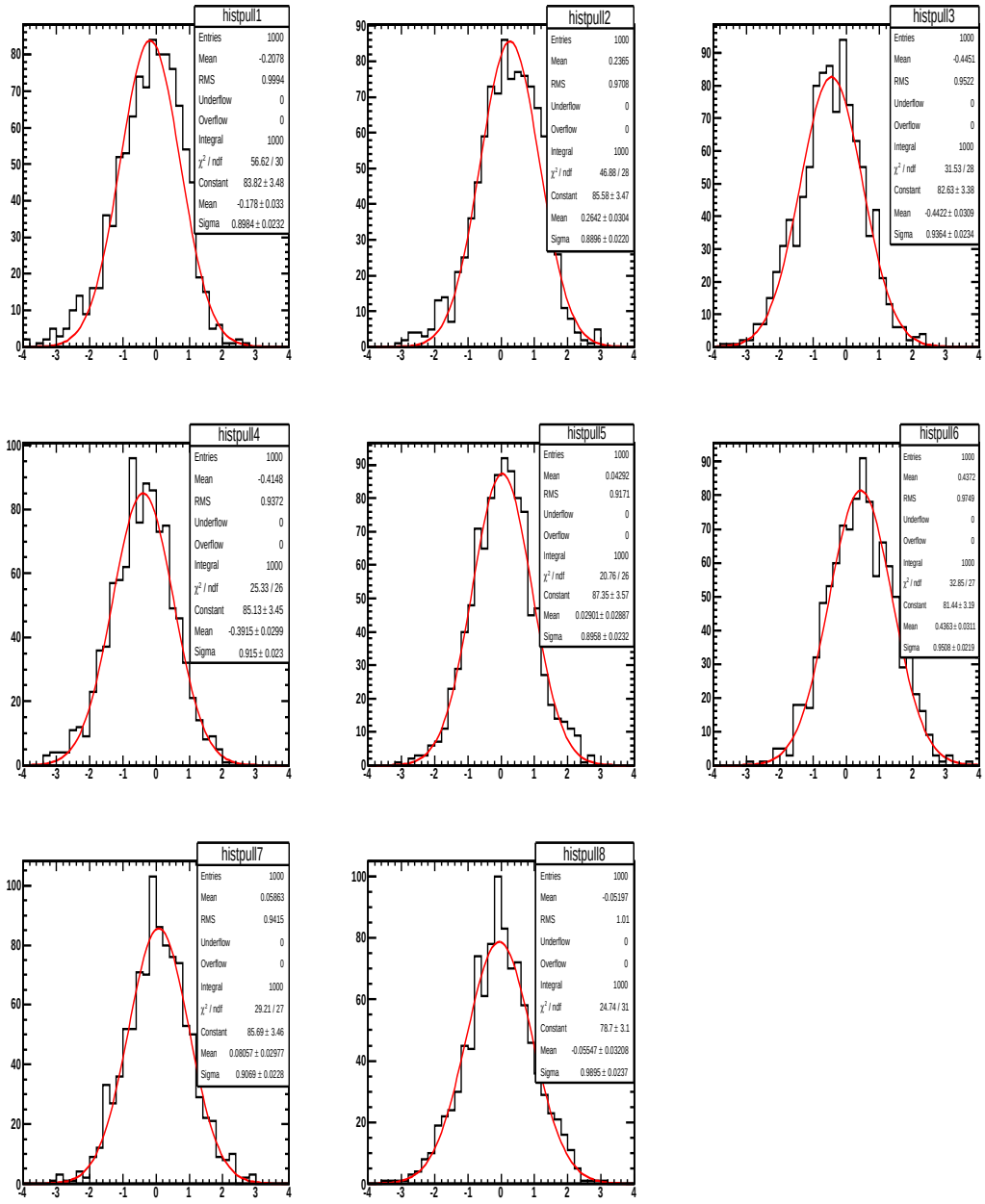


Figure 4.29: Pull distributions from unfolding the $\cos(\phi_{l\text{-}z})$ distribution with regularization parameter $\tau = 4$.

Table 4.12: Results of the Gaussian fits for the $\cos(\phi_{l\text{-}s})$ (left) and $\cos(\phi_{l\text{-}z})$ (right) pull distributions with regularization parameter $\tau = 4$.

bin	mean	σ
1	0.061 ± 0.033	0.940 ± 0.024
2	-0.196 ± 0.031	0.927 ± 0.024
3	-0.322 ± 0.031	0.924 ± 0.021
4	-0.249 ± 0.030	0.905 ± 0.021
5	0.095 ± 0.028	0.888 ± 0.022
6	0.421 ± 0.031	0.946 ± 0.022
7	-0.217 ± 0.031	0.948 ± 0.024
8	0.105 ± 0.031	0.957 ± 0.024

bin	mean	σ
1	-0.178 ± 0.033	0.898 ± 0.023
2	0.254 ± 0.030	0.890 ± 0.022
3	-0.442 ± 0.031	0.935 ± 0.023
4	-0.392 ± 0.030	0.915 ± 0.023
5	0.029 ± 0.029	0.896 ± 0.023
6	0.436 ± 0.031	0.951 ± 0.022
7	0.081 ± 0.030	0.907 ± 0.023
8	-0.055 ± 0.031	0.989 ± 0.024

Estimation of the Spin Asymmetry Coefficients

The final measurements of the angular distributions are obtained by subtracting, bin-by-bin, the background obtained from the reference subsample from the total of signal plus background (Figure 4.25) obtained from the analysis subsample. The resulting distributions are unfolded as described above to obtain the true distributions shown in Figure 4.30.

The spin asymmetry coefficients A in the spectator and beamline bases for top events are then obtained by individually fitting angular distributions in

Figure 4.30 according to Formula 4.22:

$$A_s^t = 0.949 \pm 0.089 \text{ and } A_z^t = 0.871 \pm 0.102\,, \tag{4.26}$$

which agree within the statistical errors with the MadGraph results given in Section 4.2.1.

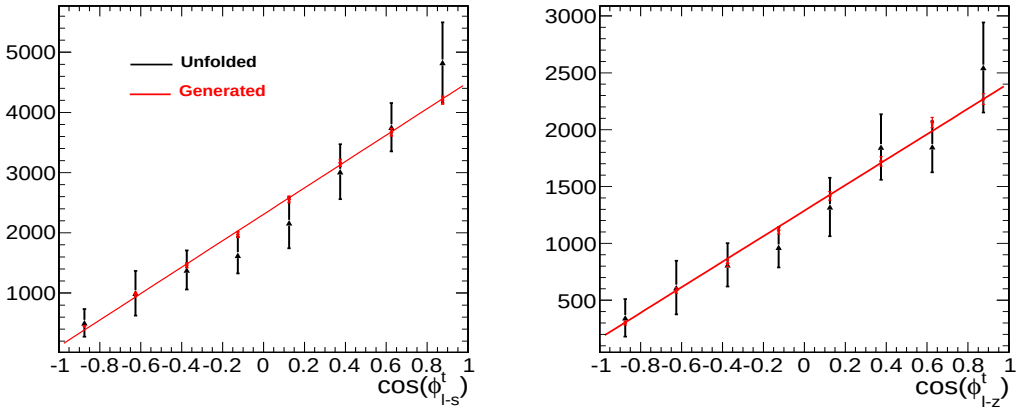


Figure 4.30: Background subtracted and unfolded opening angle distributions in single t events (black points): l-s angle (left) and l-z angle (right). The black lines represent the fit of angular distributions. The number of events corresponds to an integrated luminosity of $2\,\text{fb}^{-1}$.

4.2.5 Systematic Uncertainties

Systematic Uncertainties at Generation Level

- **PDF**: The impact of parton distribution function is estimated by taking the difference between the measurements obtained with the default PDF

CTEQ6L and two others, CTEQ5L, MRST2002NL. The variations in A_s^t are +0.5% and +1.5%, and in A_z^t are +0.6% and +2.7% for CTEQ5L and MRST2002NL, respectively.

- **Top mass and single top t-channel cross section**: As shown in [60], the top mass and $\sigma_{t\text{-}ch}$ uncertainties lead to negligible variation in spin correlations.

- **W+jets and VQQ** : The cross sections for W+jets and VQQ background processes are varied by ±50% [61], this results in −8.3%/+10.4% and −10.1%/+12.5% variation in A_s^t and A_z^t, respectively.

- **Jet multiplicity**: Uncertainties in initial state and final state radiations (ISR and FSR), pile up rate could result in an underestimation of the number of non-single top t-channel jets. The variation in jet multiplicity due to these uncertainties is estimated with Minimum Bias (MB) events by counting the number of jets with $p_T > 30$ GeV and $|\eta| < 5.0$. Underestimation coming from MB events is 0.5%. The variation in jet multiplicity due to QCD radiations is estimated by comparing $t\bar{t}$ events with larger ISR and FSR with $t\bar{t}$ events with nominal ISR and FSR. The comparison is made with counting the number of jets with $p_T > 30$ GeV and $|\eta| < 5.0$. Underestimation turns out to be 1%. This results in a total jet multiplicity underestimation of 1.5%. To test this effect, 1.5% additional

background jets per event are generated while processing the data sample. Jets are simulated randomly according to p_T, η and b-discriminator distributions obtained from Minimum Bias event samples for this sort of jet. The variation in A_s^t and A_z^t are found to be negligible.

Systematic Uncertainties at Reconstruction Level

- **b-tagging**: b identification discriminator in b-jet (and vetoed third jet) is changed such that b-tagging efficiency varies by +6% and -6% [62]. The variations in A_s^t and A_z^t are -5.0%/+10.5% and -3.7%/+11.2%, respectively.

- **JES**: The uncertainty due to the jet energy scale uncertainty is evaluated by varying the jet energy by ±2%, which is derived from [63]. A_s^t and A_z^t are varied by +7.2%/-3.0% and +8.3%/-6.1%, respectively.

- **MET**: The Missing Transverse Energy $\not{E}_T$ is varied by ±10% as used in [61]. The variations in A_s^t and A_z^t turn out to be +3.4%/-5.0% and +6.0%/-5.2%, respectively.

Other Systematic Uncertainties

- **Uncertainty in QCD Background Estimation**: The uncertainty in the number of QCD events from the data-driven method is estimated using the statistical error of the fit performed with the $RelIso$ distribution,

Figure 4.23 (right), plus varying the shape of the non-QCD distribution, Figure 4.23 (left) by changing the W+jets and VQQ contributions by $\pm 50\%$ and varying the fit range in $RelIso$ by approximately one bin size (± 0.05). These add up to a $\pm 30\%$ error in QCD background resulting in -4.2%/+5.0% and -5.3%/+6.1% variations in A_s^t and A_z^t, respectively.

- **Uncertainty from Unfolding Procedure** The mean values given in Table 4.6 are used to estimate the systematic uncertainty coming from the unfolding procedure. The $\cos(\phi_{l\text{-}s})$ and $\cos(\phi_{l\text{-}z})$ distributions are corrected, bin-by-bin, according to the shift in the mean from 0. Then, the modified distributions are used to extract A using the global fit as before. The variations in A_s^t and A_z^t are found to be -1.5% and -3.0%, respectively.

Table 4.13 summarizes the systematic uncertainty results.

4.2.6 Conclusions for Single Top Production

The top quark spin asymmetry coefficients in the spectator and beamline bases in single top t-channel production in proton-proton collisions at 10 TeV are measured using the angular distributions of the top quark decay products ($\phi_{l\text{-}s}$ and $\phi_{l\text{-}z}$). Based on a total integrated luminosity of two inverse femtobarns, the

results are

$$A_s^t = 0.949 \pm 0.089\ (\text{stat.})^{+0.167}_{-0.116}(\text{sys.}).$$

$$A_z^t = 0.871 \pm 0.102\ (\text{stat.})^{+0.181}_{-0.128}(\text{sys.}).$$

Including the systematic uncertainties, the measurement has a total relative uncertainty of 20.0% and 23.4% in A_s^t and A_z^t, respectively.

Table 4.13: Results obtained for each source of systematic uncertainty considered and the total systematic uncertainty. The total gives the sum of the systematic errors in quadrature.

Source of systematic uncertainty	Uncertainty in A_s^t (%)	Uncertainty in A_z^t (%)
PDF (CTEQ5L and MRST2002NL)	$+0.5, +1.5$	$+0.6, +2.7$
Top Mass ($\pm 5\%$)	negligible	negligible
single top t-ch. cross section ($\pm 10\%$)	negligible	negligible
W+jets and VQQ ($+50\% - 50\%$)	$-8.3, +10.4$	$-10.1, +12.5$
Jet multiplicity ($+1.5\%$)	negligible	negligible
Sensitivity to single top modeling	negligible	negligible
b-tagging efficiency ($\pm 6\%$)	$-5.0, +10.5$	$-3.7, +11.2$
JES ($\pm 2\%$)	$+7.2, -3.0$	$+8.3, -6.1$
MET ($\pm 10\%$)	$+3.4, -5.0$	$+6.0, -5.2$
QCD background estimation ($\pm 25\%$)	$-4.2, +5.0$	$-5.3, +6.1$
Unfolding Procedure	-1.6	-3.0
Total	$+17.6, -12.2$	$+20.8, -14.7$

4.3 Future Plan

The study of measurement of spin correlation in top pair production in semileptonic decay channel with the simulated data has been completed. As soon as real data is available in 2010, the same analysis done for simulated data will be repeated for real data, experimental values will be compared to the theoretical results obtained and using by CMSSW.

The spin correlation study of single top production in t-channel with the simulated data has also been completed. The single top spin correlation analysis will be applied to real data to be obtained from CMS as soon as it is available. The results from real data will be compared with those of simulated data to check and verify the Standard Model expectation for spin of top quark.

Bibliography

[1] D. Griffiths, "Introduction to Elementary Particles," *John Wiley & Sons* (1987).

[2] F. Halzen and A. Martin, "Quarks and Leptons," *John Wiley & Sons* (1984).

[3] M. Kaku, "Quantum Field Theory: A Modern Introduction," *Oxford University Press* (1993).

[4] W. Cottingham and D. Greenwood, "An Introduction to the Standard Model of Particle Physics," *Cambridge University Press* (1998).

[5] W. Greiner and J. Reinhardt, "Quantum Electrodynamics," *Springer Verlag* (1995).

[6] W. Greiner, S. Schramm, and E. Stein, "Quantum Chromodynamics," *Springer Verlag* (1995).

[7] S. Glashow, "Partial-symmetries of weak interactions," *Nuclear Physics 22* **579** (1961).

[8] S. Weinberg, "A model of leptons," *Physical Review Letters 19* **1264** (1967).

[9] S. Salam, "In elementary particle theory," *Almqvist and Wiksells, Stockholm* **367** (1968).

[10] **D0** Collaboration, S. Abachi et al. *Phys. Rev. Lett.* **74** (1995) 2632.

[11] **D0 and CDF** Collaboration, "A Combination of CDF and D0 Results on the Mass of the Top Quark," `arXiv:hep-ex/0703034`.

[12] **CDF** Collaboration, "Combination of CDF top quark pair production cross section measurements with up to 760 pb^{-1}," *CDF Note* (1996).

[13] **CDF** Collaboration, F. Abe et al. *Phys. Rev. Lett.* **74** (1995) 2626.

[14] **D0** Collaboration, V. M. Abazov et al., "Evidence for production of single top quarks," *Phys. Rev. Lett.* **78** (2008) 012005, `arXiv:hep-ex/0803.0739v2`.

[15] **CDF** Collaboration, "Combination of CDF Single Top Quark Searches with $2\,\text{fb}^{-1}$ of Data," *CDF* **9251** (2008).

[16] **CMS** Collaboration, G. L. Bayatian et al. *J. Phys* **G 34** (2007) 995.

[17] N. Kidonakis and R. Vogt, "The theoretical top quark cross section at the Tevatron and the LHC," *Phys.Rev* **D78** (2008) 074005, arXiv:0805.3844v1.

[18] T. K, "Top Quark Production and Decay Measurements from CDFCombination of CDF," *Proceedings of the ICHEP 98* **FERMILAB-CONF-98-389-E** (1998).

[19] **Particle Data Group** Collaboration, W. M. Yao and other *J. Phys.* **G 33** (2006).

[20] T. Stelzer, Z. Sullivan, and S. Wilenbrock *Phys. Rev.* **D 56** (1997) 5919.

[21] https://twiki.cern.ch/twiki/bin/view/CMS/TWikiTopQuark2008SingleT.

[22] A. Giammanco et al., "Prospects for a measurement of the single-top t-channel cross section in the muon channel, with the first 200 pb^{-1} of CMS data at 10 TeV," *CMS AN Note* **2009/069** (2009).

[23] LHCb Collaboration, http://lhcb.web.cern.ch/lhcb/.

[24] **LCH** Collaboration, "LHC Design Report," *CERN/LHCC* **03** (2004).

[25] LEP Experiments, http://greybook.cern.ch/.

[26] **CMS** Collaboration, "Physics Technical Design Report, Vol. 1: Detector Performance and Software," *CERN/LHCC* **2006-001** (2006).

[27] **CMS** Collaboration, "The CMS experiment at the CERN LHC, Journal of Instrumentation," *Journal of Instrumentation* **3** (2008).

[28] ATLAS Collaboration, http://atlas.web.cern.ch/Atlas/index.html.

[29] LHCb Collaboration, http://lhcb.web.cern.ch/lhcb/.

[30] ALICE Collaboration, http://aliceinfo.cern.ch/.

[31] **CMS** Collaboration, "CMS Tracker Project, Technical Design Report," *CERN/LHCC* **98-6** (1998).

[32] **CMS** Collaboration, "ECAL Technical Design Report," *CERN/LHCC* **97-033** (1997).

[33] N. Akchurin and R. Wigmans *Rev. Scien. Instr.* **74** (2002) No. 6.

[34] G. Baiatian, A. Sirunyan, et al., "Design, Performance, and Calibration of CMS Forward Calorimeter Wedges," *CMS NOTE* **2006/044** (2006).

[35] **CMS** Collaboration, "The Magnet Project Technical Design Report," *CERN/LHCC* **97-010** (1997).

[36] **CMS** Collaboration, "The muon project technical design report," *CERN/LHCC* **97-032** (1997).

[37] **CMS** Collaboration, "Level-1 Trigger Technical Design Report," *CERN/LHCC* **2000-038** (2000).

[38] **CMS** Collaboration, "DAQ and High-Level Trigger Technical Design Report," *CERN/LHCC* **2002-026** (2002).

[39] **D0** Collaboration, "Spin Correlation in tt-bar Production from pp-bar Collisions at sqrt(s)=1.8 TeV," *Phys. Rev. Lett.* **85** (2000) 256–261, arXiv:hep-ex/0002058.

[40] G. Mahlon and S. Parke, "Angular correlations in top quark pair production and decay at hadron colliders," *Phys. Rev* **D53** (1996) 4886.

[41] W. Bernreuther, A. Brandenburg, and P. Uwer, "Transverse polarization of top quark pairs at the Tevatron and the LHC," *Phys. Lett.* **B 368** (1996) 153, arXiv:hep-ph/9510300.

[42] A. Czarnecki, M. Jezabek, and J. Kuhn, "Lepton spectra from decays of polarized top quarks," *Nucl. Phys.* **B 351** (1991) 70.

[43] G. Mahlon, "Spin Issues in $t\bar{t}$ Production and Decay," *McGill/98-34* arXiv:hep-ph/9811281.

[44] W. Bernreuther et al., "Top quark pair production and decay at hadron colliders," *Nucl. Phys.* **B 690** (2004) 81, arXiv:hep-ph/0403035.

[45] M. Mangano et al., "ALPGEN, a generator for hard multiparton processes in hadronic collisions," *JHEP* **0307** (2003) 001, arXiv:hep-ph/0206293.

[46] https://twiki.cern.ch/twiki/bin/view/CMS/SWGuideFrameWork.

[47] S. Lowette et al., "Top Quark Analysis Framework," *CMS Internal Note* **2007/068** (2007).

[48] https://twiki.cern.ch/twiki/bin/view/CMS/SWGuidePAT.

[49] J. Alwall et al., "MadGraph/MadEvent v4: The new web generation," *JHEP* **0709** (2007) 028, `arXiv:0706.2334`.

[50] T. Sjostrand, S. Mrenna, and P. Skands, "PYTHIA 6.4 physics and manual," *JHEP* **05** (2006) 026, `arXiv:hep-ph/0603175`.

[51] **CMS** Collaboration, "Physics Technical Design Report, Vol. 1: Detector Performance and Software; Chapter 9, Muons," *CERN/LHCC* **2006-001** (2006) 026.

[52] **CMS** Collaboration, "Physics Technical Design Report, Vol. 1: Detector Performance and Software," *CERN/LHCC* **2006-001** (2006) 026.

[53] https://twiki.cern.ch/twiki/bin/view/CMS/SWGuideEgammaIsolation.

[54] A. Rizzi, F. Palla, and G. Segneri, "Track impact parameter based b-tagging with CMS," *CERN CMS Note* **2006/019** (2006).

[55] https://twiki.cern.ch/twiki/bin/view/CMS/SWGuideTQAFLayer.

[56] J. D'Hondt et al., "Fitting of Event Topologies with External Kinematic Constraints in CMS," *CMS Note* **2006/023** (2006).

[57] J. D'Hondt et al., "Measurement of jet energy scale corrections using top quark events," *CMS AN Note* **2007/029** (2007).

[58] A. Hocker and V. Kartvelishvili, "SVD Approach to Data Unfolding," *Nucl. Instrum. Meth* **A372** (1996) 469.

[59] http://root.cern.ch/root/html/TH1.html#TH1:GetRandom.

[60] M. Baarmand, H. Mermerkaya, and I. Vodopiyanov, "Measurement of Spin Correlation in Top Quark Pair Production in Semi-Leptonic Final State," *CERN CMS Note* **2006/111** (2006).

[61] A. Giammanco et al., "Towards a measurement of single-top cross section in the t channel, with the first inverse femtobarn of CMS data at 14 TeV," *CMS AN Note* **2009/026** (2009).

[62] M. Narain, P. Tan, et al., "Performance Measurement of b tagging Algorithms Using Data containing Muons within Jets," *CMS AN Note* **2007/046** (2007).

[63] S. Esen, "Plans for Jet Energy Corrections at CMS," *CMS AN Note* **2007/055** (2007).

[64] G. Mahlon and S. Parke, "Improved spin basis for angular correlation studies in single top quark production at the Fermilab Tevatron," *Phys. Rev* **D55** (1997) 7249, `arXiv:hep-ph/9611367`.

Appendix

Jet Combination Observables

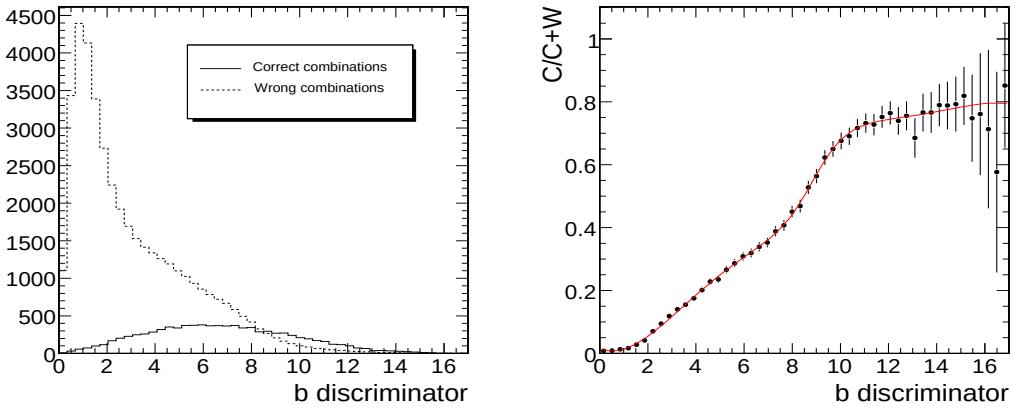


Figure 1: Sum of b-tagging discriminator of two b jets

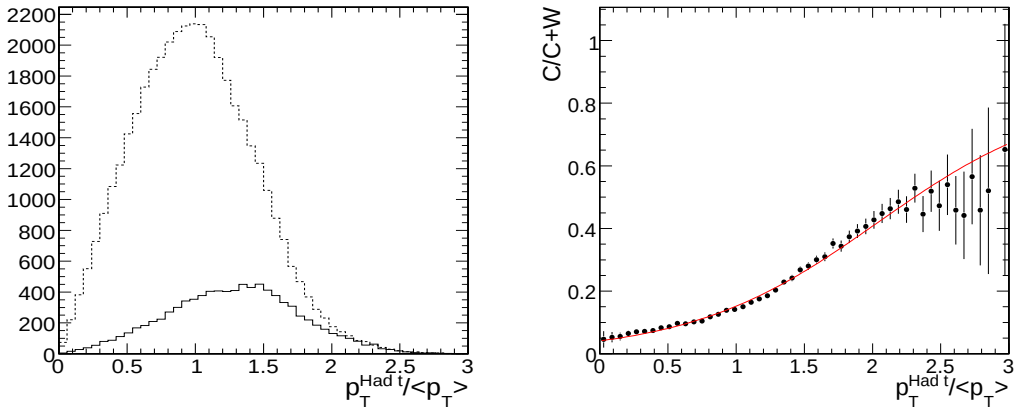


Figure 2: Transverse momentum of the hadronically decaying t quark divided by the average transverse momentum of the hadronically decaying t quarks over all possible jet combinations.

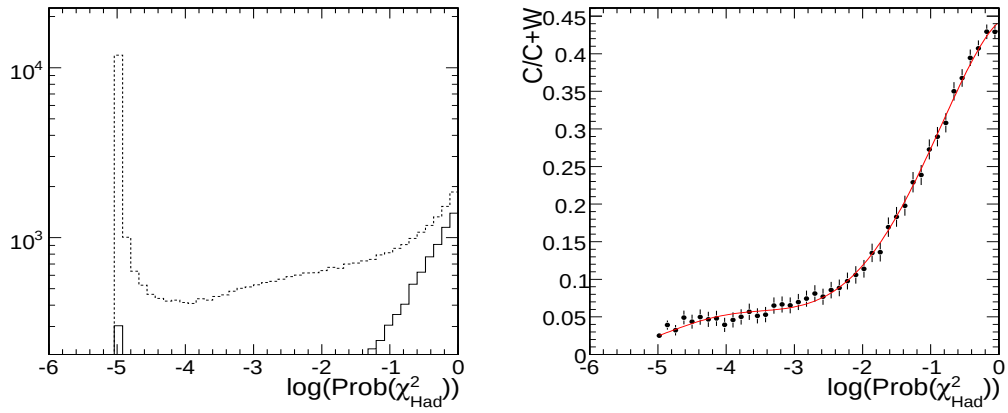


Figure 3: Probability obtained from the kinematic fit of the two light jets with W-mass constraint.

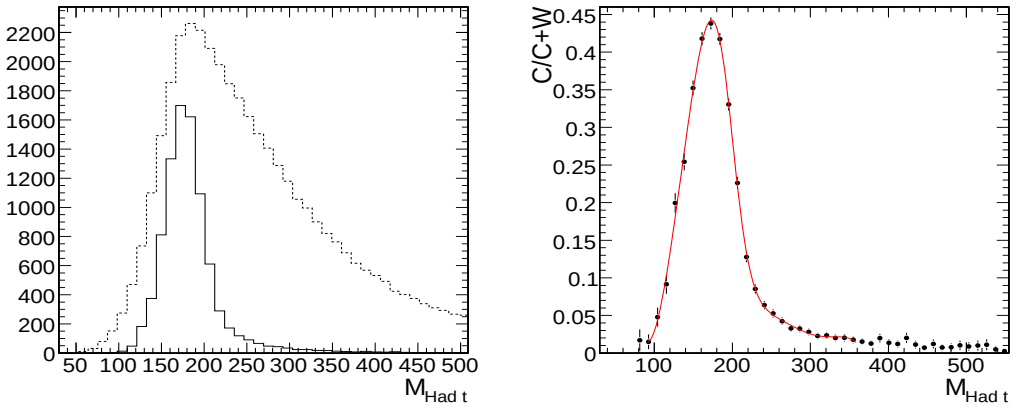


Figure 4: Mass of the hadronically decaying t.

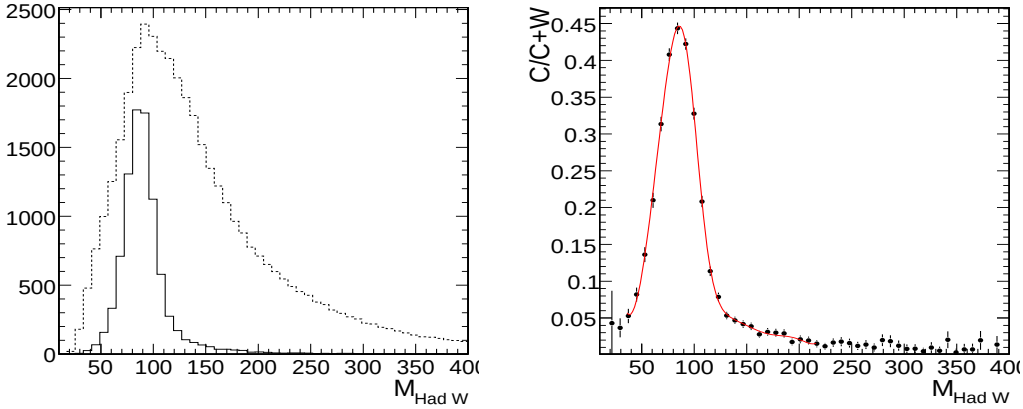


Figure 5: Mass of the hadronically decaying W.

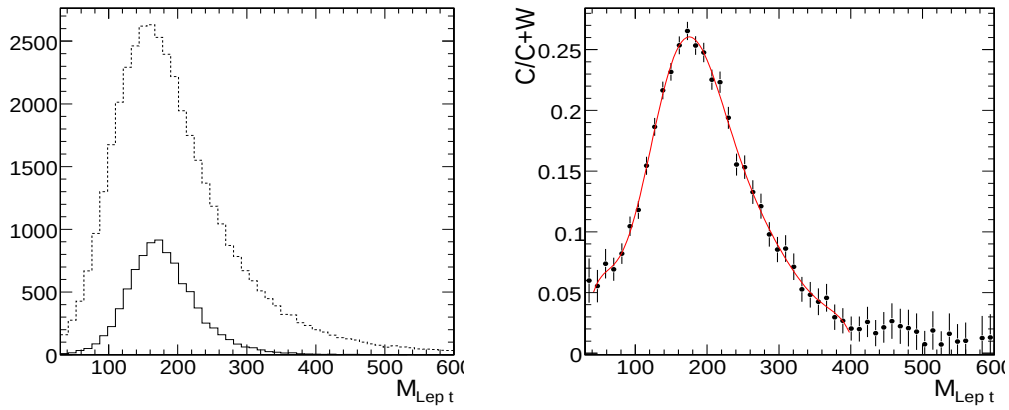


Figure 6: Mass of the leptonically decaying t estimated with neutrino $P_z = 0$.

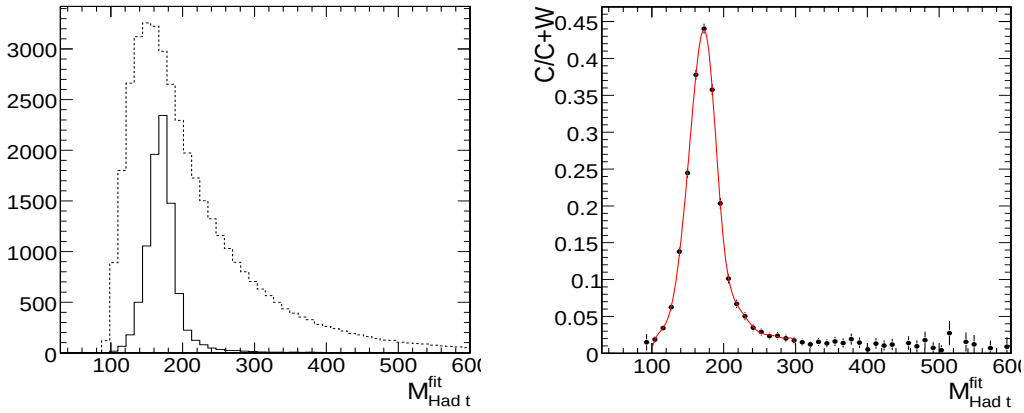


Figure 7: Mass of the hadronically decaying t using the modified light jets parameters from the kinematic fit with W-mass constraint.

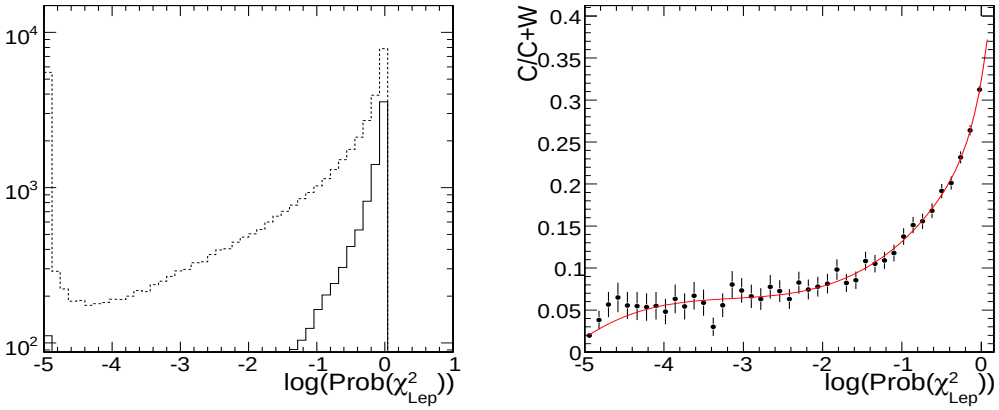


Figure 8: Probability obtained from the fit of the neutrino components.